UNIVERSITY OF CALIFORNIA,
IRVINE

# Iron Pyrite Single Crystal Studies

DISSERTATION

submitted in partial satisfaction of the requirements
for the degree of

DOCTOR OF PHILOSOPHY

in Physics

by

Trenton Salk

Dissertation Committee:
Professor Matt Law, Chair
Professor Shane Ardo
Professor Reginald Penner

2019

# DEDICATION

To

my parents and friends

in recognition of their worth

# TABLE OF CONTENTS


Page

LIST OF FIGURES v

LIST OF TABLES vi

ACKNOWLEDGMENTS vii

CURRICULUM VITAE viii

ABSTRACT OF THE DISSERTATION ix

**1. Introduction 1**
- 1.1. The Energy Crisis and Solar Power ..... 1
- 1.2. Iron Pyrite ($FeS_2$) ..... 5
- 1.3. Scope of This Work ..... 8

**2. Methods 9**
- 2.1. Single Crystal Synthesis ..... 9
  - 2.1.1. Flux Growth ..... 9
  - 2.1.2. Doped Single Crystal Growth ..... 11
- 2.2. Sample Preparation ..... 12
  - 2.2.1. Sectioning & Polishing ..... 12
  - 2.2.2. Electrical Contacts ..... 13
- 2.3. Structural & Elemental Characterization ..... 14
  - 2.3.1. X-Ray Diffraction (XRD) ..... 14
  - 2.3.2. Raman Spectroscopy ..... 15
  - 2.3.3. Mass Spectrometry ..... 15
- 2.4. Optical & Morphological Characterization ..... 17
  - 2.4.1. Optical Absorption Spectroscopy ..... 17
  - 2.4.2. Spectroscopic Ellipsometry ..... 19
  - 2.4.3. Atomic Force Microscopy (AFM) ..... 19
- 2.5. Electrical & Magnetization Characterization ..... 19
  - 2.5.1. Temperature-Dependent Conductivity & Hall Effect ..... 19
  - 2.5.2. Vibrating Sample Magnetometry (VSM) ..... 21
- 2.6. Data Modeling & DFT Calculations ..... 22
  - 2.6.1. Charge Transport ..... 22
  - 2.6.2. Density Functional Theory (DFT) Calculations ..... 25

**3. Undoped Pyrite Single Crystals 27**
- 3.1. Characterization ..... 27

3.1.1. Elemental Characterization ..... 27
3.1.2. Structural Characterization ..... 30
3.1.3. Hall Effect Studies ..... 33
3.1.4. Optical Absorption ..... 35
3.1.5. Magnetization ..... 42

**4. Doped Pyrite Single Crystals 45**
4.1. Cobalt Doped ($Co_xFe_{1-x}S_2$) ..... 48
4.1.1. Elemental Characterization ..... 49
4.1.2. Structural Characterization ..... 51
4.1.3. Hall Effect Studies ..... 53
4.1.4. Optical Absorption ..... 57
4.1.5. Magnetization ..... 58
4.1.6. Summary ..... 61
4.2. Nickel Doped ($Ni_xFe_{1-x}S_2$) ..... 64
4.2.1. Elemental Characterization ..... 64
4.2.2. Structural Characterization ..... 67
4.2.3. Hall Effect Studies ..... 69
4.2.4. Optical Absorption ..... 71
4.2.5. Magnetization ..... 73
4.2.6. Summary ..... 75
4.3. Chromium Doped ($Cr_xFe_{1-x}S_2$) ..... 77
4.3.1. Elemental Characterization ..... 77
4.3.2. Structural Characterization ..... 78
4.3.3. Hall Effect Studies ..... 81
4.3.4. Optical Absorption ..... 83
4.3.5. Magnetization ..... 84
4.3.6. Summary ..... 86
4.4. Conclusions ..... 89

REFERENCES 93

# LIST OF FIGURES


Page

Figure 1.1 SunShot initiative progress and goals ..... 1
Figure 1.2 Annual potential electricity production and raw material cost ..... 4
Figure 1.3 Unit cell and band diagrams of iron pyrite ..... 6
Figure 1.4 Calculated equilibrium band diagram of the pyrite surface at 300 K ..... 7

Figure 2.1 Na-S binary phase diagram ..... 10
Figure 2.2 Typical pyrite sample preparation. ..... 14
Figure 2.3 Conductivity and Hall effect of a multilayer system ..... 23

Figure 3.1 Structural characterization of undoped pyrite crystals. ..... 31
Figure 3.2 Raman spectra of a powderized single crystal ..... 32
Figure 3.3 Electrical properties of undoped pyrite crystals ..... 34
Figure 3.4 Index of refraction and extinction coefficient for pyrite ..... 36
Figure 3.5 Absorption coefficient of undoped pyrite crystals ..... 37
Figure 3.6 High energy spectral features of undoped pyrite ..... 38
Figure 3.7 Room temperature far-IR spectra of a pyrite crystal ..... 40
Figure 3.8 Spectra of low energy features ..... 41
Figure 3.9 Magnetic properties of undoped pyrite crystals ..... 43
Figure 3.10 Molar susceptibility as a function of temperature for undoped crystals. ..... 44

Figure 4.1 Synchrotron XRD pattern of powdered $Co_xFe_{1-x}S_2$ crystals ..... 52
Figure 4.2 Electrical properties of $Co_xFe_{1-x}S_2$ crystals ..... 54
Figure 4.3 Number of charge carriers as a function of Co concentration ..... 56
Figure 4.4 Optical absorptivity spectra of $Co_xFe_{1-x}S_2$ crystals ..... 58
Figure 4.5 Magnetic properties of $Co_xFe_{1-x}S_2$ crystals ..... 59
Figure 4.6 DFT results for $Co_xFe_{1-x}S_2$ ..... 62
Figure 4.7 Synchrotron powder XRD patterns of $Ni_xFe_{1-x}S_2$ crystals ..... 68
Figure 4.8 Electrical properties of $Ni_xFe_{1-x}S_2$ crystals ..... 70
Figure 4.9 Optical absorptivity spectra of $Ni_xFe_{1-x}S_2$ crystals ..... 72
Figure 4.10 Magnetic properties of $Ni_xFe_{1-x}S_2$ crystals. ..... 74
Figure 4.11 DFT results for $Ni_xFe_{1-x}S_2$. ..... 76
Figure 4.12 Synchrotron XRD pattern of powdered $Cr_xFe_{1-x}S_2$ crystals ..... 80
Figure 4.13 Electrical properties of $Cr_xFe_{1-x}S_2$ crystals ..... 82
Figure 4.14 Optical absorptivity spectra of $Cr_xFe_{1-x}S_2$ crystals ..... 84
Figure 4.15 Magnetic properties of $Cr_xFe_{1-x}S_2$ crystals ..... 85
Figure 4.16 DFT results for $Cr_xFe_{1-x}S_2$ ..... 88

# LIST OF TABLES

Page


Table 3.1 ICP-MS results of a typical undoped single crystal pyrite ..... 29
Table 3.2 Fit parameters used in Figure 3.3 ..... 35

Table 4.1 [Co] uniformity in $Co_xFe_{1-x}S_2$ crystals ..... 49
Table 4.2 ICP-MS results of a typical Co-doped ([Co] = 333 ppm) crystal ..... 50
Table 4.3 Results of Curie-Weiss fits of $Co_xFe_{1-x}S_2$ crystals ..... 61
Table 4.4 [Ni] uniformity in $Ni_xFe_{1-x}S_2$ crystals ..... 65
Table 4.5 ICP-MS results of a typical Ni-doped ([Ni] = 558 ppm) crystal ..... 66
Table 4.6 Transverse (TO) and longitudinal (LO) optical phonon modes of pyrite ..... 68
Table 4.7 Results of Curie-Weiss fits of $Ni_xFe_{1-x}S_2$ crystals ..... 70
Table 4.8 [Cr] uniformity in $Cr_xFe_{1-x}S_2$ crystals ..... 72
Table 4.9 ICP-MS results of a typical Cr-doped ([Cr] = 33 ppm) crystal ..... 74
Table 4.10 Results of Curie-Weiss fits of $Cr_xFe_{1-x}S_2$ crystals ..... 75

# ACKNOWLEDGMENTS

Firstly, I'd like to thank my committee chair and advisor, Matt Law, for his guidance and support over the years. I'm continually impressed by the breadth and depth of his knowledge. I'm grateful that he encouraged us to be as hands on with our own research as possible. I learned a great deal about a wide variety of experimental techniques and practices, something not every graduate student gets to do.

There are many people I would like to thank for making the work detailed in this dissertation possible. I would like to thank Prof. Ruqian Wu and Dr. Jeonwoo Kim for supplying the DTF calculations seen here. I'd like to thank Prof. Kathleen Johnson for letting us use her ICP-MS and her grad students, Chris Wood and Kevin Wright, for helping me maintain and upkeep the instrument. I want to thank Dr. Ignacio Martini at UCLA, for his assistance with the magnetization measurements.

The facility staff at UCI was incredible and I appreciate their time and support. I want to thank Lee Moritz and Mark Steinborn of the Physical Sciences Machine Shop, Dr. Qiyin Lin, Dr. Ich Tran, and Dr. Jian-Guo Zheng of IMRI, and Cyril McCormick of the electronics shop.

I also want to thank the IRMI staff for hiring me as a lab assistant in the Surface Science Facility. Although it was time consuming and occasionally frustrating, being able to use, maintain, and assist users with experiments on a multi-million dollar instrument was overall an enjoyable experience.

I had the pleasure of working alongside a lot of great people over my tenure at UCI. I want to thank: Dr. Moritz Limpinsel, Dr. Vineet Nair and Dr. Jason Tolentino for their help and guidance when I first joined that lab. Dr. Nima Farhi, my PIP (partner-in-pyrite), for his part in the work presented here. As well as the other members of the Law group: Dr. Amanda Weber, Mohammed El Makkaoui, Dr. Zhongyue Laun, Dr. Kan Fu, Glen Junor, Juliette Micone, Alex Ableson, Dr. Christian Engelbrekt, Dr. Darren Neo, Dr. Chao Yi, Caroline Qian, Yash Gargasya, and Andy Yang. Thank you all for your help and camaraderie.

I'm grateful for all the many friends I've made along the way. You guys made grad school a more enjoyable experience.

I'd like to thank give a big thank you to my family, for their love and encouragement. I love you all.

Lastly, I'd like to thank Dr. Kate Rodriguez. (Even though she didn't thank me in her dissertation, its fine. I'm not even bitter about it.) You helped me keep my sanity during all this. Without you I don't know if I would be where I am today. Thank you.

# CURRICULUM VITAE

Trenton Salk

## EDUCATION

**Doctor of Philosophy in Physics** **2019**
*University of California, Irvine (UCI)* *Irvine, CA*

**Master of Science in Physics** **2019**
*UCI* *Irvine, CA*

**Bachelor of Arts in Physics** **2013**
*University of California, Davis (UCD)* *Davis, CA*

## RESEARCH EXPERIENCE

**Graduate Student Researcher** **2013-2019**
Matt Law Lab, Department of Chemistry, *UCI* *Irvine, CA*

**Lab Assistant** **2015-2019**
Surface Science Facility, IMRI, *UCI* *Irvine, CA*

**Undergraduate Student Researcher** **2011-2012**
Dong Yu Lab, Department of Physics, *UCD* *Davis, CA*

## PUBLICATIONS

**The Effect of Co, Ni, and Cr Impurities on the Electronic, Optical, and Magnetic Properties of Iron Pyrite Single Crystals** **2019**
T. Salk, N. Farhi, A. Weber, J. Kim, R. Wu, and M. Law
*In Preparation*

**Reversible Aggregation of Covalently Cross-Linked Gold Nanocrystals by Linker Oxidation** **2019**
Z. Luan, T. Salk, A. Abelson, S. Jean, and M. Law
*Journal of Physical Chemistry C*

**Collective topo-epitaxy in the self-assembly of a 3D quantum dot superlattice** **2019**
Abelson, C. Qian, T. Salk, Z. Luan, K. Fu, J. G. Zheng, J. L. Wardini, and M. Law
*Nature Materials*

# ABSTRACT OF THE DISSERTATION

Iron Pyrite Single Crystal Studies

By

Trenton Salk

Doctor of Philosophy in Physics

University of California, Irvine, 2019

Professor Matt Law Irvine, Chair

Iron pyrite ($FeS_2$) is an earth-abundant, non-toxic material that has a suitable band gap of 0.95 eV, a large optical absorption coefficient, and adequate carrier diffusion lengths for use in photovoltaic applications. However, its practical use is limited in part by poor understanding and control of doping. Here, we employ variable temperature Hall effect, electrical conductivity, optical transmission spectroscopy, and magnetization measurements supported by density functional theory (DFT) calculations to study, in detail, the impact of three transition metal impurities (cobalt, nickel, and chromium) on the properties of ultrapure pyrite single crystals grown in sodium polysulfide. By studying samples as a function of impurity concentration, we conclusively establish that cobalt is a nearly ideal donor in the dilute limit (<500 ppm Co) with a defect state that lies above the conduction band minimum, while nickel and chromium act as deep donors that barely affect the carrier concentration. Broad sub-band gap absorption features in the optical spectra of $Co_xFe_{1-x}S_2$, $Ni_xFe_{1-x}S_2$, and $Cr_xFe_{1-x}S_2$ samples are assigned using DFT models to specific electronic transitions between the impurity states and the pyrite bands. We also observe at low temperature several series of sharp absorption

peaks in $FeS_2$, $Ni_xFe_{1-x}S_2$, and $Cr_xFe_{1-x}S_2$ that are likely caused by excitons and associated phonon replicas. Magnetization data are consistent with the other results and show that $Co_xFe_{1-x}S_2$ magnetic behavior is similar to undoped samples at low Co concentration – indicating that cobalt donates one electron to the lattice to form nonmagnetic low-spin $Co^{3+}$ – and develops a much larger paramagnetic response at higher Co concentrations owing to the increased Pauli paramagnetism from free carriers and paramagnetic behavior of occupied Co defect states (low-spin $Co^{2+}$). $Ni_xFe_{1-x}S_2$ acts as a well-behaved Curie paramagnet at all temperatures and concentrations explored with a charge state of $Ni^{2+}$ deduced from the magnetic susceptibility, in agreement with DFT results. $Cr_xFe_{1-x}S_2$ also behaves as Curie paramagnets at all concentrations. While DFT calculations, in conjunction with electrical and optical data, indicate that Cr preferentially forms $Cr_{Fe}$–$V_S$ pairs and should be in the low-spin $Cr^{2+}$ state, susceptibility data shows Cr takes several electron configurations (low-spin $Cr^{2+}$, high-spin $Cr^{2+}$, and $Cr^{3+}$) with some combination of each likely present in each sample. This discrepancy is not yet understood. By analyzing the results of each measurement (with exception of the Cr magnetic data), in conjunction with DFT calculations, we establish a self-consistent picture of the defect energy levels for each element. We determine that the $Co_{Fe}$ defect state lies ~70 meV above the conduction band minimum, while $Ni_{Fe}$ and $Cr_{Fe}$ reside 378 and 209 meV below the conduction band, respectively. These results establish the basic doping behavior of three elements and provide a pathway for overcoming the key challenges to rational doping in pyrite.

# Chapter 1

# Introduction

## 1.1 The Energy Crisis and Solar Power

In 2018 global energy consumption was 18.6 terawatts (TW), up 2.9% from 2017, the largest rise seen in the past decade [1]. While generation of energy expanded for almost all sources, nearly 70% of this increased demand was met by fossil fuels. As a result, global energy-related $CO_2$ emissions rose by 1.7%. Experts project global energy consumption to increase an additional 50% by 2050 [2]. One of the greatest challenges of our time is to meet this growing demand without further damaging the environment and polluting our environment by finding cheap, clean and safe alternatives to fossil and nuclear fuels. Solar energy has the ability to meet these conditions and provide the world with the power it needs.

Over $10^4$ TW of solar energy strikes the earth's surface each year. Less than 2 hours of radiation from the sun has enough potential energy to meet global demands for a year. While there are several methods used in attempts to harness this energy including solar thermal (using heat from the sun to heat a medium) and solar fuel production (using solar light to drive

photochemical reactions), the most well-known method is to utilize the photovoltaic effect in semiconductors to generate electricity directly.

Photovoltaic (PV) panels have been used since the 1950s, but the high cost of solar cell fabrication has limited them to applications such as satellites, off grid installations and mobile devices. However, over the last decade we've seen a tremendous change in the PV market and for the first time solar energy has become price-competitive with fossil fuels. This resulted from large decreases in PV panel costs due to extensive advancements in material science research, improvements in fabrication techniques, and economies of scale. These advancements were driven in part by government subsidies and initiatives, such as the Department of Energy's SunShot Initiative [3], who's goal of reducing utility scale solar power generation from 28 ¢/kWh in 2010 to 6 ¢/kWh by 2020 was met in 2017 (Fig. 1.1). Despite such a drastic reduction in cost, solar energy only made up 1.6% of US power production in 2018 [1]. In order to promote widespread adoption and disrupt the current fossil fuel dominated market, PV panel costs need to be further reduced.

The most common PV devices seen are the traditional single crystal silicon p-n junction panels. They have benefited from the decades of extensive research on silicon's fabrication and material properties, leading to highly efficient and stable solar panels. However, further reductions in its manufacturing cost are difficult do to the energetically demanding processes needed to produce the high quality single crystal silicon necessary for efficient device performance. Due to its poor light absorption properties, thick layers (typically ~300 μm) are needed for sufficient light capture. In order to extract these photo-generated carriers for

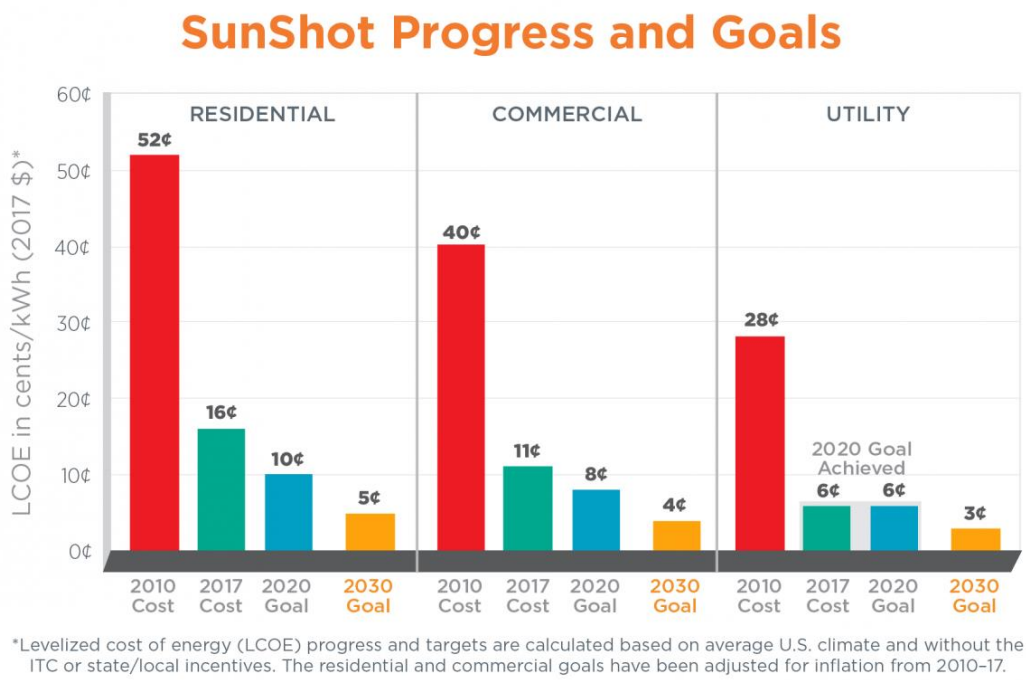


Figure 1.1 SunShot initiative progress and goals [3]. The 2020 goal of achieving 6 ¢/kWh at the utility scale was met in 2017, with the new goal of reaching 3 ¢/kWh by 2030.

electrical use diffusion lengths on the order of the sample thickness are needed. For the thicknesses required in silicon devices, the silicon used has to be very pure and high quality. These prerequisites for efficient silicon devices (thick, high purity/quality) increase panel production costs.

Materials with stronger absorption properties require much thinner absorber layers than traditional crystalline silicon cells, potentially reducing production costs, and are used to fabricate "thin film" PV devices. CdTe and $CuIn_{1-x}Ga_xSe_2$ (CIGS) are currently the most popular thin film materials in use with reported device efficiencies of 22.1% and 23.4% respectively [4]. However, concerns about the toxicity of Cd and the scarcity of tellurium and indium limit the viability of the large-scale production of these panels needed to meet the 10's of TW of global

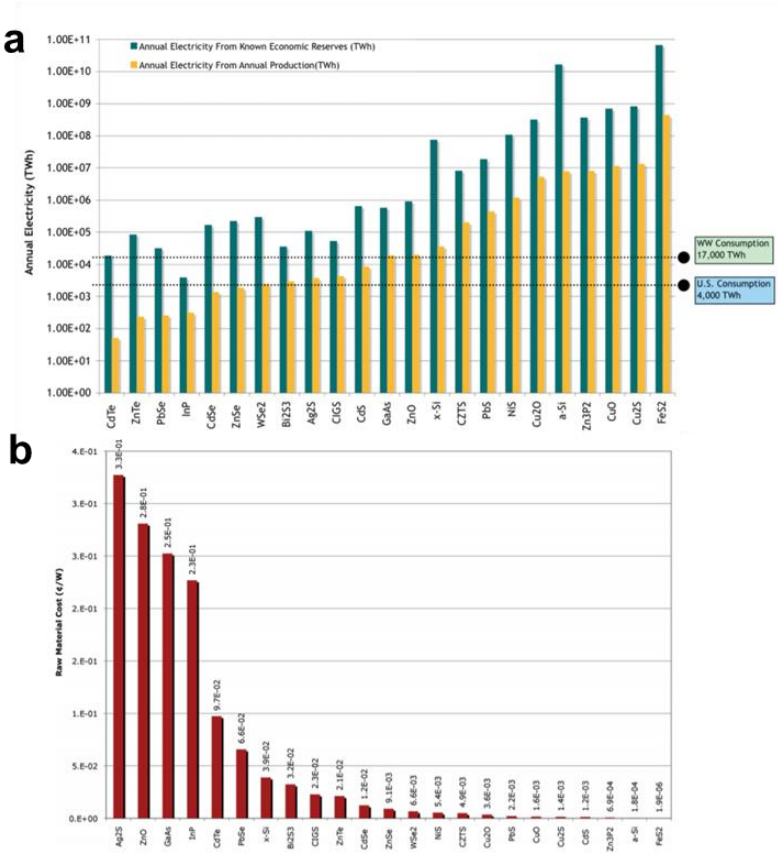


Figure 1.2 Annual potential electricity production and raw material cost for 23 inorganic PV materials. (a) Annual potential electricity production based on known economic reserves (blue) and annual production (yellow). (b) Raw material costs in ¢/W. Images taken from [5].

energy demand. Therefore, we require a thin film material that is cheap, non-toxic, and earth abundant in order to sustain the growth in global energy consumption in an environmentally friendly way.

In a 2009 study by Wadia et.al., iron pyrite ($FeS_2$) was identified as having highest potential for TW-scale solar deployment among 23 inorganic photovoltaic materials [5]. The materials were evaluated on the basis of potential annual power production (determined from reported band gap values and material availability) and materials extraction costs. As can be seen from figure 1.2, iron pyrite ($FeS_2$) had both the highest potential power production and lowest extraction

costs. Composed of only iron and sulfur, pyrite meets the requirements of cheap, non-toxic, and earth-abundant for an ideal thin film PV material.

## 1.2 Iron Pyrite ($FeS_2$)

Iron pyrite ($FeS_2$), commonly known as fool's gold, forms in a NaCl-like crystal structure ($Pa\bar{3}$), with the $Fe^+$ ions occupying the Na positions and <111> oriented S-S dimers occupying the Cl positions (Fig. 1.3). The pyrite crystal structure ($MX_2$) is adopted by many transition metals M and chalcogens X= O, S, Se, Te, including cattierite ($CoS_2$) and vaesite ($NiS_2$). $FeS_2$ also forms a metastable phase, the orthorhombic marcasite. Its formation energy is slightly higher than that of pyrite, therefore it's easily converted by thermal annealing. However, a sulfur-rich environment is necessary during annealing to prevent sulfur loss and the formation of sulfur deficient phases, such as greigite (Fe3S4), smythite (Fe9S11), pyrrhotite ($Fe_7S_8$) and troilite (FeS).

Research on pyrite started in the mid 1980's due to its potential as an ideal PV material for sustainable, low-cost, TW-scale solar energy conversion. It is composed of earth-abundant, nontoxic, inexpensive elements, has an optical band gap of ~0.95 eV (theoretical maximum efficiency of 30.5% according to the Shockley−Queisser limit with AM 1.5 light, slightly less than the 33.7% limit for an ideal 1.34 eV band gap [6]) and strong light absorption (with an absorption coefficient $\alpha > 10^5$ for $h\nu > 1.3$ eV) allowing >90% of sun light to be absorbed with only 100 nm thick layers [7]. Additionally, reported room-temperature electron mobility values

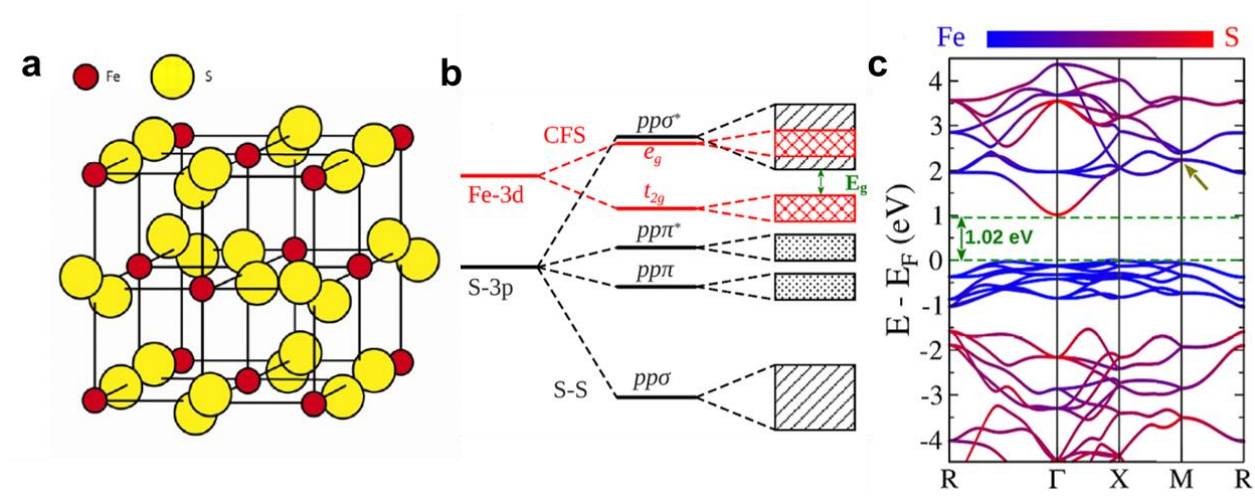


Figure 1.3 Unit cell and band diagrams of iron pyrite. (a) Unit cell of FeS2, adapted from [8]. (b) Schematic band structure derived from atomic Fe and S states. (c) DFT calculated band structure, the color scale indicating Fe and S contributions. (b) and (c) and reproduced from [9].

up to 360 $cm^2V^{-1}s^{-1}$ [10], quantum efficiencies > 90% at 1.26 eV [8], and minority carrier diffusion lengths (100−1000 nm [11,12]) exceeding the thickness needed for complete light absorption make pyrite a truly intriguing material for PV applications.

Despite these appealing properties, pyrite faces three interrelated issues that have so far limited its potential for TW-scale power production. First, pyrite based PV devices suffer from a disappointingly low photovoltage ($V_{OC}$ <200 mV) that limits power conversion efficiencies to < 3% percent [7,13], an order of magnitude lower than the theoretical maximum. Second, pyrite surfaces are rich in electronically active defects that cause Fermi level pinning with strong upward band bending [14,15], surface conduction [16–18], fast recombination [14,19], and the possibility for narrowed surface band gaps [20,21], all of which complicate junction formation [22,23]. Third, the doping of pyrite is poorly understood and poorly controlled, which hinders the progression of fundamental understanding of pyrite and prevents rational device

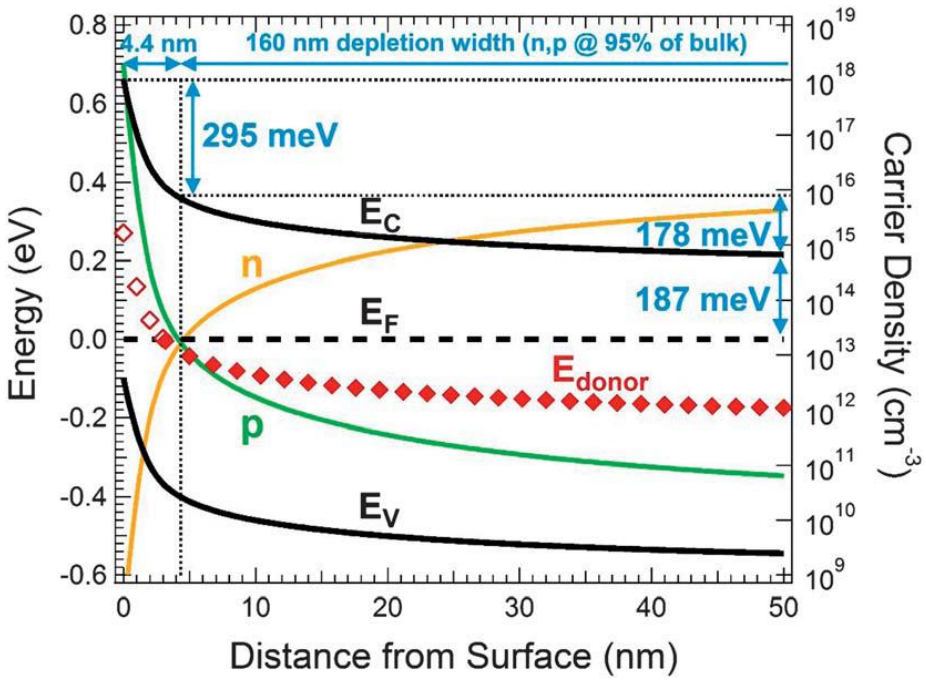


Figure 1.4 Calculated equilibrium band diagram of the pyrite surface at 300 K. Image taken from [16]

engineering [16–18,24,25]. Our lab has demonstrated that high-quality, ultrapure synthetic pyrite single crystals grown by a flux technique feature conductive, *p*-type surfaces (caused by a high density of shallow acceptors pinning the Fermi level near the valance band edge) surrounding interiors made *n*-type by a high concentration of native deep donors [16], while recent work has provided transport evidence indicating sulfur vacancies are responsible for these states [26]. Ionization of these donors near the surface augments the strong electric field of this inversion layer, resulting in a thin triangular potential barrier at the pyrite surface (Fig. 1.4). Following the work of Bronold *et al*. [14], we [16] and then others [19] argued that thermionic-field emission through this triangular surface barrier may be responsible for the large reverse saturation current, poor rectification, and low photovoltage of pyrite devices.

## 1.3 Scope of This Work

This work utilizes combined electrical, optical, and magnetic measurements of ultrapure single crystals doped with individual elements in order to highlight an avenue to achieve better understanding and control of doping in pyrite. Chapter 2 gives an overview of the experimental techniques and computational methods used in this work. Chapter 3 further explores the intrinsic properties of our flux grown crystals to gain a better understanding of the magnetic and optical properties of such high purity samples, in addition to the electronic behavior already studied. In chapter 4 the results of undoped crystals are used as a point of comparison to the properties of flux-grown $Co_xFe_{1-x}S_2$, $Ni_xFe_{1-x}S_2$, and $Cr_xFe_{1-x}S_2$ crystals, in order to establish the basic doping behavior of Co, Ni, and Cr and improving our understanding of the bulk defect chemistry of pyrite.

# Chapter 2

# Methods

## 2.1 Single Crystal Synthesis

Iron pyrite single crystals were the basis of these studies. In order to eliminate uncertainty in the results of our experiments, crystal purity and structural quality were of vital importance. The high purity crystals used in these experiments were synthesized via a flux growth technique unique to our lab, first established by Nick Berry and later optimized by Dr. Nima Farhi. This synthesis was first published in [16] and is described in detail below.

### 2.1.1 Flux Growth

Pyrite singles crystals were formed in a sodium polysulfide flux by heating an evacuated quartz ampule containing a crucible filled with high purity iron, sulfur and sodium sulfide to 780°C and then cooling over a ~24h period. Sodium sulfide was chosen as a flux material due to the low melting point sodium polysulfide has over a wide range of compositions and temperatures (see

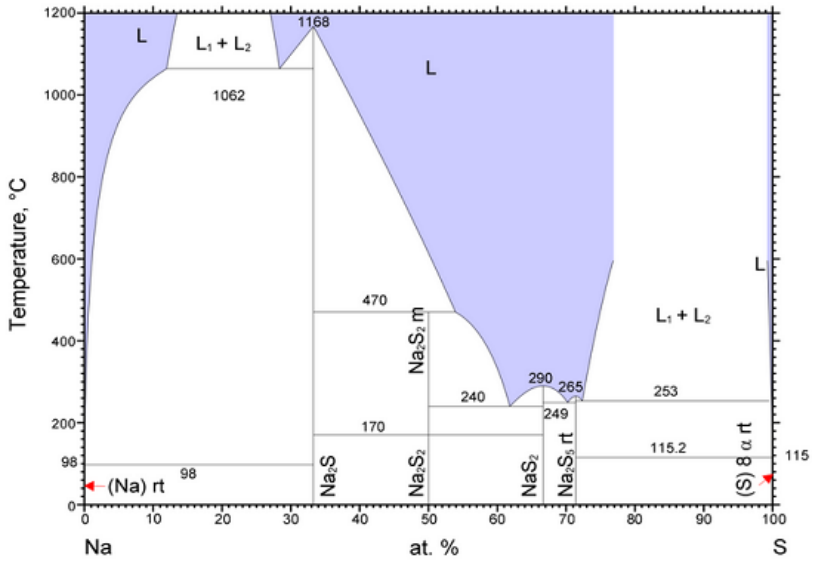


Figure 2.1: Na-S binary phase diagram (data from [27]). The Na-S system has eutectic points as low as 240°C and a large region of binary liquid immiscibility above 253°C near the sulfur-rich end of the system.

Fig. 2.1), shares a common anion with pyrite, and has an cation that has been shown to not incorporate into the crystal to any significant degree [16].

Before the synthesis, the high purity precursors are first further purified. Iron powder (99.998%, 22 mesh, Alfa Aesar) is placed into a pyrolytic boron nitride (pBN) crucible and centered in a horizontal tube furnace. The iron was then reduced at 300°C under a flow of 5% $H_2$/95% Ar for 15 hours in order to remove moisture and any oxides that may have formed. Sulfur powder (99.9995%, Alfa Aesar) was dried and degassed by heating in a quartz round bottom flask at 130°C for 3 hours under vacuum (~30 mTorr). $Na_2S \cdot 9H_2O$ (> 99.99%, Aldrich) was first crushed, then dried and degassed under vacuum (~30 mTorr) at 300°C for 5 hours, resulting in a powdered mixture of white $NaS_2$ and yellow polysulfide. After purification, each precursor's vessel was back filled with Ar, sealed air tight and immediately transferred into a $N_2$ filled

glovebox (< 0.1 ppm $O_2$). The precursors were then removed from their respective vessels for storage.

While in the glovebox, 0.50 grams of iron powder (8.9 mmol), 0.71 grams of $NaS_2$ (9.1 mmol), and 1.29 grams of sulfur are loaded into either an alumina crucible (99.5%, LSP Ceramics) or pBN crucible (99.999%, Morgan Technical Ceramics). The crucible is then placed into a half sealed quartz tube. The other end was then attached to a rubber collar with a shut off valve. The collar/quartz tube were brought out of the glovebox and attached to a vacuum system. Before opening the shut off valve to the crucible, the vacuum system was first pumped to <10 mTorr then backfilled with Ar (99.999%). This pump/purge procedure was repeated 3 times. The quartz tube was then evacuated to <10 mTorr and sealed shut with a hydrogen/oxygen torch. The quartz ampule was placed at the center of a vertical furnace, heated to 780°C at a rate of 13°C/min, held at 780°C for 6 hours, cooled to 625°C over 24 hours, then cooled to room temperature naturally (typically ~5 hours). The crucible was then removed from the ampule and placed in a bath of Millipore water for several hours in order to dissolve the $NaS_2$ flux. The resulting pyrite crystals were sonicated in Millipore water to remove residual flux, further rinsed with Millipore water, and then brought into the glovebox for storage.

### 2.1.2 Doped Single Crystal Growth

Controllably doped crystals were grown in essentially the same manner as described above; the only difference was the addition of the dopant into the crucible after the iron powder, but

before the other precursors. Nickel powder (99.996%, 120 mesh, Alfa Aesar), chromium(III) nitrate nonahydrate (99.99%, Aldrich), and octacarbonyldicobalt (stabilized with 1-5% hexane, Alfa Aesar) were used without further purification. To ensure an even distribution the dopants were added in solution form. We used stock solutions of 0.1M Ni dissolved in hydrazine (98%, anhydrous, Aldrich), 0.1M $Cr(NO_3)_3$ in methanol (99.8%, anhydrous, Aldrich), and 0.1M $Co_2(CO)_8$ in hexane (>99%, anhydrous, Aldrich). The desired amount of solution was diluted with pure solvent to 1 mL total volume and added over the iron. The solvents were then evaporated by heating the crucibles in a box furnace inside the glove box at 200°C for 30 minutes. The rest of the growth procedure is identical to that of the undoped crystals.

## 2.2 Sample Preparation

### 2.2.1 Sectioning and Polishing

Many characterization techniques necessitate samples that are relatively thin (such as electrical Van der Pauw measurements) with finely polished, mirror-like surfaces (such as optical transmission or surface science techniques). As such, great care was taken to optimally prepare samples that fit these conditions, resulting in parallel slabs of pyrite that has surfaces with <1 nm RMS roughness (see fig. 2.2).

Most of the crystals used in this study were prepared by first mounting the single crystals in epoxy (Buelher EpoxyCure). A slow-speed saw (Model 650, South Bay Technology) was then

used to cut ~700 µm slabs parallel to the largest high quality facet (typically {111} plane, though {210} was seen occasionally). The crystals were then soaked in dichloromethane to dissolve the epoxy. The crystal slabs were polished by mounting the slab onto a metal puck with Crystalbond™ and sequentially polishing with SiC paper of grit size 600, 800, and 1000, followed by sequential lapping with 3 µm and 1 µm diamond slurries and, finally, lapping with 50 nm $Al_2O_3$ slurry (Buehler MasterPrep) until no sign of damage is visible under a 5x optical microscope. The crystals were rotated by 90° between each polishing in order to optimally remove damage caused by the previous polishing step. Both sides of the slab were polished in this manner. Residual slurry particles were removed by sonicating in Millipore water. Polished slabs were then stored in the glovebox to reduce oxidation.

Several crystal slabs were instead prepared by using Leica EM TXP. The sample preparation with this tool was nearly identical, except the crystals no longer needed to be mounted in epoxy. Instead, the whole crystal was mounted with the target facet onto a metal chuck mount and the section was cut using diamond saw attachment. This allowed the cut surface to be polished without removing the slab. The surface was then sequentially polished with 9 µm, 5 µm, and 2 µm diamond polishing pads and finally by lapping with a 50 nm $Al_2O_3$ slurry.

### 2.2.2 Electrical Contacts

For accurate electrical characterization barrier-less, ohmic, contacts are required. Since contacts to finely polished/as-grown surfaces were often troublesome, ohmic contacts were typically made by carefully scratching the crystal to increase the local surface roughness before

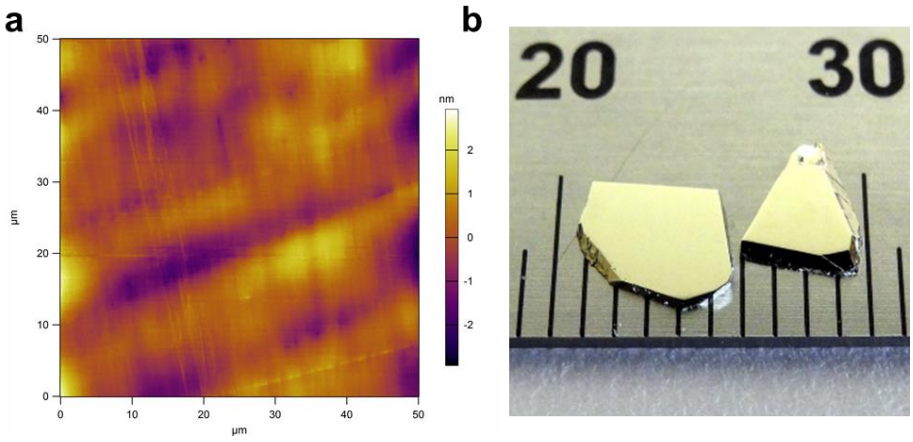


Figure 2.2: Typical pyrite sample preparation. (a) 50 µm x 50 µm AFM topography image of a typical pyrite slab polished surface showing waviness of 1-2 nm and an RMS roughness of 0.64 nm. (b) Photograph of two pyrite slabs. Ruler scale is in mm.

applying colloidal silver paste. However, these contacts to Co-containing crystals became non-Ohmic at lower temperatures. To obtain Ohmic contacts to Co-containing samples, 10-20 nm of nickel was evaporated onto the roughened corners of the crystal and then covered with colloidal silver paint, even then Co-doped samples became non-Ohmic at sufficiently low temperatures.

## 2.3 Structural and Elemental Characterization

To insure our crystals were free from common phase impurities, such as its polymorph marcasite or sulfur deficient phases like pyrrhotite, and elemental contamination their structure and elemental composition were thoroughly characterized.

### 2.3.1 X-Ray Diffraction (XRD)

Single Crystal XRD data was taken on a performed on a Rigaku SmartLab diffractometer using Cu Kα radiation (λ = 1.5406 Å). X-ray rocking curves and 2Θ-ω scans were acquired on the SmartLab configured with a Ge(440) x 4 monochromator with an angular resolution of 5.4 arcseconds.

Synchrotron XRD measurements were carried out at Beamline 11-BM of the Advanced Photon Source (λ = 0.413141 Å) at Argonne National Laboratory using crushed crystals in capillary transmission mode. Lattice parameters were determined from Rietveld refinement of the XRD patterns (PDXL version 2.6.1.2).

### 2.3.2 Raman Spectroscopy

Raman spectroscopy was use to further prove disprove the existence of marcasite impurities in our crystals, since it has been shown that Raman is more sensitive in detecting marcasite than regular XRD techniques. Raman spectra were collected using a Renishaw inVia confocal Raman microscope with a 50× objective lens using a 523 nm laser at less than 5 mW. Because of the high light absorption of pyrite limits the probing of this technique to the very surface, samples were powdered right before measurement and scanned in multiple regions to ensure the data acquired was representative of the entire crystal.

### 2.3.3 Mass Spectrometry

To measure the elemental purity of our single crystals as well as quantify the dopant concentration in doped samples, A Nu AttoM High-Resolution Inductively coupled plasma mass spectrometer (ICP-MS) was used, utilizing the external calibration method. Samples were completely dissolved in double distilled trace metals basis nitric acid (TraceMetal grade, Fisher Scientific) in a Teflon-lined acid digestion vessel (Parr 4744, 45 mL) at 170°C for 4 hours. A multi-element standard (Inorganic Ventures IV-ICPMS-71A) was used to generate standard calibration curves for each element. Cobalt, nickel, and chromium were measured as $^{59}$Co, $^{60}$Ni, and $^{52}$Cr, quantified using the standard calibration curves, and corrected for isotopic abundance to obtain the total concentration of each element in ppm by mass. The results were analyzed using Nu Quant software (version 1.1135.1). Mass concentrations (ppm wt.) were converted to atomic concentrations (ppm at.) using:

$$ppm.at\ of\ x = \frac{\left(\frac{ppm.wt\ of\ x/10^6}{M_x}\right)}{\left(3\times\left(\frac{1}{M_{FeS_2}}\right)+\frac{ppm.wt\ of\ x/10^6}{M_x}\right)}\times 10^6. \qquad (2.1)$$

Where $M_{\mathrm{FeS_2}}$and $M_{\chi}$ are the molar masses of the stoichiometric $FeS_2$ and the measured element, respectively. An internal standard (VHG Labs LIS3-100) was used to correct for drift and matrix related artifacts.

Glow discharge mass spectrometry measurements were made on undoped samples by Evens Analytical Group. Powdered pyrite specimens were pressed into high purity In foil (99.99999%)

previously cleaned with acid to remove surface impurities. Impurities in the In foil were analyzed prior to elemental analysis of each sample. Glow discharge conditions of 1.0 kV, 2.0 mA, and 100 Pa of 99.9999% Ar were used for all measurements. Samples were pre-sputtered for five minutes prior to data acquisition. The intensities of the ion beams were measured with a Faraday cup for iron, sulfur and indium isotopes and a Daly conversion detector for all analytes in the samples. The efficiency of the detectors was calibrated using 180Ta (relative isotopic abundance of 0.012%) measured on the Daly detector and 180Ta (relative isotopic abundance of 99.99%) measured on the Faraday cup during analysis of pure Ta metal. Scan points per peak were 70 channels, DAC steps of 7 with integration times of 100 and 160 ms for the Daly detector and Faraday cup, respectively.

## 2.4 Optical and Morphological Characterization

### 2.4.1 Optical Absorption Spectroscopy

Variable-temperature optical extinction spectra of double-side polished crystal slabs were acquired from 0.006 - 1.1 eV (50 - 8870 $cm^{-1}$) in transmission geometry on a Nicolet 6700 Fourier transform infrared (FTIR) spectrometer equipped with a cryostat (a Janis ST-100 for measurements from 80-350 K and an ARS DE-202 for measurements from 10-300 K). Spectra were acquired using 256 scans and a step size of 1.928 $cm^{-1}$ at a vacuum of 1-7 × $10^{-6}$ Torr. Samples were mounted to a copper disk with a 2 mm diameter circular aperture using small

pieces of double-sided copper tape for measurements down to 80 K or thermal grease (Apiezon Type N) for measurements down to 10 K. Mid-IR (0.05 – 1.1 eV) measurements were made using a XT-Kbr beamsplitter and DLaTGS (KBr) detector. Far-IR (0.006 - 0.08 eV) measurements were made using a Solid-Substrate™ (Thermo Scientific) beamsplitter and a DLaTGS (poly(ethylene)) detector.

Optical absorption coefficient spectra $\alpha(hv)$ were calculated from measured transmittance (T) spectra using the equation for the total transmittance of a thick absorbing slab at normal incidence including multiple internal reflections but neglecting interference effects [28]:

$$T = \frac{(1-R)^2 \exp(-\alpha d)}{1-R^2 \exp(-2\alpha d)} \tag{2.2}$$

Where d is the slab thickness (determined with digital calipers) and R is the reflectance reflectivity of the air-pyrite interface, given by:

$$R = \frac{(n-1)^2+k^2}{(n+1)^2+k^2}. \tag{2.3}$$

Values for the index of refraction ($n$) and extinction coefficient ($k$) of pyrite were taken from spectroscopic ellipsometry measurements of our synthetic pyrite single crystals. Given practical limits on sample thickness (d > 30 μm) and transmittance sensitivity (T > 0.001), accurate absorptivity measurements were possible only for $\alpha < \sim 500$ cm$^{-1}$. Some samples were also measured on a PerkinElmer Lambda 950 spectrophotometer equipped with the cryostats in

order to extend the FTIR data to higher photon energy and larger maximum $\alpha$. In both cases, transmission spectra of the empty copper disk served as the background. Backgrounds were taken at each measured temperature to account for thermal expansion of the cryostat cold finger, which alters the intensity of light passing through the copper disk.

### 2.4.2 Spectroscopic Ellipsometry

The complex index of refraction ($\widetilde{N} = n + ik$) was measured over the wavelength range of 0.14-30 um at J.A. Woollam using an IR-VASE and VUV-VASE spectroscopic ellipsometer.

### 2.4.3 Atomic Force Microscopy (AFM)

Surface topography was measured using an Asylum MFP-3D atomic force microscope (AFM) in tapping (AC) mode using AC160TS-R3 (Asylum Research) tips.

## 2.5 Electrical and Magnetic Characterization

### 2.5.1 Temperature-Dependent Conductivity and Hall Effect

Temperature-dependent conductivity and Hall effect measurement where done inside a glovebox with a modified Ecopia HMS-5000 (0.55 T permanent magnet) using the Van der Pauw method [29]. Due to the unreliable electronics provided with the Ecopia system, our system was modified to use two dual-channel Keithley 2636A SMUs with each channel acting as a source/sink for each of the 4 contacts in our Van der Pauw geometry, all of which are tied to a common ground. An Arduino Uno is used to control the motor of Ecopia system responsible for moving the permanent magnets used for Hall effect measurements. A Lakeshore Cryotronics 321 temperature control unit is used to monitor and control the stage temperature. The system is operated/automated with a homemade LabView program.

The Hall coefficient was calculated as $R_{\mathrm{H}} = \frac{V_{\mathrm{H}} d}{IB}$, where $V_{\mathrm{H}}$ is the averaged Hall voltage measured, d the crystal thickness, I the applied current, and B the magnetic field strength. The Hall voltage is an average of the values measured for both magnetic field directions and perpendicular sample diagonals. Current reversal was used to eliminate Ohmic voltage drops due to misaligned contacts when measuring Hall voltages. The applied current ranged from 1 μA at 80 K to 1-2 mA at 350 K for undoped and Ni- and Cr-containing crystals. The high conductivity of Co-doped crystals required higher currents. The quality of the data was checked by ensuring <5% difference in voltage readings upon current reversal for conductivity values and <10% difference in Hall coefficient values for perpendicular directions. Carrier concentrations and mobilities were calculated using the single carrier approximation.

Samples are mounted with thermal grease (Apiezon Type N) to glass slides bonded to the sample stage. Ohmic contacts were confirmed by ensuring linear IV curves between all contacts.

### 2.5.3 Vibrating Sample Magnetometry (VSM)

To determine the magnetic properties of our samples, vibrating sample magnetometry (VSM) measurements were taken on a from 2-300 K on a Magnetic Property Measurement System SQUID magnetometer (MPMS 3, Quantum Design) equipped with a 5 T superconducting magnet. Moment vs. field (*m*-H) and moment vs. temperature (*m*-T) scans were acquired at a range of applied dc magnetic fields up to 5 T. *m*-T measurements were taken with the field applied during cooling. Samples were mounted to quarts rods with a small amount of varnish (Lake Shore, VGE-7031). An empty sample holder (quartz rod and varnish) showed a negligible diamagnetic response at all temperatures. Instrument performance was verified with a palladium reference standard, which matched tabulated values to within 0.5%. *m*-*H* scans were checked for reversibility and linearity. Temperature dependent susceptibility measurements were taken with fields in the range of 4-10kOe, with the field applied during cooling. The effective magnetic moment $\mu_{eff}$ of the Co, Ni, and Cr impurities was calculated by fitting the temperature-dependent molar susceptibility $\chi_{mol}$ (expressed in terms of moles of Co, Ni, or Cr, as determined by ICP-MS), in the temperature region dominated by Curie-Weiss behavior, to a model that includes a Curie-Weiss term and a temperature independent constant with the following expression,

$$\chi_{mol} = \frac{C_m}{(T-\theta)} + \chi_0. \quad (2.4)$$

Where $C_m$ is the Curie constant, *T* is the absolute temperature, *Θ* is the Curie-Weiss temperature, and $\chi_0$ is a constant that accounts for an essentially temperature independent Van Vleck or Pauli susceptibility (see below). The effective magnetic moment is then determined from the expression $\mu_{\text{eff}} = 2.83\sqrt{C_m}$ [30], The spin-only formula $\mu_{\text{eff}} = \sqrt{n(n+2)}$ was then used to estimate the number of unpaired electrons (*n*) per impurity atom. Magnetic data in this paper are reported in Gaussian cgs units.

Powderized samples were measured by loading the sample into a plastic capsule that was then lodged into a straw and inserted into the instrument. The diamagnetic response from the straw holder dominated much of the signal until the paramagnetic response from the sample was strong enough to overcome it.

## 2.6 Data Modeling and DFT Calculations

To help interpret our experimental data, modeling and density function theory calculations were utilized. The specifics of these calculations are detailed below.

### 2.6.1 Charge Transport

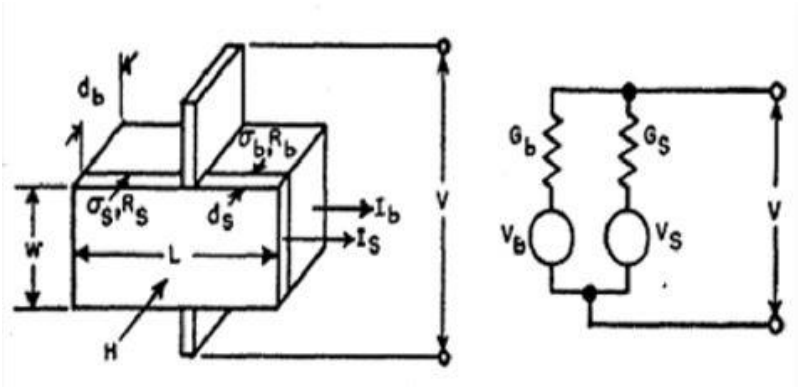


Figure 2.3: Conductivity and Hall effect of a multilayer system established by Petritz. The subscripts s and b denoted properties of the surface and bulk respectively. Image taken from [31].

In order to accurately replicate our electrical data a multilayer conduction model needed to be utilized. This conduction model was pioneered by Petritz [31] and first applied to the conduction in pyrite by Dr. Moritz Limpinsel [16]. The crux of the model assumes that conduction in our samples happens in three parallel layers; the n-type bulk and two identical p-type surface layers (see Fig. 2.3).

Here we calculate the carrier concentrations (n and p), conductivity (σ), and Hall coefficient ($R_H$) of each layer by using the charge neutrality condition

$$N_D^+ + p = N_A^- + n. \tag{2.4}$$

Where $N_D^+$ and $N_A^-$ are the concentrations of ionized donors and acceptors, given by [32]

$$N_D^+ = \frac{N_D}{1+ e^{\frac{(E_F(T)-E_D)}{k_bT}}} \tag{2.5}$$

and

$$N_A^- = \frac{N_A}{1+ e^{\frac{(E_A - E_F(T))}{k_bT}}} \tag{2.6}$$

respectively. Where here $N_D$ and $N_A$ are the concentration of donors and acceptors and $E_D$ and $E_A$ are their respective energies. The carrier concentrations $n$ and $p$ are given by

$$n = \int_{E_C}^{\infty} DOS(E) \left( \frac{1}{e^{\frac{E- E_F(T)}{k_bT}} +1} \right) dE \tag{2.7}$$

and

$$p = \int_{-\infty}^{E_V} DOS(E) \left( 1 - \frac{1}{e^{\frac{E- E_F(T)}{k_bT}} +1} \right) dE. \tag{2.8}$$

In this work, we assume a parabolic DOS. The fits worked by self-consistently solving for the temperature dependent Fermi level $E_F(T)$. This was done by inserting eqn. (2.5) through (2.8) into eqn. (2.4) and solving for $E_F$ at each temperature. Using $E_F(T)$ we solved for n(T) and p(T), from which we can then calculate σ(T) and $R_H(T)$ from the generalized expressions:

$$\sigma = e(p\mu_h - n\mu_e) \tag{2.9}$$

and

$$R_H = \frac{p\mu_h^2 - n\mu_e^2}{e(p\mu_h - n\mu_e)}. \quad (2.10)$$

The overall sample properties were then calculated by combining the bulk and surface contributions using [31]

$$\sigma_{total} = \sigma_b \frac{d_b}{d} + 2\sigma_s \frac{d_s}{d} \quad (2.11)$$

and

$$R_{H,total} = R_{H,b}\left(\frac{\sigma_b}{\sigma_{total}}\right)^2 + 2R_{H,s}\left(\frac{\sigma_s}{\sigma_{total}}\right)^2, \quad (2.12)$$

where $d_b$ and $d_s$ are the thicknesses of the bulk and surface layers and $d = d_b + 2d_s$ is the total sample thickness. For this work the bulk and surface layers were assumed to be uncompensated n and p-type materials, respectively. The bulk electron mobility $\mu_{e,b}$ was determined from fits to the unipolar region of the Hall data, while the surface hole mobility $\mu_{h,s}$ was parameterized from thin film values. Therefore this routine uses 5 free fit parameters ($N_{A,s}$, $N_{D,b}$, $E_{A,s}$, $E_{D,b}$, and $\mu_{-e,b}$)

### 2.6.2 Density Functional Theory (DFT) Calculations

To help us draw a better picture of the effects of controlled doping from our results of the various property measurements on our doped crystals, density functional theory (DFT) calculations were done by Dr. Jeonwoo Kim.

DFT calculations were carried out with the projected augmented plane-wave method [33,34] as implemented in the Vienna ab initio simulation package (VASP) [35]. We described the exchange-correlation interaction among electrons by the generalized gradient approximation (GGA) [36]. The energy cutoff for the plane-wave expansion was set at 350 eV. A 3×3×3 supercell (324 atoms including a single substitutional impurity cation, giving an impurity concentration of $2.3\times10^{20}$ $cm^{-3}$) was used to approximate the relatively dilute impurity conditions of the experiments. A 4×4×4 ***k***-point mesh was used to sample the Brillouin zone. All atoms were fully relaxed until the change of the total energy was smaller than 0.01 meV. To match the band gap of pyrite to the experimental value, we included the Hubbard term ($U$ = 2 eV) that accounts for on-site repulsion of electrons localized in the Fe *d*-orbitals [37]. For consistency, $U$ = 2 eV was used for the Co, Ni, and Cr dopant atoms as well.

# Chapter 3

# Undoped Pyrite Single Crystals

## 3.1 Characterization

To explore the intrinsic properties of iron pyrite it is important to start with the highest purity and crystallographically perfect crystals as possible. The flux growth method (described in sec. 2.2.1) pioneered by Nick Berry and optimized by Dr. Nima Farhi provided crystals that met these conditions. In the following sections the structural, elemental, optical, electrical and magnetic properties of these single crystals is presented. The results shown in this chapter fully characterize these crystals and make a great reference point for the effects of the controlled doping explored in chapter 4.

### 3.1.1 Elemental Characterization

The elemental purity of our undoped crystals has been reported before showing a purity of 99.998% on a metals basis with the only elements above 1 ppm being Cr (6.4 ppm), B (6.3ppm), Si (4.2pm), Na (4.2 ppm), and Cl (1.1 ppm) [16]. In this study elemental purity was determined by high-resolution inductively coupled plasma mass spectrometry (HR-ICP-MS). We used a

combination of multi-element standards and semi-quantitative analysis to estimate the concentrations of 61 elements, 40 elements quantitatively and 21 elements semi-quantitatively (see sec. 2.3.3). We note that a small number of relevant elements were not measured with ICP-MS, including the light elements (H, Li, Be, B), the gas formers (C, N, O), the halogens, and a few others due to contamination of the shared instrument (Ca, Al, Si, P). Table 3.1 summarizes the results for a typical sample. The major contaminates seen are Na (26.7 ppm), Cr (3.1 ppm), Mn (0.2 ppm), Ni (0.4 ppm), Cu (0.4 ppm), Zn (4.1 ppm), and Se (0.2 ppm), while all other measured elements were in negligible concentrations. The sodium concentration varies widely from 1-1000 ppm depending on how thoroughly a given sample is rinsed in water prior to digestion for ICP-MS analysis. We previously showed that sodium exists as a surface residue from the $Na_2S$-based flux rather than a lattice impurity [16], so we ignore its presence here. On the basis of the ICP-MS results, we conclude that the undoped crystals have a typical impurity concentration of 8.3 ppm of the elements measured. Cu, Zn, and Se were not reported as contaminates in our previous publication because their concentration is below the detection limit of the GDMS measurement. They, along with Ni, are listed as measured impurities of our sulfur precursor, although their concentration is surprisingly high in our samples if this is the only source of these elements. Cr and Mn likely originate from our Fe precursor. The S:Fe ratio was measured, with results in the 1.972 – 1.985 range. These results deviate from the ideal 2:1 ratio likely because of sulfur loss during the sample digestion process.

Glow discharge mass spectrometry (GDMS) measurements from Li - U were conducted on undoped samples in order to look at some of the elements we didn't have access to by ICP-MS. Results were similar to those previously published, with the major impurities not reported by

| Undoped Single Crystal | | | |
|---|---|---|---|
| S:Fe = 1.98138[b] | | | |
| element | ppm at. | element | ppm at. |
| Na | 26.7362 | Te[a] | 0.0078 |
| Mg | 0.0410 | Cs | <0.0005 |
| Sc | 0.0353 | Ba | <0.0364 |
| Ti | 0.0444 | La | 0.0001 |
| V | 0.0587 | Ce | 0.0003 |
| Cr | 3.0655 | Pr[a] | <0.0002 |
| Mn | 0.1995 | Nd | <0.0006 |
| Co | 0.0321 | Sm | 0.0002 |
| Ni | 0.4413 | Eu | 0.0002 |
| Cu | 0.3614 | Gd | <0.03 |
| Zn | 4.1077 | Tb | 0.0012 |
| Ga | <0.0023 | Dy | <0.0004 |
| Ge | 0.0025 | Ho | <0.0002 |
| As | 0.0133 | Er | <0.0003 |
| Se | 0.1388 | Tm | <0.0003 |
| Rb | 0.0012 | Yb | <0.0004 |
| Sr | 0.0045 | Lu | 0.0018 |
| Y[a] | <0.0034 | Hf[a] | 0.0001 |
| Zr[a] | 0.0033 | Ta[a] | <0.0001 |
| Nb[a] | 0.0002 | W[a] | <0.0011 |
| Mo[a] | 0.0031 | Re[a] | 0.0000 |
| Ru[a] | 0.0394 | Os[a] | 0.0003 |
| Rh[a] | 0.0097 | Ir[a] | 0.0001 |
| Pd[a] | 0.0075 | Pt[a] | 0.0153 |
| Ag | <0.005 | Au[a] | <0.0015 |
| Cd | 0.0001 | Hg[a] | <0.3 |
| In | 0.0050 | Tl | <0.00005 |
| Sn[a] | 0.0034 | Pb | 0.0817 |
| Sb[a] | 0.0002 | Bi | <0.0040 |
| | | U | <0.0008 |

Table 3.1: ICP-MS results of a typical undoped single crystal pyrite reported in atomic ppm. [a] Elemental concentration determined by semi-quantitative methods. [b] Due to sulfur loss during sample preparation, the measured S:Fe deviates from the expected 2:1.

ICP-MS being B (1.1 ppm), Al (0.6 ppm), Cl (4.5 ppm), and Ca (1.1 ppm). In combination with the ICP-MS results, this leads to a total impurity concentration, ignoring Na, of ∼16 ppm. Our halogen-free flux synthesis leads to a low concentration of halides in our samples, in contrast to the relatively high levels of halides often present in CVT-grown pyrite crystals. The electronic activity of halide impurities in pyrite remains an open question. Of the elements we were unable to measure (H, C, N, O), we believe that only hydrogen and oxygen are important impurities that could be present in significant concentration. Most importantly for the work described in chapter 4, we find the average Cr, Co, and Ni concentration to be 4.4 ppm, < 0.36 ppm, and 0.84 ppm respectively in our undoped samples.

### 3.1.2 Structural Characterization

Our double-side polished slabs have irregular shapes up to 6 mm on a side (Fig. 2.2b), mis-cut angles of <6° off the (111), and good co-planarity of the front and back surfaces (to <2°). AFM topography scans of 50×50 μm regions of the polished surfaces show a long-wavelength surface waviness of 1-2 nm amplitude and a typical rms surface roughness of <1 nm (Fig. 2.2a).

X-ray diffraction (XRD) scans show that the slabs are highly perfect, phase-pure pyrite crystals. A vast majority of the crystals discussed in this thesis have a (111) orientation (Fig. 3.1a), though we occasionally see (210) oriented facets. XRD rocking curve measurements were used to determine the crystallographic quality of our single crystals. Figure 3.1b shows a peak width of 6.5 arcseconds indicating excellent structural perfection even after polishing. As a reference,

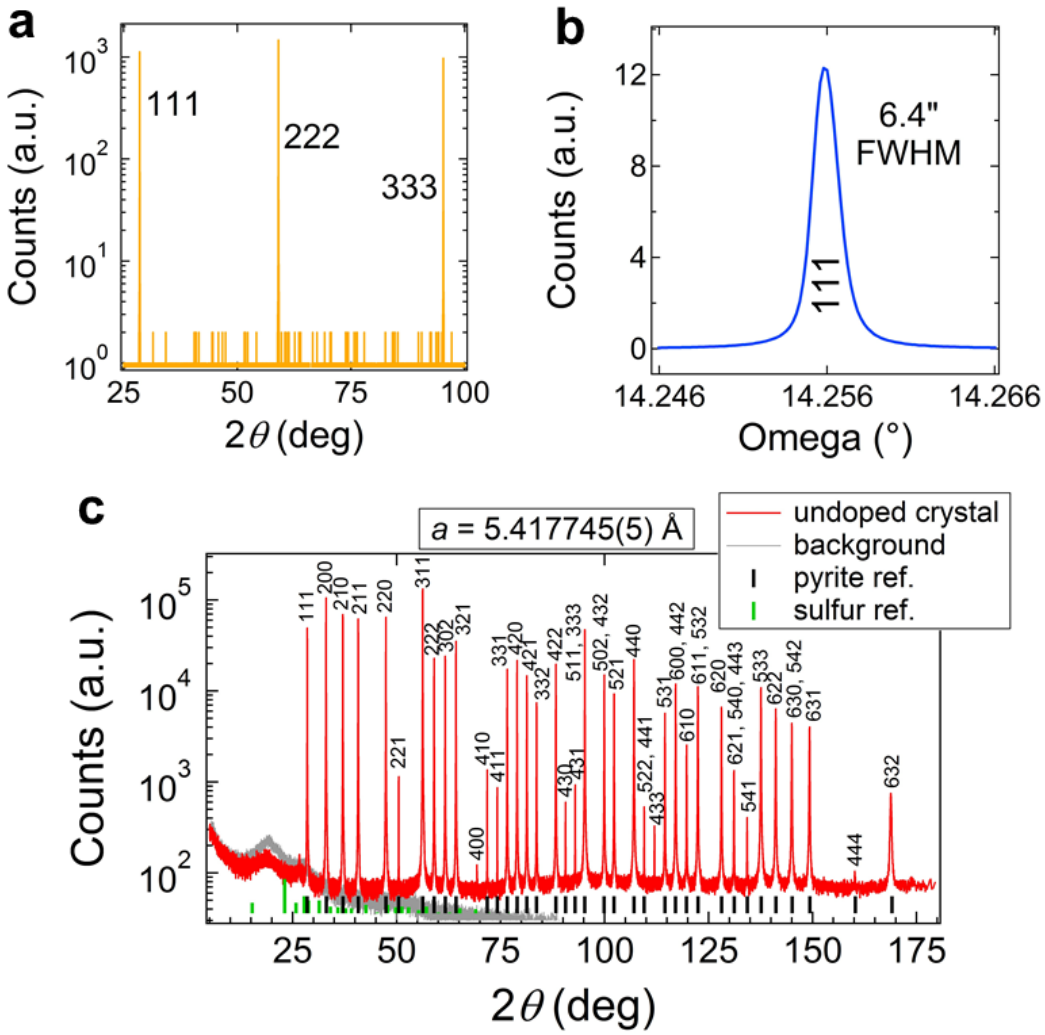


Figure 3.1: Structural characterization of undoped pyrite crystals**.** (a) 2*Θ*–*ω* XRD scan of a polished (111)-oriented pyrite single crystal slab on a log scale. (b) (111) rocking curve of a pyrite slab, showing a FWHM of 6.4 arcseconds. (c) Synchrotron XRD pattern of a powderized crystal on a log scale. All reflections index to pyrite $FeS_2$ (PDF# 00-042-1340) with the exception of the tiny peak at 26.6°. This peak is caused by residual flux and eliminated by rinsing the sample with water. Rietveld refinement of the data gives a cubic lattice parameter of 5.417745(5) Å at room temperature. The background pattern is of an empty capillary tube. Black and green bars denote the reference patterns for pyrite and orthorhombic sulfur, respectively.

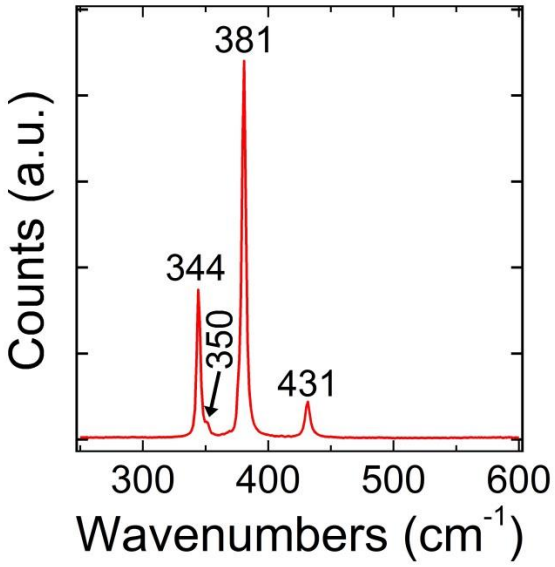


Figure 3.2: Raman spectra of a powderized single crystal showing the dominant bands of pyrite at ~344 $cm^{-1}$ and ~381 $cm^{-1}$, a small shoulder at ~350 $cm^{-1}$, and a minor band at ~431 $cm^{-1}$, corresponding to the Ag (S2 dumbbell libration), $E_g$ (S2 dumbbell stretching), $T_g(1)$, and $T_g(3)$ vibrational modes, respectively. The marcasite peak typically seen at ~320 $cm^{-1}$ is absent.

a commercial prime grade CZ-grown Si wafer had a peak width of 8.5 arcseconds. Synchrotron powder XRD is consistent with phase-pure pyrite, with no evidence for crystalline or amorphous impurities (Fig. 3.1c). We calculate a cubic lattice constant of 5.417745(5) Å from Rietveld refinement of the XRD data.

Raman spectroscopy was used as a complimentary technique to XRD to check for the presence of marcasite, a polymorph of pyrite, since it has been shown that Raman is more sensitive to in detecting marcasite than other XRD techniques. Because of the strong light absorption of pyrite, the probe depth of Raman is limited to the near surface. In an attempt to get data representative of the entire crystal, samples were powderized immediately before measurement and spectra were taken in several locations. We observed a total of four separate Raman bands from pyrite (Fig. 3.2): dominant bands at ~344 $cm^{-1}$ and ~381 $cm^{-1}$, a small

shoulder at ~350 $cm^{-1}$, and a minor band at ~431 $cm^{-1}$, corresponding to the $A_g$ (S2 dumbbell libation), $E_g$ (S2 dumbbell stretching), $T_g(1)$, and $T_g(3)$ vibrational modes, respectively. Notably the spectra is absent of the major marcasite band seen at ~315-325 $cm^{-1}$.

### 3.1.2 Hall Effect Studies

Undoped crystals were characterized by variable-temperature Hall effect, electrical conductivity (Figure 3.3). The electrical behavior of these crystals is essentially the same as described in our previous report [16], where a thin, conductive, hole-rich (*p*-type) layer at the surface of the *n*-type pyrite crystals progressively dominates transport as bulk electrons freeze out to deep donors with decreasing temperature. This transition from bulk to surface conduction manifests as a non-monotonic Hall coefficient ($R_H$) that is unambiguously negative at higher temperature (indicating *n*-type conduction), a minimum at ~140 K (depending on crystal thickness), and noisy but often positive below ~100 K (Fig. 3.3a). Good fits to the experimental data (dashed lines in Fig. 2) can be obtained using a multi-layer transport model (see sec. 2.6.1) that assumes parallel conduction via a thick bulk *n*-type layer with a high concentration of deep donors ($N_{D,bulk}$ = $10^{18}$-$10^{19}$ $cm^{-3}$, $E_C$ - $E_D$ = 380-400 meV) and a ~4 nm thick *p*-type surface layer on both sides of the crystal with a high concentration of shallow acceptors ($N_{A,surface}$ = $10^{20}$-$10^{21}$ $cm^{-3}$, $E_A$ - $E_v$ = 30-50 meV). Transport is unipolar *n*-type above ~150K, with a typical electron density (*n*) and mobility ($\mu_e$) of 2 × $10^{15}$ $cm^{-3}$ and 300 $cm^2$ $V^{-1}$ $s^{-1}$ at 300 K (Fig. 3.3b-c, Table 3.2 for exact fit results). This carrier density is about $10^3$ larger than the predicted intrinsic carrier concentration

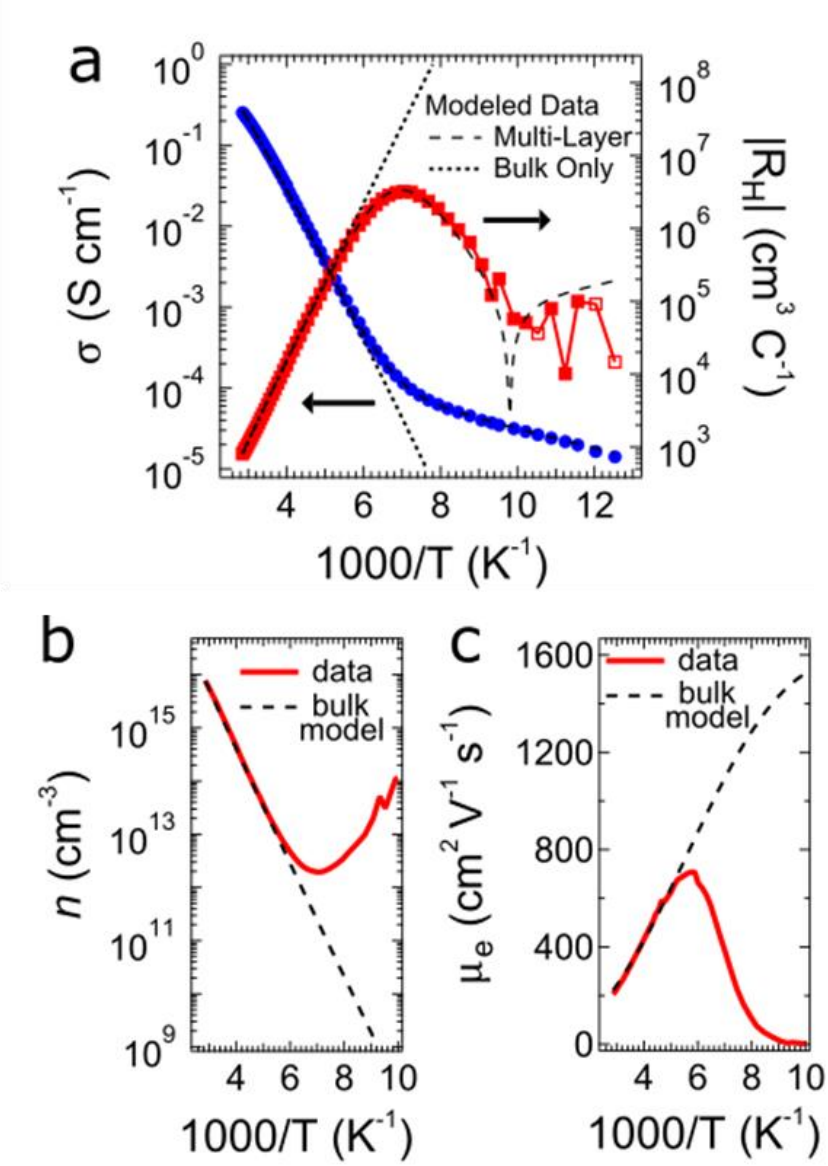


Figure 3.3: Electrical properties of undoped pyrite crystals. (a) Conductivity and absolute Hall coefficient versus inverse temperature for a typical sample (590 μm thick). Closed (open) squares represent negative (positive) values of $R_H$. Dashed lines are fits to the data using a multi-layer conduction model [16]. (b) Electron density ($n$) and (c) mobility ($\mu_e$) from 100-350 K. Solid lines are derived from the experimental data by assuming a unipolar Hall coefficient (i.e., $R_H = -1/ne$). Dashed lines are results from the model showing the behavior of the bulk electrons. The unipolar approximation ($n\mu_e^2 \gg p\mu_h^2$) is satisfied only at temperatures where the two traces overlap.

| Parameter (unit) | Fit Results |
|---|---|
| $N_D$ ($cm^{-3}$) | 3.16 x $10^{18}$ |
| $E_C - E_D$ (meV) | 400 |
| $N_A$ ($cm^{-3}$) | 5.01 x $10^{20}$ |
| $E_A - E_V$ (meV) | 35 |
| $\mu_e$ ($cm^2\ V^{-1}\ s^{-1}$) | 297 |
| $\mu_h$ ($cm^2\ V^{-1}\ s^{-1}$) | 3 |
| $d_s$ (nm) | 4.4 |

Table 3.2: Fit parameters used in Figure 3.3.

of pyrite ($n_i \sim 10^{12}$ $cm^{-3}$). Below 150 K, the samples first enter a regime of mixed conduction (where both bulk electrons and surface holes contribute substantially to the current), followed by dominant *p*-type surface conduction at lower temperatures. The origin of the unintentional *n*-type doping of bulk pyrite is well not understood, but sulfur vacancies ($V_S$) that act as deep donors are a leading suspect [7,16] and recent reports have shown good evidence of this [26]. The *p*-type surface layer also remains somewhat mysterious, but probably results from intrinsic surface states that pin the Fermi level near the valence band edge, causing surface inversion in nominally-undoped samples [15,16,18].

### 3.1.3 Optical Absorption

Spectroscopic ellipsometry (SE) was used to determine the complex index of refraction ($\widetilde{N} = n + ik$) of our synthetic pyrite crystals from 40 meV to 8.45 eV. We have previously published optical constants from a natural pyrite sample [38], here we report for the first time results from our high purity flux-grown single crystals extending into the sub-gap region (fig.

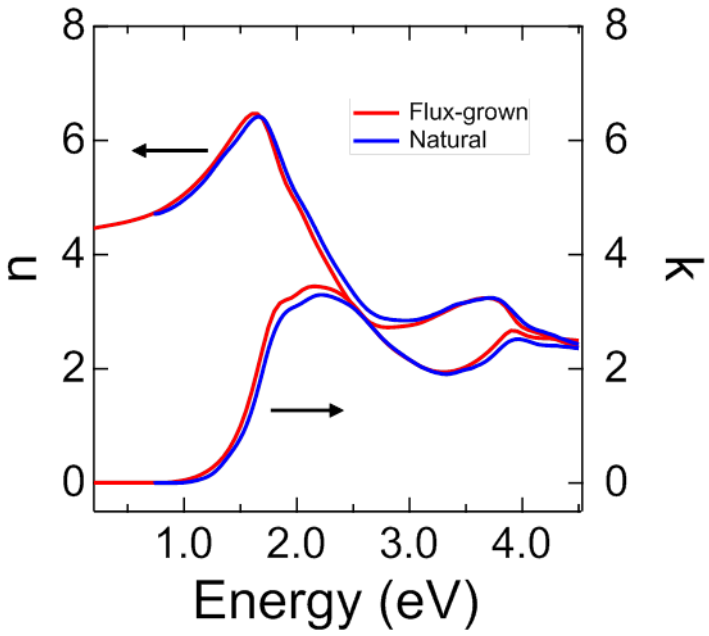


Figure 3.4: Index of refraction (n) and extinction coefficient (k) for natural and synthetic pyrite. Natural pyrite data adapted from [38].

3.4). The results are similar to those of the natural crystal. From these values we calculated the reflectivity (R) for the pyrite surface (eqn. 2.2). SE derived constants needed to be used since the crystal slabs were often too small to measure the reflectance using the integrating sphere of our UV-Vis.

Optical transmission spectra were used to determine the absorption coefficient ($\alpha$) of the undoped crystals (eqn. 2.3) at energies from below to just above the bulk band gap (0.05-1.1 eV). Figure 3.5a shows $\alpha(h\nu)$ at six different temperatures (80-340 K) for a sample with a thickness of 130 µm. We observe the expected strong absorption threshold at the bulk pyrite band gap. Tauc plots suggest that the optical band gap increases from ~0.84 eV at 340 K to ~0.95 eV at 80 K, which is similar to our previous results for crystals of this thickness [16]. Within the band gap, $\alpha(h\nu)$ is nearly flat and featureless and has a relatively small value (3-30

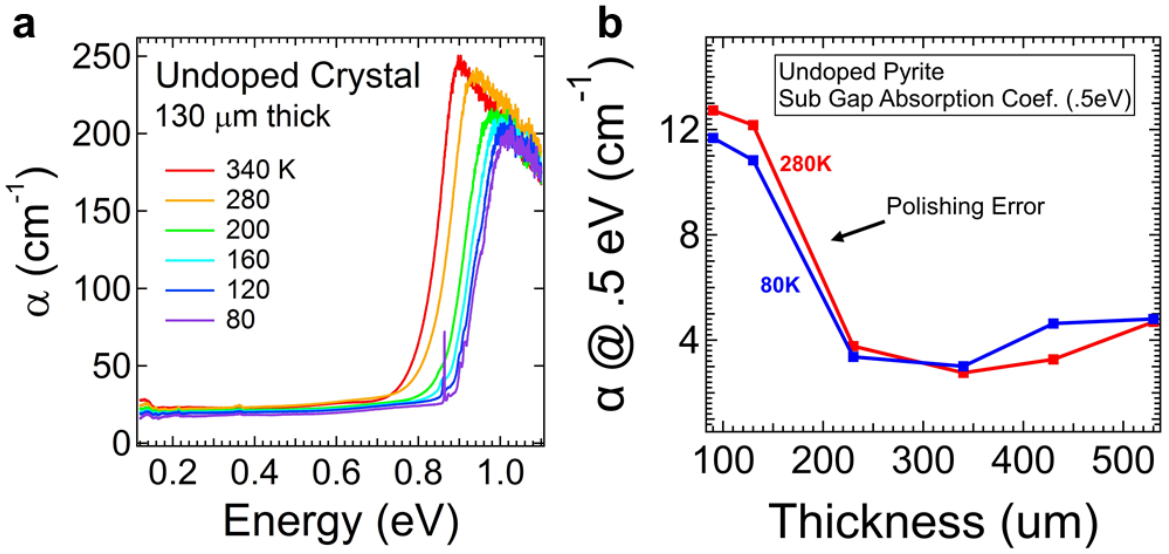


Figure 3.5: Absorption coefficient of undoped pyrite crystals. (a) Absorption coefficient as a function of energy of a polished crystal at several temperatures. The turnover in the spectra above ~0.9 eV is an instrument artifact. (b) Value of sub-gap absorption coefficient as a function of crystal thickness. The crystal was thinned from alternating sides. A polishing error occurred when thinning from 230 μm to 130 μm resulting in an apparent increase in the absorption coefficient.

$cm^{-1}$) We find that this sub-gap absorption is dependent on the quality of the polish, with poorer polishing leading to lower sub-gap transmission (Fig. 3.5b). Whether this absorption originates from increased panchromatic light absorption by near-surface holes resulting from additional surface states created by poor polishing or is an artifact due to increased scattering from surface roughness is a matter of further research. This strong dependence on surface condition makes determining if there is also a bulk component to this sub gap absorption difficult. If the sub-gap $\alpha(h\nu)$ was due to only surface effects and its absorption (or scattering) was constant, we would expect $\alpha(h\nu)$ to increase approximately as $d^{-1}$, where d is the thickness of the sample. However, we see that over several thicknesses $\alpha(h\nu)$ is roughly constant, leading us to believe that a bulk absorption could be responsible for at least some sub-gap $\alpha(h\nu)$.

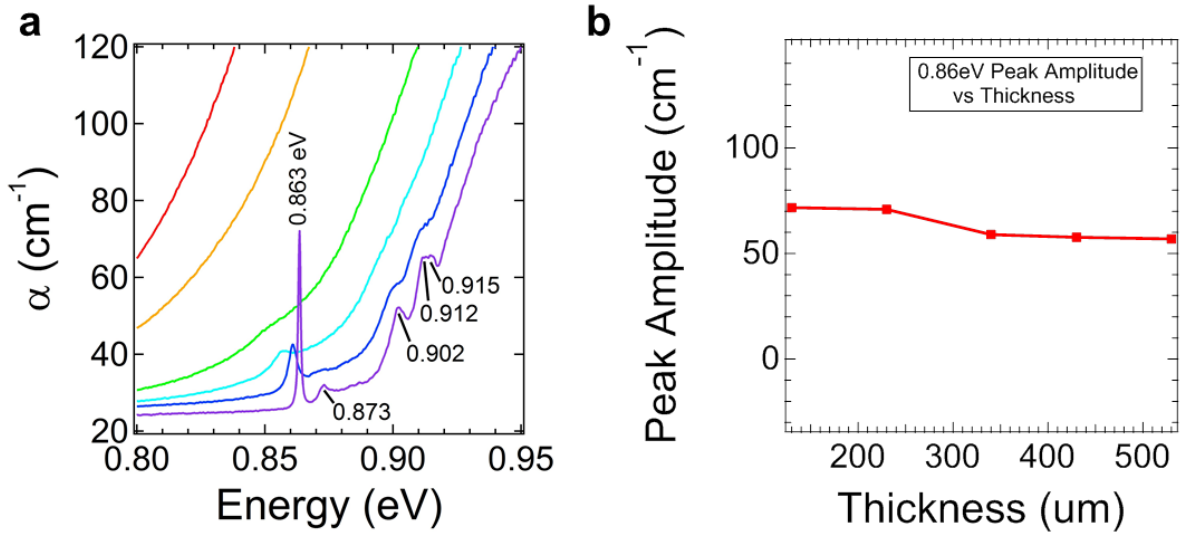


Figure 3.6: High energy spectral features of pyrite. (a) Magnified view of the same spectra as fig. 3.5 showing the characteristic series of high-energy peaks that emerges near the band edge at lower temperatures. (b) Peak amplitude (background subtracted) of $\alpha(h\nu)$ for the 863 meV peak as a function of thickness. Since $\alpha(h\nu)$ is a bulk property and independent of thickness, the peak being independent of thickness tell us this feature is also a bulk property.

Conspicuous in the optical spectra is a group of at least five sharp absorption peaks at 0.85-0.93 eV that emerges at $T < 200$ K (Fig. 3.5a & 3.6a). These peaks blue shift and become more pronounced with decreasing temperature. Their positions remain essentially unchanged at temperatures below 80 K. At 80 K, the main peak at 863 meV is quite weak ($\alpha \approx 50$ cm$^{-1}$, compared to $>10^5$ cm$^{-1}$ for energies above the band gap) but very sharp (FWHM ≈ 1 meV), while the other peaks are weaker and broader. Several of the higher-energy peaks seem to be doublets or multiplets. Since their absorption coefficient is independent of thickness (Fig. 3.6b), we believe the peaks are due to bulk states rather than states specific to the surface layer. Previous optical transmission studies of pyrite have also reported these sub-gap absorption features. Yang *et al*. assigned the peaks at 863 and 873 meV to transitions from the top of the valence band to $Cr^{3+}$ and $Cr^{2+}$ states located near the conduction band edge [39]. However, we

show below that the intensity of the sub-gap peaks actually decreases with increasing chromium concentration, which definitively rules out this explanation. In an earlier work, Kou and Seehra resolved three of the peaks (at 866, 904, and 914 meV at 80 K) and tentatively attributed the first two transitions to excitonic levels [40]. By assuming the 866 meV and 904 meV peaks were the first and second exciton they calculated a first exciton binding energy of 54 meV. However, this binding energy should be large enough for these excitonic peaks to persist well above room temperature, whereas the observed spectral features emerge only below 200 K. If we instead assume that the 873 meV peak is the second exciton, then, using the hydrogenic model, the energy separation between these peaks is [40]

$$E_{n2} - E_{n1} = \frac{\mu e^2}{2\hbar\varepsilon^2}\left(1 - \frac{1}{4}\right), \tag{3.1}$$

where ε is the dielectric constant and μ is the effective mass of the exciton. By taking the energy difference between the first and second exciton peak, we can calculate a first exciton binding energy of 12.9 meV. Such a binding energy would readily explain why the 863 meV peak only begins to be resolvable at temperatures below 160 K (where $k_b$T = 13.7 meV). These values imply a fundamental gap of 876 meV, near the electronic band gap derived previously [16]. To further asses the validity of this assignment, using ε = 21 [38,41] and an effective electron mass of 0.49 $m_e$ [37], we calculate the necessary effective hole mass to obtain our 12.9 meV binding energy and get a value of 2.26 $m_e$, which is in agreement with experimental results [13]. Although the absorption coefficient for the 863 meV peak is smaller than typically seen in a

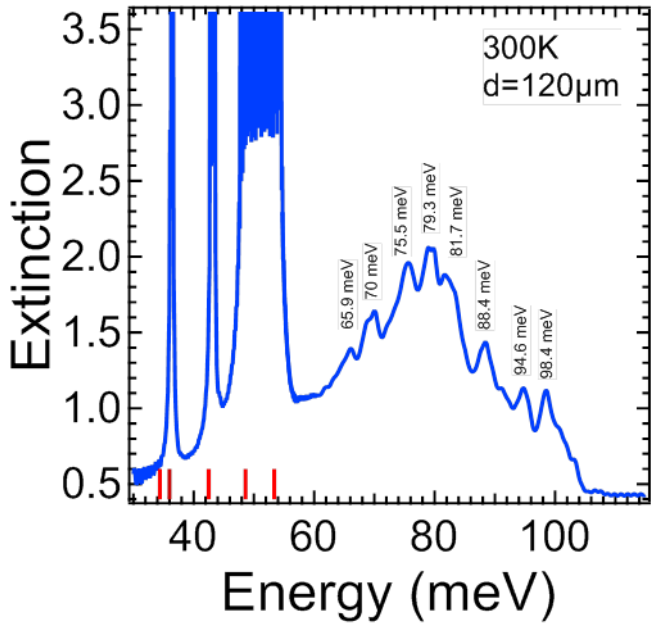


Figure 3.7: Room temperature far-IR spectra of a 120μm thick undoped pyrite crystal. Data stitched from far-IR and Mid-IR measurements. Red lines indicate IR phonon modes from [42]. Noise at the peak of the ~50 meV feature is an artifact due to total absorption.

direct band gap semiconductor, a small density of states tail at the band edge could easily explain this as well as the discrepancy between band gaps determined optically and those derived from electronic measurements [16,43]. The additional peaks observed in Fig. 3.6a could possibly be attributed to a combination of phonon replicas of the first exciton peak (explaining their increased width), band degeneracy, spin-orbit splitting, anisotropy of mass and dielectric constant, and fine structure perturbations to the excitonic levels. Future magneto-optical studies could help to establish the origin of these sub-gap peaks.

Far-IR spectra also showed several interesting features. On the low end of the extinction spectrum in figure 3.7 we see three strong absorption peaks. These are the well-known IR phonon modes of pyrite, where here two pairs of lines are too close/strongly absorbing to

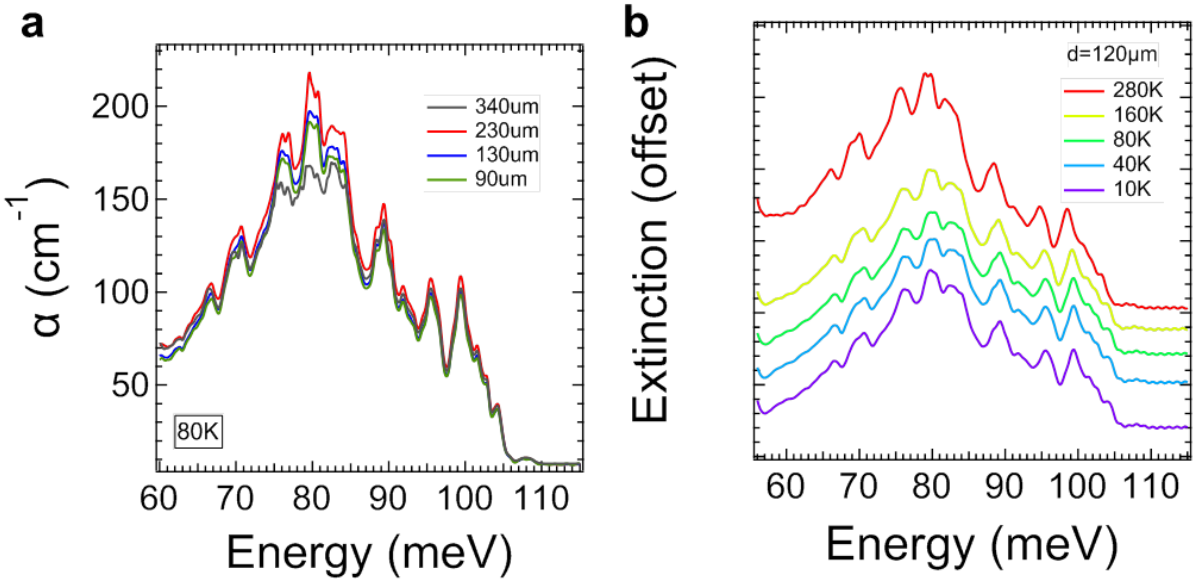


Figure 3.8: Transmission spectra of low energy features. (a) Absorption coefficient of the same crystal at 90 μm, 130 μm, 230 μm, and 340 μm showing that all but peaks near ~80 meV are independent of thickness indicating they are bulk features. (b) Extinction spectra (off set) showing the temperature dependence of the unknown far-IR features.

resolve in our instrument. The red bars indicate the IR modes from [42], showing great agreement from previous work. In the 60-110 meV range, just on the high energy side of the IR phonon lines, we see a broad absorption feature with several peaks superimposed on it. To our knowledge these features have never been reported. Figure 3.8a shows room temperature $\alpha(h\nu)$ for a crystal for several thicknesses (90 μm, 130 μm, 230 μm, and 340 μm). We can see that, with the exception of the peaks near 80 meV, the absorption is constant, indicating these features originate from the bulk of pyrite. While the peaks near 80 meV are not constant for the various thicknesses, they do not have any correlation with the thickness, making their origin unclear. The temperature dependence of these features (Fig. 3.8b) shows a ~0.7 meV blue-shift going from 280K to 160K and relatively no shift when the temperature is decreased further. Interestingly the features at ~80 meV show the same temperature dependence, which leads us to believe these peaks have the same origin as the others, further complicating the interpretation of their thickness dependence. Given

that this broad set of peaks appear to be bulk features, are present in undoped and doped samples alike, and their position with respect to the single phonon absorption lines, we tentatively attribute these features to 2 phonon processes. However, further studies would be necessary to definitively make this assignment.

### 3.1.4 Magnetization

Variable temperature dc magnetization measurements in a SQUID magnetometer were used to determine the magnetic susceptibility of the undoped crystals from 2-300 K. We find linear and reversible magnetization-field (M-H) plots at temperatures above 2 K, while M(H) is slightly nonlinear at 2 K (Figure 3.9a). Temperature dependent molar susceptibility plots $\chi_{mol}$ vs T show a paramagnetic (positive $\chi_{mol}$) response at all temperatures (Fig. 3.9b), with two regions of distinctively different behavior, in agreement with the findings of Burgardt and Seehra [44]. For temperatures >60 K undoped crystals exhibit a paramagnetic signal that increases slightly with increasing temperature. Since Fe in $FeS_2$ is in the low spin $d^6$ state we attribute, as others have [44–46], the paramagnetic response to a Van Vleck paramagnetic susceptibility, $\chi_{vv}$. Van Vleck paramagnetism is associated with a field induced electronic transition and can be calculated by the expression

$$\chi_{vv} = 2N\mu_B^2 \sum_k \frac{|\langle l|L_z|k\rangle|^2}{E_k - E_l}, \tag{3.2}$$

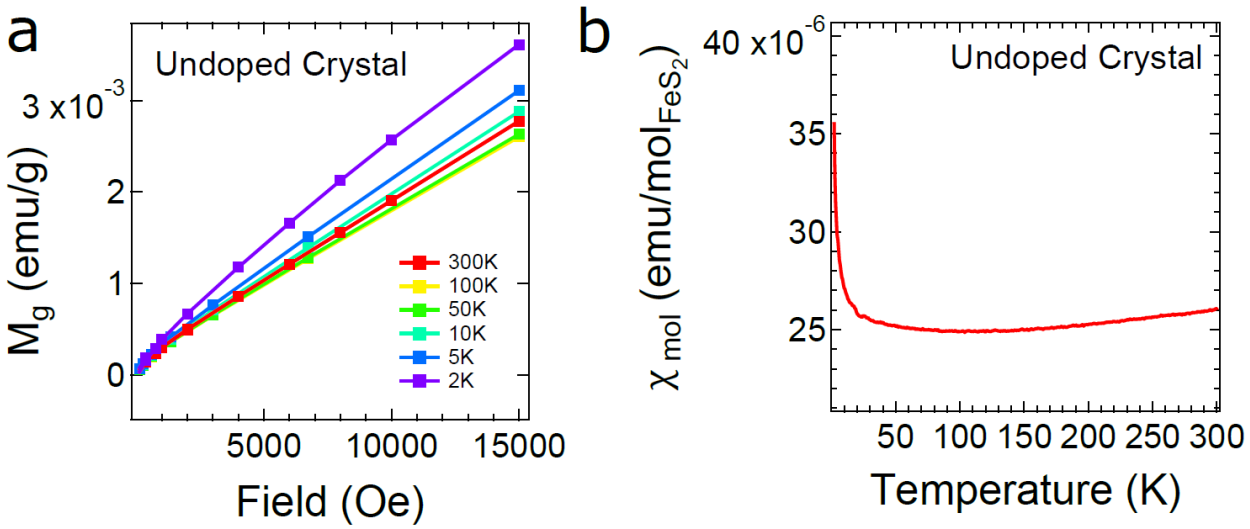


Figure 3.9. Magnetic properties of undoped pyrite crystals. (a) Mass magnetization ($M_g$) versus applied magnetic field at various temperatures for a representative nominally-undoped pyrite crystal. (b) Molar susceptibility (on an $FeS_2$ basis) as a function of temperature.

where N is Avogadro's number, $\mu_B$ is the Bohr magneton, $L_z$ is the component of the angular momentum that couples the ground state $|l\rangle$ with the excited state $|k\rangle$, having energies $E_l$ and $E_k$, respectively. For pyrite, the ground state is the $T_{2g}$ valence band and the excited state consists of the $E_g$ conduction band states, making $E_k - E_l$ the fundamental gap. Although the expression for $\chi_{vv}$ is not explicitly temperature dependent, it's inversely proportional to the band gap, which is known to have a negative temperature coefficient [16,40,47], and gives rise to the temperature dependence seen in our susceptibility measurements [45]. Indeed, we see a 4.9% change in our susceptibility as we decrease our temperature from 300 K to 100 K, in relatively close agreement with the 6.5% change seen in the optical band gap over that temperature range [16]. For temperatures below 60K our pyrite crystals exhibit Curie type behavior. Interestingly, the paramagnetic susceptibility grew substantially when crystals were crushed into powder in inert atmosphere, and strengthened further when the powders were exposed to air for hours to weeks. We find that powdered, air-exposed crystals have a large

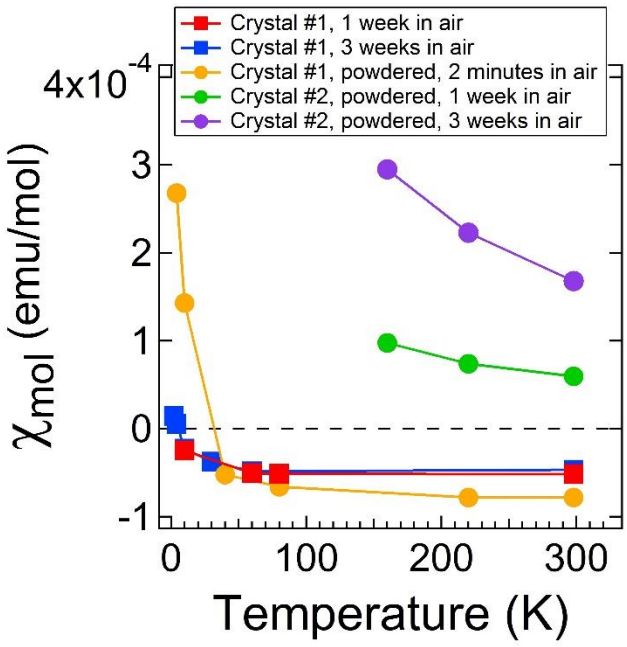


Figure 3.10. Molar susceptibility as a function of temperature for undoped crystals. Since powdered samples are difficult to mount by the method mentioned in sec. 2.5.3, samples here were loaded into plastic capsules that were lodged into plastic straws for measurement. The susceptibility of intact crystals were dominated by the diamagnetic response of the plastic capsules until very low temperature and show little change with air exposure (red and blue traces). Paramagnetic response increases substantially for crystals crushed into powder, even with minimal air exposure (orange). After sitting in air for one week, powder become paramagnetic even at room temperature, and the paramagnetism strengthens with additional time in air (green and blue). Susceptibility reported on an $FeS_2$ basis.

paramagnetic Curie-type signal even at room temperature (Figure 3.10). Given these observations, the Curie type behavior below 60K can be attributed to paramagnetic species on the crystal surface (e.g., surface $Fe^{3+}$) and the several ppm of bulk magnetic impurities present in our crystals.

# Chapter 4

# Doped Pyrite Single Crystals

While the surface inversion layer continues to be a leading issue in realizing pyrite as a solar absorbing layer in photovoltaic devices, the poorly understood and poorly controlled doping of pyrite both prevents rational device engineering [16–18,24,25] and hinders the progression of the fundamental understanding of pyrite. The impact of important fundamental studies of pyrite and its surface are often diminished due to the use of natural crystals or low purity precursors, without first considering the concentration and effect of impurities on the properties of pyrite. Given the high quality and purity, our flux-grown crystals provide a suitable experimental platform for doping studies. Below, we report on the properties of flux-grown $Co_xFe_{1-x}S_2$, $Ni_xFe_{1-x}S_2$, and $Cr_xFe_{1-x}S_2$ crystals in the dilute doping limit ($x < 0.01$, equivalent to < 3300 ppm at.), with the goals of establishing the basic doping behavior of Co, Ni, and Cr and improving our understanding of the bulk defect chemistry of pyrite in order to engineer high-performance pyrite devices.

$Co_xFe_{1-x}S_2$ and $Ni_xFe_{1-x}S_2$ alloys have been studied for many years due to their interesting electrical and magnetic properties and relevance to spintronics. $CoS_2$ and $NiS_2$ are members of the pyrite family of metal disulfides ($MS_2$, with M = Mn-Zn). While $FeS_2$ is a nonmagnetic

semiconductor, $CoS_2$ is a ferromagnetic metal ($T_C \approx 121$ K) and $NiS_2$ is a small band gap antiferromagnetic semiconductor ($E_g \approx 0.27$ eV, $T_N \approx 50$ K) that becomes weakly ferromagnetic below ~30 K [48–50]. $Co_xFe_{1-x}S_2$ is a model system for highly spin-polarized ferromagnetism [51].

Several groups have reported on the behavior of dilute Co and Ni (< 500 ppm) in natural or CVT-grown iron pyrite crystals. In important early work, Chandler and Bené concluded from low-temperature EPR data of single crystals grown by vapor transport with $Cl_2$ that cobalt on an iron site ($Co_{Fe}$) is a very shallow donor and nickel on an iron site ($Ni_{Fe}$) is a very deep donor near the middle of the band gap [52]. EPR spectra of $Co_xFe_{1-x}S_2$ crystals acquired at 2-4 K (in an effort to freeze out the itinerant cobalt electrons) showed the presence of low-spin $Co^{2+}$ ($^2E_g$ ground state), the onset of semi-metallic behavior at $x \approx 0.0001$ ([Co] = 30 ppm), and metallic conduction for $x \geq 0.005$ (1600 ppm). Spectra of $Ni_xFe_{1-x}S_2$ crystals at 77 K showed the presence of $Ni^{2+}$ ($^3A_{2g}$ ground state) with fully localized $e_g$ electrons. These authors noted some delocalization of the Ni $e_g$ electrons in a narrow defect band at higher Ni concentrations (650-10,000 ppm). In several papers investigating $Ni_xFe_{1-x}S_2$ alloys made by $ICl_3$ transport, Ho *et al*. argued that $Ni_{Fe}$ is actually a fairly good donor in pyrite, contrary to the EPR results [53,54]. Savage *et al*. studied natural single crystals using room-temperature Hall effect and conductivity measurements and concluded that Co impurities increase the free electron concentration but Ni impurities do not [55], confirming previous conclusions by Lehner *et al*. on polycrystalline samples grown by CVT from low-purity (99-99.9%) starting materials [56]. Earlier transport measurements had indicated degenerate *n*-type conduction in Co-doped CVT crystals [57,58] and thin films [59]. More recently, very detailed magnetization and transport studies by Guo *et*

*al*. showed that $Co_xFe_{1-x}S_2$ crystals grown by $I_2$ transport are metallic for $x$ at least as small as 0.0003 ([Co] ≈ 100 ppm) [60,61]. These authors found that the $Co_{Fe}$ donor efficiency (the increase in carrier concentration per unit increase in Co concentration) may be close to unity at low [Co] ($x$ < 0.004, 1300 ppm) but drops rapidly with increasing [Co] to a value of ~0.1 at $x$ = 0.075 (25,000 ppm), suggesting a concentration-dependent degree of localization of the Co $e_g$ electrons. Magnetic cluster formation was reported at temperatures below 10 K in samples with low [Co] and above the Curie temperature in samples with $x \geq 0.007$ (2333 ppm).

Here, we combine variable-temperature electrical, optical, and magnetic measurements with DFT calculations to carefully study the impact of substitutional cobalt, nickel, and chromium on the properties of ultrapure pyrite crystals. These three transition elements are common impurities in natural pyrite crystals and either known (Co) or suspected (Ni and Cr) *n*-type dopants. Lehner *et al*. recently used room-temperature optical transmission spectroscopy to estimate the energies of the defect levels introduced by high concentrations of Co or Ni in pyrite single crystals grown by $FeBr_3$ transport [25]. Our study extends past work to higher-purity pyrite host crystals that enable clearer elucidation of composition-property relationships. We also focus on a range of lower impurity concentrations (<1000 ppm) that is more relevant to the electronic doping of semiconductors. By correlating electrical, optical, and magnetic data acquired as a function of impurity concentration, sample thickness, and temperature with insights from DFT models, a detailed and self-consistent picture of the defect energy levels, concentrations, and charge states can be established. Using this approach, we show that Co creates a state within the pyrite conduction band with a high donor efficiency at low doping concentrations and essentially zero magnetic moment for [Co] < 350 ppm, making it an ideal *n*-

type dopant for pyrite. We also present the first doping and transport measurements of $Cr_xFe_{1-x}S_2$ crystals. Chromium is less studied than Co and Ni because it does not crystallize in the pyrite structure, even though it is commonly found as an impurity in many iron precursors.

## 4.1 Cobalt Doped ($Co_xFe_{1-x}S_2$)

Cobalt was added to the crystal synthesis in the form of dicobalt octacarbonyl (DOC) dissolved in hexane. The solution was added to the iron in the crucible via a micropipette then heated to 200°C for 30 minutes to evaporate the hexane, with the rest of the synthesis proceeding as the undoped crystals (sec. 2.1.1). Adding the dopant in solution phase allowed us a high degree of control in the concentration of dopants added as well as helped ensure the dopant was incorporated homogeneously. DOC was chosen rather than dissolving Co in nitric acid in order to avoid unintentional nitrogen and oxygen contamination in our crystals. We made crystals with cobalt concentrations [Co] of 5-5580 ppm (atomic basis), below are the properties investigated in these intentional Co doped pyrite single crystals.

| Sample | Section* | [Co] (ppm at.) | Average [Co] (atoms/cm$^{-3}$) | *X* |
|---|---|---|---|---|
| **1** | 1a | 244 | $2.0 \times 10^{19}$ | 0.00082 |
| | 1b | 224 | | |
| | 2a | 300 | | |
| | 2b | 316 | | |
| **2** | 1a | 253 | $2.2 \times 10^{19}$ | 0.00087 |
| | 1b | 261 | | |
| | 2a | 330 | | |
| | 2b | 283 | | |
| | 3a | 309 | | |

Table 4.1: [Co] uniformity in $Co_xFe_{1-x}S_2$ crystals.* Section 1 refers to the top of the crystal and section 3 to the bottom of the crystal (a and b refer to pieces of the crystal in the same z-section, measured to check for homogeneity in the xy plane).

### 4.1.1 Elemental Characterization

ICP-MS measurements were used to quantify the concentration of Co incorporated into our crystals. In order to test the homogeneity of Co, crystals were sectioned into several slabs parallel to the top facet and each slab was fractured into two pieces before each was dissolved in acid and each measured by ICP-MS separately. By breaking up the crystal in this manner we were able to check the uniformity of Co in our samples. Table 4.1 shows the results of two such crystals, displaying no significant inhomogeneity in our samples. The small variation seen likely arose from errors in the ICP-MS measurement of solution preparation. While the cobalt was readily incorporated into the crystals using this approach, we saw insignificant changes in the concentrations of most other measured elements (see Table 4.2). The only element we see increase to over 1 ppm is Cu, which is a likely a surface contaminate from the slow speed saw used during the sectioning of this crystal before measurement.

| 333 ppm Co Sample | | | |
|---|---|---|---|
| S:Fe = 2.060193262 | | | |
| **element** | **ppm at** | **element** | **ppm at** |
| Na | 299.8575 | Te[a] | 0.1070 |
| Mg | 0.8903 | Cs | 0.0007 |
| Sc | 0.0593 | Ba | 0.0153 |
| Ti | 0.0948 | La | 0.0008 |
| V | 0.0309 | Ce | 0.0006 |
| Cr | 2.4847 | Pr[a] | 0.0067 |
| Mn | 0.0860 | Nd | 0.0364 |
| Co | 333.1991 | Sm | 0.0098 |
| Ni | 1.5212 | Eu | 0.0028 |
| Cu | 1.2066 | Gd | 0.0053 |
| Zn | 2.6183 | Tb | 0.0017 |
| Ga | <0.063 | Dy | 0.0045 |
| Ge | 0.0028 | Ho | 0.0010 |
| As | 0.0701 | Er | 0.0038 |
| Se | 0.3193 | Tm | 0.0005 |
| Rb | 0.0049 | Yb | 0.0055 |
| Sr | 0.2997 | Lu | 0.0024 |
| Y[a] | 0.0024 | Hf[a] | 0.0035 |
| Zr[a] | 0.0023 | Ta[a] | 0.0010 |
| Nb[a] | 0.0023 | W[a] | 0.0126 |
| Mo[a] | 0.0187 | Re[a] | 0.0028 |
| Ru[a] | 0.0374 | Os[a] | 0.01491 |
| Rh[a] | 0.0194 | Ir[a] | 0.00164 |
| Pd[a] | 0.0336 | Pt[a] | 0.0108 |
| Ag | 0.1948 | Au[a] | 0.0160 |
| Cd | 0.0374 | Hg[a] | 0.2932 |
| In | 0.0085 | Tl | 0.0027 |
| Sn[a] | 0.0088 | Pb | 0.0760 |
| Sb[a] | <0.03 | Bi | 0.0070 |
| | | U | 0.2648 |

Table 4.2: ICP-MS results of a typical Co-doped crystal ([Co] = 333 ppm) pyrite reported in atomic ppm.
[a] Elemental concentration determined by semi-quantitative methods.

### 4.1.2 Structural Characterization

Crystals grown with cobalt incorporated show similar size, shape, faceting, and quality as undoped crystals. High-resolution synchrotron powder XRD showed no evidence of phases other than pyrite, even for crystals with the highest cobalt concentration studied here (5580 ppm, Fig. 4.1). These observations are reasonable given that $FeS_2$ and $CoS_2$ (cattierite) form a solid solution over the entire compositional range [48,62]. Unit cell length was determined for undoped and doped crystals by Rietveld refinement of the XRD patterns. We observed shifts in XRD peak positions that are consistent with lattice expansion as well as an increased unit cell length due to the incorporation of cobalt, in rough agreement with Vegard's law ($a$ = 5.524 Å for $CoS_2$) [63] and the expectation that cobalt occupies iron sites in the pyrite $FeS_2$ structure to form substitutional $Co_{Fe}$ defects [61].

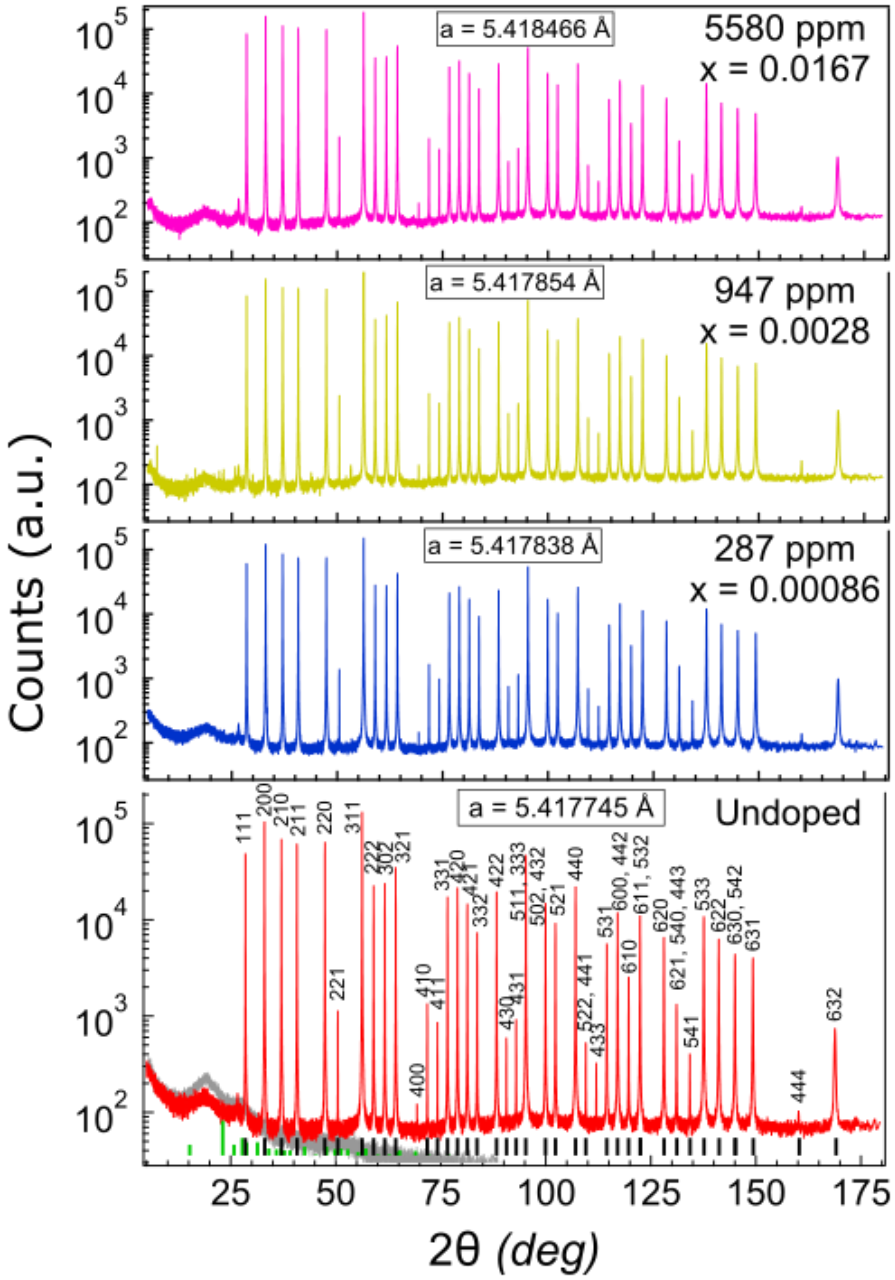


Figure 4.1. Synchrotron XRD pattern of a powdered undoped and powdered $Co_xFe_{1-x}S_2$ crystals with $x$ = 0.00086, 0.0028, and 0.0167, presented on a log scale. All 39 reflections index to pyrite and no other phases are detected. Lattice parameters were calculated by Rietveld refinement with PDXL2 software at room temperature. The background pattern is for an empty capillary tube. Overlaid on the undoped data are a background pattern of an empty capillary tube (gray) as well as reference patterns for pyrite (black bars) and orthorhombic sulfur (green bars).

### 4.1.3 Hall Effect Studies

Variable-temperature electrical conductivity and Hall coefficient data (Figure 4) show that cobalt induces metallic behavior in pyrite, in agreement with previous reports on the electrical properties of $Co_xFe_{1-x}S_2$ crystals [25,52,60]. The free electron density and conductivity both increase, while the electron mobility decreases, with increasing cobalt concentration (Fig. 4.2a-c). At Co concentrations as low as 5ppm ($3.7\times10^{17}$ $cm^{-3}$) we observe decreasing conductivity with increasing temperature and a mobility temperature dependence proportional to $T^{\alpha}$, with $\alpha \approx -1.7 \pm 0.2$. This is close to the $T^{-3/2}$ expected for the thermally activated phonon scattering that is typical of conduction in metals. This behavior, along with a temperature independent carrier concentration, indicates metallic conduction in even our most lightly doped samples. Along with our magnetic measurements presented below, we could conclude that Co creates a defect state, $E_D$, resonant with the conduction band states of pyrite, i.e. that $E_D$ lies above the conduction band minimum (CBM), $E_C$, such that $(E_D-E_C) > 0$. However, we find that only ~60% of cobalt incorporated results in additional free carriers for low doping concentrations (3-100ppm) and that this value further decreases when additional Co is added to the system, down to ~28% for our largest Co concentration measured (1812ppm). From this, there appears to be a concentration dependent compensating defect state created with Co incorporation. The larger decrease in additional free carriers for greater doping concentrations could also be explained by the reduction in ionization efficiency for increasingly doped degenerate semiconductors [64,65].

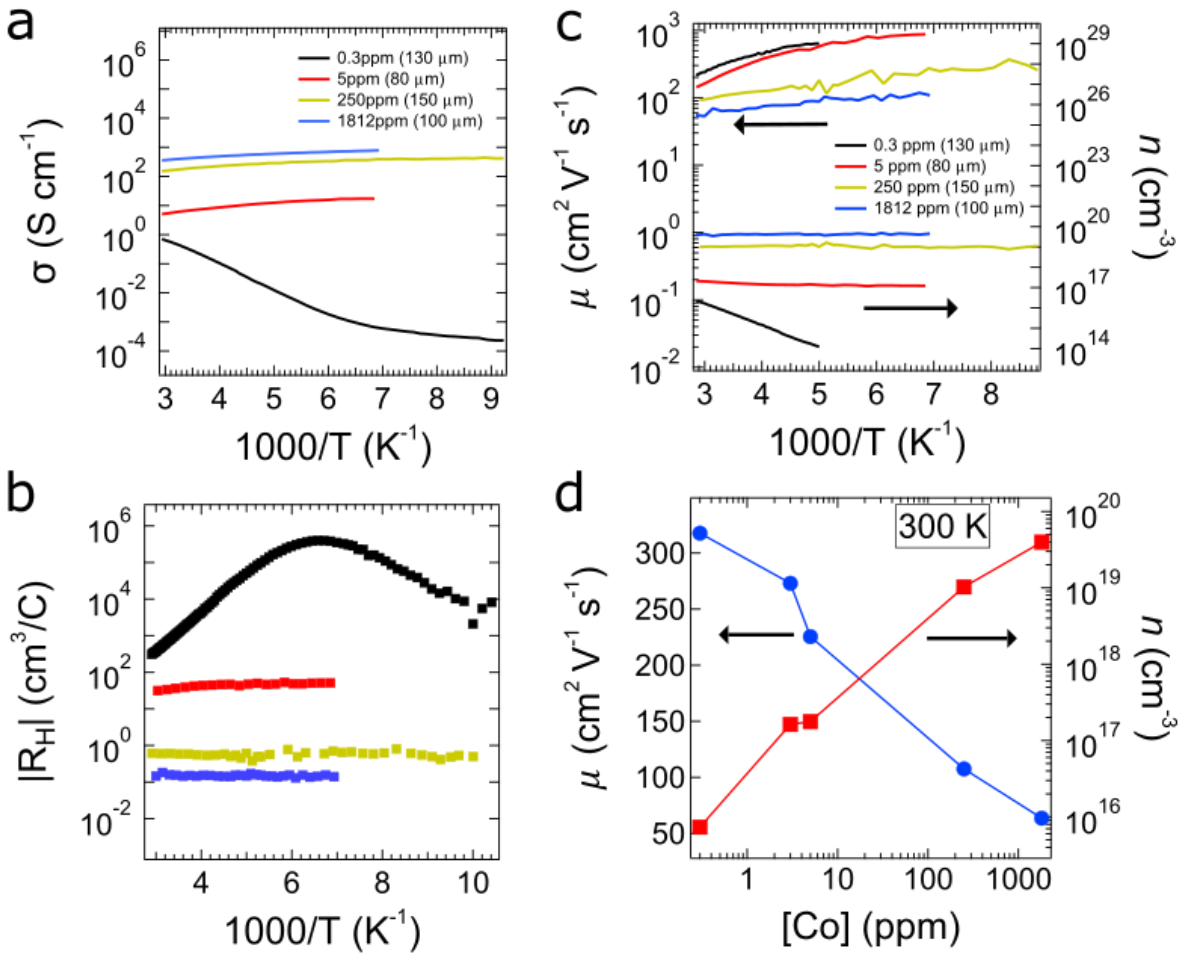


Figure 4.2. Electrical properties of $Co_xFe_{1-x}S_2$ crystals. (a) Conductivity and (b) absolute Hall coefficient versus inverse temperature for samples with various Co concentrations, from .3 ppm (for an undoped control crystal) to 1812 ppm. (c) Bulk electron density ($n$) and mobility ($\mu$) in the unambiguously unipolar ($n$-type) temperature region. (d) Room-temperature $n$ and $\mu$ as a function of [Co].

In a semiconductor the number of ionized donors $N_D^+$ can be determined from

$$N_D^+ = \frac{N_D}{1+2\ exp[\frac{E_F - E_D}{kT}]}. \quad (4.1)$$

Where $N_D$ is the donor concentration and $E_F$ is the Fermi the energy of the system. The number of free carriers $n$ in the system can also be calculated using

$$n = N_C \frac{2}{\sqrt{\pi}} F_{\frac{1}{2}}(\frac{E_F - E_C}{kT}), \quad (4.2)$$

where $N_C$ is the effective density of states in the conduction band, under the parabolic band approximation, and $F_{1/2}$ is the Fermi integral given by

$$F_{1/2}(\eta_f) = \int_0^\infty \frac{\eta^{1/2}\, d\eta}{1+exp(\eta - \eta_f)}. \quad (4.3)$$

Equations (6) and (7) can be equated using the charge neutrality condition, $n \cong N_D^+$. From this a self-consistent Fermi energy can be determined from a given donor level ($E_D$-$E_C$) and $N_D$ then can be used to calculate $n$ or $N_D^+$. In non-degenerate semiconductors the condition that $(E_F - E_C) > 3kT$, allows one to use Boltzmann statistics to greatly simplify Eq. 4.2 to obtain an analytic solution. For the case of degenerate semiconductors, this condition is not met and Eq. 4.2 must be solved numerically. Taking this degeneracy into account we find that as $N_D$ is increased $n$ also increases (and hence $N_D^+$), until the Fermi level rises to the point where the

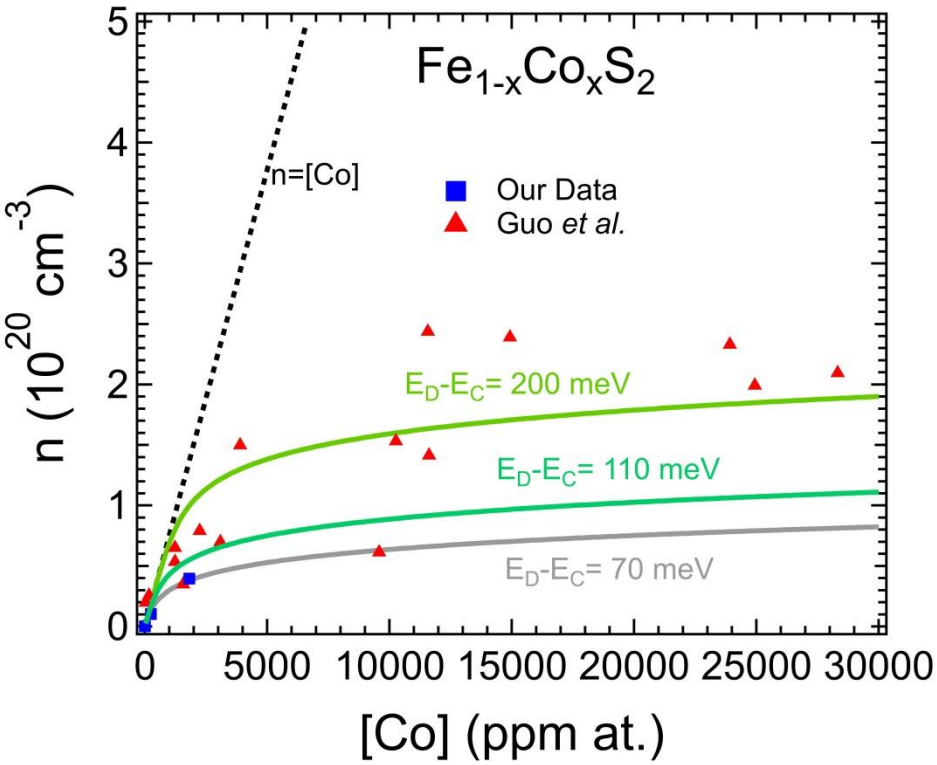


Figure 4.3. Number of charge carriers as a function of Co concentration. Blue squares represent the data shown in Fig. 4.2d, while the red triangles are adapted from [60]. The dashed line shows $n$ if every Co atom contributes one electron. The solid lines are fits to the joint data where $E_c - E_d$ is allowed to float. The upper line is a fit of the entire joint data set resulting in a defect state ~200 meV above $E_C$, while the middle line is a fit to [Co] < 4000 ppm giving us $E_D$-$E_C$ = 120 meV. The bottom solid line is a fit to only our data resulting in $E_D - E_C$ = 70 meV.

probability of occupying the defect state is non-negligible, making $\frac{N_D^+}{N_D} < 1$. However, since we look only at dilute doping cases in our study, this effect is not prominent in our data set with only our largest doping concentration showing a drastic decrease in ionization efficiency. Guo *et al.* showed that while $n$ increased with increasing [Co] for concentrations below 8000ppm, $n$ was relatively constant for [Co] > 8000ppm [60]. This behavior is well captured when taking into account the effects of degeneracy on ionization efficiency. Least square fits of our joint data sets (using only Guo *et al.*'s low [Co] (< 4000 ppm) data) place the defect state ~110meV above $E_C$ (see Fig. 4.3). However, it must be noted that the validity of [Co] in the low [Co] range of Guo

et.al.'s data is called into question since the concentration was calculated from the magnetization saturation [61]. As we'll see below (sec. 4.1.5) in the low [Co] range, a large majority of the Co present is in the low-spin $Co^{3+}$ resulting in no magnetic moment. This implies that the concentration of [Co] in [60] is overestimated in the low [Co] regime. Correcting for this would push the $E_D$ from fits closer to $E_C$. Fits to only our data place the defect state ~70 meV above the conduction band minimum. While this model is oversimplified, in that it assumes the donor density of states is a delta function at $E_D$ and neglects changes to the shape of the conduction band with increased doping, it gives us a qualitative means of understanding the reduction in donor efficiency and helps give us an approximate location of our defect state within our conduction band (70 – 110 meV above $E_C$).

### 4.1.4 Optical Absorption

In addition to increasing the electrical conductivity, Co also significantly increases optical absorptivity within the band gap of pyrite. We observe two prominent new room-temperature absorption bands centered at ~0.615 eV and <0.2 eV that grew in intensity with increasing [Co] (Figure 4.4). Lehner *et al*. reported similar spectra for $Co_xFe_{1-x}S_2$ crystals containing a greater concentration of Co (as well as a number of other impurities) [25]. We find that the peak at 0.615 eV shifts to higher energy with decreasing temperature, following the general temperature dependence of the pyrite band gap, while the lower-energy feature is independent of temperature (Fig. 4.4c). Both features can be assigned to bulk rather than surface defects since the absorption coefficient for these peaks are independent of thickness (data not shown). The origin of the two absorption features is discussed below. We note that

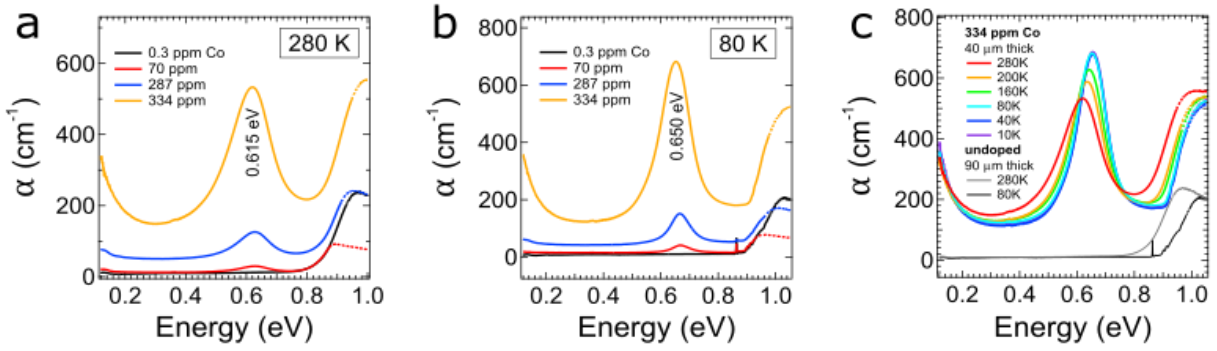


Figure 4.4. Optical absorptivity spectra of $Co_xFe_{1-x}S_2$ crystals. FTIR absorptivity spectra of polished crystals with various cobalt concentrations at (a) 80 K and (b) 280 K. Spectra of an undoped crystal ([Co] ≈ 0.3 ppm) are included for reference (black curves). The thickness of each sample is indicated in the legends. (c) Spectra for the sample with [Co] = 334 ppm at several temperatures, overlaid with 80 K and 280 K spectra from an undoped crystal for comparison.

the baseline absorptivity within the band gap rises steadily with added Co, suggestive of free carrier absorption. Indeed, samples with [Co] > 1000 ppm were too opaque throughout the sub-band gap region for measurement with our system, as would be expected for samples with a large free carrier density. In addition, the series of peaks at 0.85-0.93 eV present in low-temperature spectra of undoped crystals is progressively suppressed in samples with higher [Co] (Fig. 4.4ba). This latter finding indicates that $Co_{Fe}$ centers disrupt whatever states are responsible for these near band edge transitions (similar to the action of Cr in $Cr_xFe_{1-x}S_2$ samples, see sec. 4.3.4).

### 4.1.5 Magnetization

We used magnetization measurements to assess the spin state of Co in the $Co_xFe_{1-x}S_2$ crystals. Surprisingly, we find that the Co-doped crystals have vary similar magnetic behavior as undoped crystals for low [Co] (Figure 4.5b). They exhibit Van Vleck paramagnetism at high

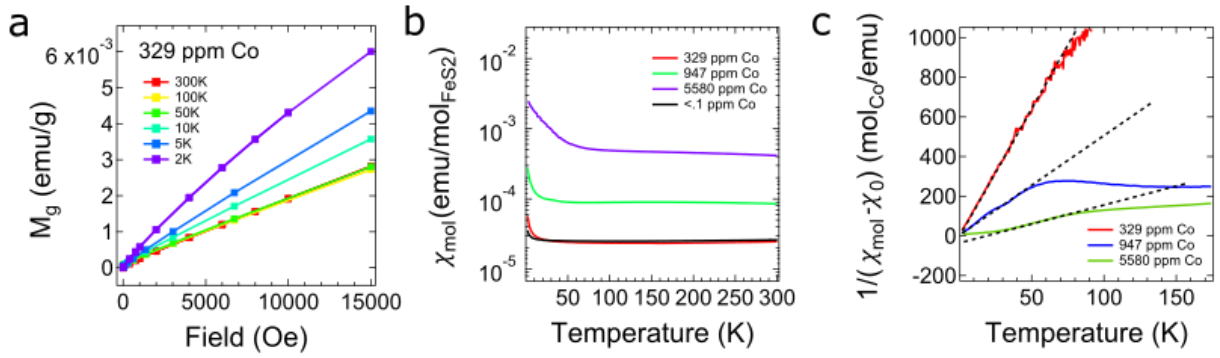


Figure 4.5. Magnetic properties of $Co_xFe_{1-x}S_2$ crystals. (a) Mass magnetization ($M_g$) versus applied magnetic field at several temperatures for a crystal with [Co] = 329 ppm, showing a linear response at high temperatures and becoming non-linear near 2K. (b) Molar susceptibility (on a $FeS_2$ basis) as a function of temperature. Data for an undoped crystal are also shown. (c) Inverse molar susceptibility (on a Co basis) after subtracting out a roughly constant $\chi_0$ component (Van Vleck or Pauli paramagnetism for low [Co] and high [Co] respectively).

temperatures, only transitioning to Curie type behavior at low temperatures (< 100 K for the 329 ppm sample). As we increase the concentration of Co we see both an increase in the Curie-type behavior at low temperatures and the constant offset at higher temperatures. We attribute, as Guo et.al. did [61], the high temperature susceptibility behavior to the Pauli susceptibility originating from the large number of iterant electrons donated by Co.

Fitting our lowest [Co] data (329 ppm) to Eq. (2.4) in the region dominated by Curie-type behavior, we find a Curie constant of $C_m$ = 0.08 emu K/$mol_{Co}$, giving an effective magnetic moment $\mu_{eff} = 2.82(C_m)^{1/2}$ = 0.8 Bohr magnitons $\mu_B$ per Co atom and a Curie-Weiss temperature $\theta$ is essentially zero, which is characteristic of systems containing dilute, non-interacting paramagnetic centers (Fig. 4.5c). Such a small $\mu_{eff}$ suggests that at these low concentrations cobalt exists in the pyrite lattice as isolated octahedral $Co^{3+}$ centers with a low-spin $t_{2g}^6$ configuration, giving zero effective magnetic moment per ion. This is consistent with the

observation that cobalt's defect state lies within the pyrite conduction band, since electron donation by $Co^{2+}$ to the crystal should result in diamagnetic $Co^{3+}$ as the dominant cobalt species. The absence of electron capture by $Co^{3+}$ to form paramagnetic $Co^{2+}$ centers at lower temperatures is further evidence that the $Co_{Fe}$ states may be resonant with the pyrite conduction band. If we assume that the defect state $E_D$ lies 70 meV above the conduction band, the calculated fraction of un-ionized cobalt atoms in our 329 ppm sample (i.e. the number of Cobalt in the 2+ state) is 0.33. This is in close agreement with the 0.28 unpaired electrons per Co derived from the spin-only effective magnetic moment equation.

By fitting the higher [Co] samples as we did the lower [Co], this time $\chi_0$ accounting for the relatively temperature independent Pauli susceptibility, we can determine $\mu_{eff}$ for these samples as well. From these fits we find $\mu_{eff}$ = 1.2 $\mu_B$ and 2.1 $\mu_B$, giving 0.84 and 1.30 unpaired electrons per Co for 947 ppm and 5580 ppm respectivetly. If we calculate the fraction of un-ionized Co within our system for these samples, again assuming $E_D$ - $E_C$ = 70 meV, we obtain values of 0.59 and 0.87 for the 947 ppm and 5580 ppm samples respectively. This is in excellent agreement with derived values for the 947 ppm sample, giving validity to the results to our fits of $n$ vs [Co] in sec. 4.1.3. The discrepancy seen in the 5580 ppm sample isn't surprising as we also see a Curie-Weiss temperature of 17.8 K, indicating the presence of ferromagnetic ordering.

Table 4.3 shows that better agreement between experimentally derived $Co^{2+}$ concentrations and those theoretically calculated assuming $E_D$-$E_C$ = 70 meV than those calculated assuming the 110 meV from fits of Guo et.al.'s and our joint data, indicating that the Co defect state lies closer to 70 meV above $E_c$ than 110 meV.

| [Co] (ppm) | $\mu_{eff}$ ($\mu_B$) | Θ (K) | n | Fraction un-ionized (Theory) | |
|---|---|---|---|---|---|
| | | | | $E_D$-$E_c$=110 meV | $E_D$-$E_c$=70 meV |
| 329 | .802 | -0.31 | .282 | 0.141 | .333 |
| 947 | 1.24 | -0.76 | .593 | 0.413 | .590 |
| 5580 | 2.07 | 17.8 | 1.30 | 0.817 | .870 |

Table 4.3: Results of Curie-Weiss fits of $Co_xFe_{1-x}S_2$ crystals were $\mu_{eff}$ is the effective magnetic moment, Θ is the Curie-Weiss temperature and n is the number of unpaired electrons.

### 4.1.6 Summary

We turned to DFT calculations to help rationalize the measured electrical, optical, and magnetic properties of the $Co_xFe_{1-x}S_2$ crystals. The modeling utilized a 3×3×3 pyrite $FeS_2$ supercell containing a single $Co_{Fe}$ point defect, which is equivalent to a $Co_{Fe}$ concentration of 3086 ppm ($2.3 \times 10^{20}$ atoms/$cm^3$).

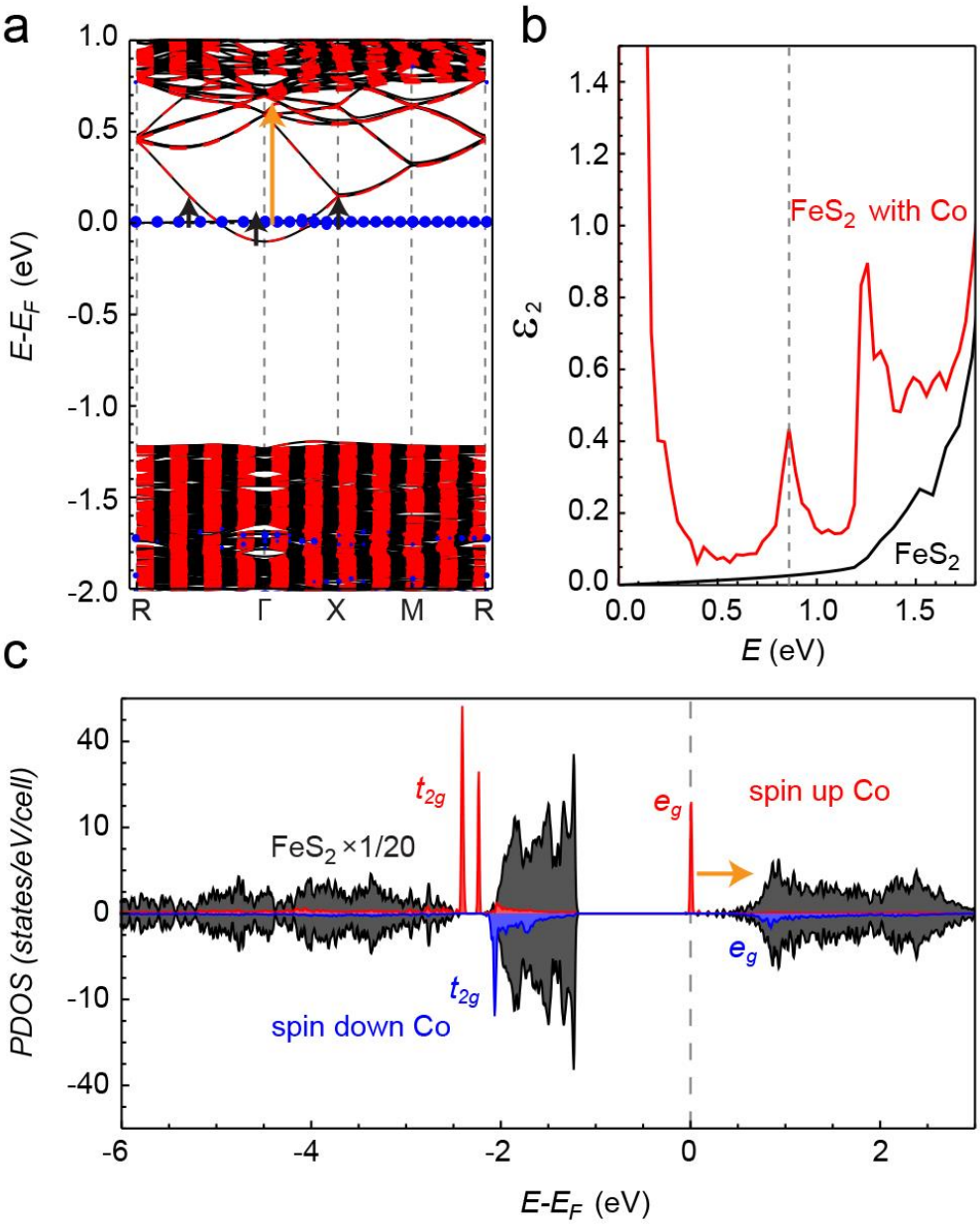


Figure 4.6. DFT results for $Co_xFe_{1-x}S_2$. Calculated (a) band structure, (b) imaginary part of the dielectric function ($\varepsilon_2$), and (c) spin-resolved projected density of states for $Co_xFe_{1-x}S_2$ with $x$ = 0.0091. The HOMO of $Co^{2+}$ is predicted to lie within the pyrite conduction band. Transitions from these Co *d*-orbitals to higher conduction bands (yellow arrow in (a) and (c)) account for the pronounced peak in the sub-gap absorption spectrum (dashed line in (b)) observed for $Co_xFe_{1-x}S_2$ crystals.

The calculated band structure, imaginary part of the dielectric function ($\varepsilon_2$), and spin-resolved partial density of states for $Co_xFe_{1-x}S_2$ are presented in Figure 7. The calculations suggest that the partially-occupied $e_g^*$ states of $Co_{Fe}$ lie within the pyrite conduction band, ~110 meV above the conduction band minimum, making Co a donor with zero ionization energy (an auto-ionizing donor), which is in good agreement with the experimental data (Fig. 4.6a). The $\varepsilon_2$ spectrum shows two peaks within the band gap at energies similar to the features at <0.2 eV and ~0.615 eV observed experimentally (Fig. 4.6b and Fig. 4.4). Analysis of the optical transition matrix elements indicates that the low-energy absorption results from transitions to and from the Co defect state and the nearby conduction band states (black arrows in Fig. 4.6a) , while transitions from cobalt's $e_g^*$ states to higher conduction bands of pyrite (yellow arrow in Fig. (7a)) are responsible for the higher-energy peak denoted with a dotted line in Fig. 4.6c. The highest energy peak determined from these calculations is absent in our experimental measurements. This peak originates from transitions from the valence band to the d-orbital state of the Co dopant and is likely outside of the spectral window experimentally measured. The absorption spectrum obtained from DFT calculations agrees qualitatively with the experimental results (Fig. 4.4). The calculated number of unpaired electrons per $Co_{Fe}$ is ~0.7, indicating a mixed oxidation state of Co ($Co^{2+}$ and $Co^{3+}$). If we consider degeneracy effects as we did previously, a sample with a donor concentration of 3086ppm and a donor energy ~110 meV above $E_C$ (as is the case in the DFT model), only 28% of the donor states are ionized leaving 72% of the donors with an unpaired electron, in agreement with the value calculated from DTF.

Bringing together the optical, electrical, magnetic and DFT results we can conclude that Co states lie just above the conduction band edge, resulting in essentially no magnetic moment for

low [Co]. This means very low doping concentrations are needed to have a large effect on the electrical properties of pyrite. This gives doping with Co a big advantage over other intentional n-type dopants, as we would be able to easily modify the Fermi level without introducing a large number of scattering sites that would ultimately reduce the mobility resulting in poorer device performance. If the issue of unintentional n-type doping of pyrite could be solved, Co would be a great candidate for controllable n-type doping.

## 4.2 Nickel Doped ($Ni_xFe_{1-x}S_2$)

Nickel-containing pyrite crystals were made using 99.996% nickel powder dissolved in hydrazine as the nickel source and incorporated into the synthesis in the same manner that the Co precursor was added to the Co-doped samples. Using this method, samples with [Ni] ranging from 8 to 17,942 ppm were fabricated and the structural, electronic, optical, and magnetic properties were thoroughly characterized to give us a clear understanding of the effects of Ni doping.

### 4.2.1 Elemental Characterization

We use ICP-MS to quantify the concentration of Ni in our doped samples as well as the 60 other elements measured by ICP-MS. Results indicate a Ni content of 8 to 17,942 ppm our Ni-doped crystals, increasing roughly in proportion to the amount of nickel spiked in the flux. Three crystals were sectioned into slab parallel to the top facet and some of those slabs were

| Sample | Ni:Fe Added | Section* | [Ni] (ppm at.) | Average [**Ni**] (atoms/cm$^{-3}$) | ***x*** |
|---|---|---|---|---|---|
| **1** | .00047 | 1 | 29 | $1.9 \times 10^{18}$ | $8 \times 10^{-5}$ |
| | | 2a | 28 | | |
| | | 2b | 24 | | |
| **2** | .00095 | 1 | 323 | $3.7 \times 10^{19}$ | 0.0016 |
| | | 2a | 623 | | |
| | | 2b | 535 | | |
| | | 3 | 588 | | |
| **3** | .0019 | 1 | 1187 | $7.8 \times 10^{19}$ | 0.0033 |
| | | 2 | 989 | | |

Table 4.4. [Ni] uniformity in $Ni_xFe_{1-x}S_2$ crystals.* Section 1 refers to the top of the crystal and section 3 to the bottom of the crystal (a and b refer to pieces of the crystal in the same z-section, measured to check for homogeneity in the xy plane).

fractured in half before each was dissolved in acid and measure by ICP-MS to check for Ni inhomogeneity in our samples. We found that two of the crystals were evenly doped throughout the crystal while one sample have a two-fold lower [Ni] in its topmost section (Table 4.4). The reason for such a drastic gradient in that sample is not yet understood, but the consistency in the other measurements give us reason to believe that a majority of the samples are uniformly doped and we will treat them as such for the duration of this section. However, we attempted to measure [Ni] on the exact sample used in the other characterization techniques whenever possible. Full elemental analysis of a 558 ppm Ni sample shows us that the addition of Ni into our sample didn't unintentionally add other impurities to our crystals (Table 4.5).

| 558 ppm Ni Sample | | | |
|---|---|---|---|
| S:Fe = 1.8144[b] | | | |
| **element** | **ppm at** | **element** | **ppm at** |
| Na | 19.9891 | Te[a] | 0.0017 |
| Mg | 2.1924 | Cs | 0.0014 |
| Sc | 0.0696 | Ba | <0.05 |
| Ti | 0.20799 | La | 0.0003 |
| V | 0.0212 | Ce | 0.0006 |
| Cr | 2.8758 | Pr[a] | <0.001 |
| Mn | 0.3184 | Nd | <0.003 |
| Co | 0.1147 | Sm | 0.0001 |
| Ni | 558.6 | Eu | <0.0001 |
| Cu | <3.28 | Gd | <0.0004 |
| Zn | 4.6496 | Tb | 0.0010 |
| Ga | 0.0033 | Dy | <0.0001 |
| Ge | 0.0048 | Ho | <0.0002 |
| As | <0.11 | Er | <0.0001 |
| Se | <0.01 | Tm | <0.0001 |
| Rb | 0.0205 | Yb | <0.0002 |
| Sr | 0.0151 | Lu | 0.0014 |
| Y[a] | 0.0005 | Hf[a] | <0.0001 |
| Zr[a] | <0.04 | Ta[a] | <0.0001 |
| Nb[a] | 0.0001 | W[a] | 0.0003 |
| Mo[a] | <0.017 | Re[a] | 0.0026 |
| Ru[a] | 0.1203 | Os[a] | 0.00044 |
| Rh[a] | 0.0104 | Ir[a] | 0.00026 |
| Pd[a] | 0.0051 | Pt[a] | 0.0030 |
| Ag | 0.0005 | Au[a] | 0.0001 |
| Cd | 0.0007 | Hg[a] | 0.0818 |
| In | 0.0041 | Tl | 0.0001 |
| Sn[a] | 0.0002 | Pb | <0.04 |
| Sb[a] | 0.0002 | Bi | 0.0029 |
| | | U | 0.0065 |

Table 4.5: ICP-MS results of a typical Ni-doped ([Ni] = 558 ppm) crystal reported in atomic ppm. [a] Elemental concentration determined by semi-quantitative methods. [b] Due to sulfur loss during sample preparation, the measured S:Fe deviates from the expected 2:1.

### 4.2.2 Structural Characterization

As with the Co-doped crystals, the Ni-containing crystals had similar size, shape, faceting, and overall quality as our undoped crystals. Synchrotron XRD patterns suggest that crystals with relatively low Ni content (<1500 ppm, $x < 0.0045$) are phase pure and homogeneous. While we see several peaks in the 517 ppm XRD pattern (red asterisks in Fig. 4.7a) that don't belong to pyrite, they index to cristobalite ($SiO_2$) and are likely a surface contaminate from sample preparation rather than a phase impurity in the bulk of our crystal. Higher Ni levels result in increasingly broadened, asymmetric line shapes consistent with a highly inhomogeneous distribution of Ni that induces a range of lattice constants in individual crystals (Figure 4.7a). Since $NiS_2$ (vaesite, $a$ = 5.670 Å) and $FeS_2$ ($a$ = 5.417 Å) are reported to form partial $Ni_xFe_{1-x}S_2$ solid solutions with a maximum $NiS_2$ solubility in pyrite of only $x$ = 0.073 at 729°C and probably much lower equilibrium solubility close to room temperature (likely <1000 ppm) [66,67], high Ni loadings are anticipated to cause compositional heterogeneity, metastable solid solutions, and phase separation. In addition to asymmetric peak broadening toward larger $d$-spacing, we sometimes observed minor phase impurities in crystals with higher Ni content (Fig. 4.7). To avoid complications originating from non-uniform composition, we focus most of our attention on crystals with [Ni] < 1500 ppm.

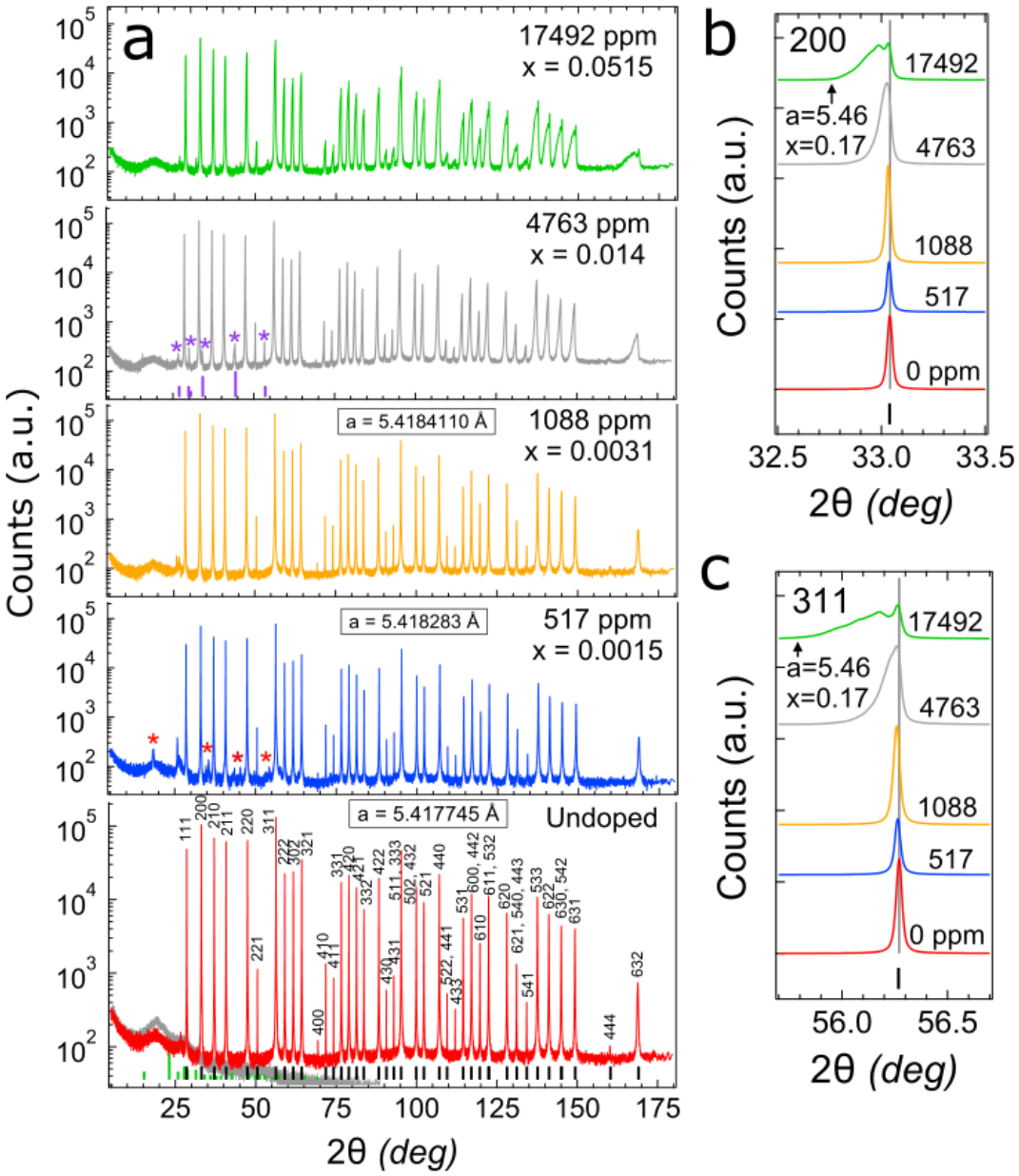


Figure 4.7. Synchrotron powder XRD patterns of $Ni_xFe_{1-x}S_2$ crystals. (a) Data on a log scale for $Ni_xFe_{1-x}S_2$ samples with $x$ = 0.0, 0.0016, 0.0033, 0.014, and 0.0525. Purple asterisks denote an impurity phase in the $x$ = 0.014 sample. The impurity peaks are consistent with "$Fe_8Ni_8S_{16}$" (PDF 00-022-0627, purple bars) or $FeNiS_2$ (PDF 01-071-4458). Red asterisks mark peaks that belong to $SiO_2$ (PDF 00-003-0257), likely a contaminate from sample prep. Overlaid on the undoped data are a background pattern of an empty capillary tube (gray) as well as reference patterns for pyrite (black bars) and orthorhombic sulfur (green bars). (b,c) Magnified views of the 200 and 311 reflections, showing significant broadening and distortion of the peaks toward smaller $2\Theta$ (larger $d$-spacing) for $x$ > 0.0033. The broad, asymmetric reflections indicate that the two samples with the highest [Ni] are not single-phase $Ni_xFe_{1-x}S_2$ solid solutions.

### 4.2.3 Hall Effect Studies

Conductivity and Hall data for Ni-containing crystals show that Ni impurities have little impact on the electrical properties of pyrite (Figure 4.8). Near room temperature, where the undoped control crystals and all of the Ni-containing crystals are unambiguously *n*-type due to ionization of bulk donors, we find that $\sigma(T)$ is independent of [Ni] for [Ni] < 1000 ppm and actually *decreases* for higher [Ni] because of a reduced carrier mobility. The electron concentration shows some spread ($10^{15}$-$10^{16}$ $cm^{-3}$ at 300 K) but is clearly uncorrelated with [Ni]. We also note a large increase in the activation energy of $\sigma(T)$ for samples with [Ni] > 1000 ppm. From section 4.2.2, we know that samples with this high of a Ni concentration show phase impurities and large crystal strain. It appears, for these samples conduction is dominated by these impurities which greatly alter electronic behavior. However, because of the poor properties of these crystals they are of limited interest to us and were not explored further. From these data, we conclude that $Ni_{Fe}$ is either a very deep donor (at least 400 meV below the conduction band edge) or completely compensated by accompanying acceptor defects. Either way, Ni is not a significant dopant in pyrite. Our assessment agrees with the EPR results of Chandler and Bené on CVT-grown $Ni_xFe_{1-x}S_2$ crystals made using $Cl_2$ transport (with $x$ estimated from nuclear activation analysis to be $0.0004 \leq x \leq 0.03$) [52] as well as the Hall measurements of Lehner and co-workers on CVT crystals made with $FeBr_3$ as the transport agent ($0.005 \leq x \leq 0.01$ by secondary ion mass spectrometry) [25,56]. However, our results disagree with the

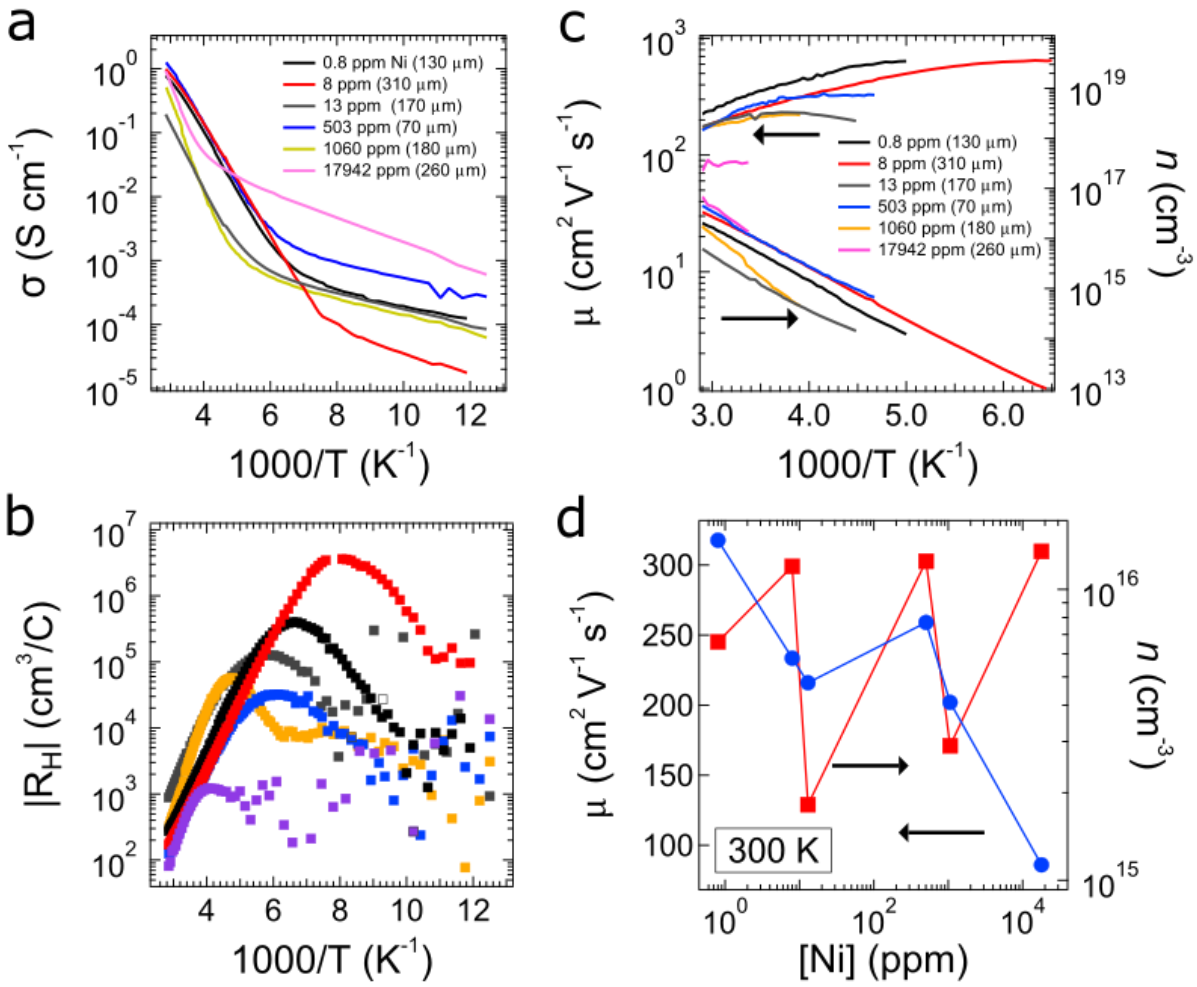


Figure 4.8. Electrical properties of $Ni_xFe_{1-x}S_2$ crystals. (a) Conductivity and (b) absolute Hall coefficient versus inverse temperature for samples with various nickel concentrations, from 0.8 ppm (for an undoped control crystal) to 17,942 ppm. (c) Bulk electron density ($n$) and mobility ($\mu$) in the unambiguously unipolar ($n$-type) temperature region. (d) Room-temperature $n$ and $\mu$ as a function of [Ni].

findings of Ho *et al.*, who reported that $\sigma(T)$ increases with [Ni] for $Ni_xFe_{1-x}S_2$ alloys (with $x$ = 0.01, 0.02, 0.04, and 0.1, although no elemental analysis was reported) made by CVT using $ICl_3$ as the transport agent [53,54]. The latter results can be understood if $ICl_3$ somehow reduces the concentration of compensating defects or results in the formation of Ni defect complexes (possibly with $I^-$ and/or $Cl^-$) that act as reasonably shallow donors in pyrite.

### 4.2.4 Optical Absorption

While Ni impurities have little impact on the electrical properties of pyrite, they do result in a measurable increase in optical absorption below the bulk band gap. With increasing [Ni], we observe progressively higher room-temperature absorptivity across a broad range of photon energies, from ~0.3 eV up to the pyrite band edge at 0.8-0.9 eV (Figure 4.9). Samples with intermediate Ni content (25-1100 ppm) show two distinct regions of increased sub-gap absorptivity that resemble band tailing. The increase in absorptivity is quite small, <100 $cm^{-1}$ even for the most heavily doped of the homogeneous samples we studied (1088 ppm, Fig. 4.9a-b). We find that the absorption onset becomes much larger for more heavily doped samples (4763 ppm), becoming too opaque for measurement in our system at energies as low as 0.42 eV. However, we cannot eliminate the possibility of inhomogeneous solid solution phase impurities as the cause of such increased absorption. With $E_g \approx$ 0.3 eV [50], $NiS_2$ inclusions could readily explain this behavior. Similar absorption features were observed by Lehner in room-temperature transmission measurements of Ni-containing pyrite crystals [25].

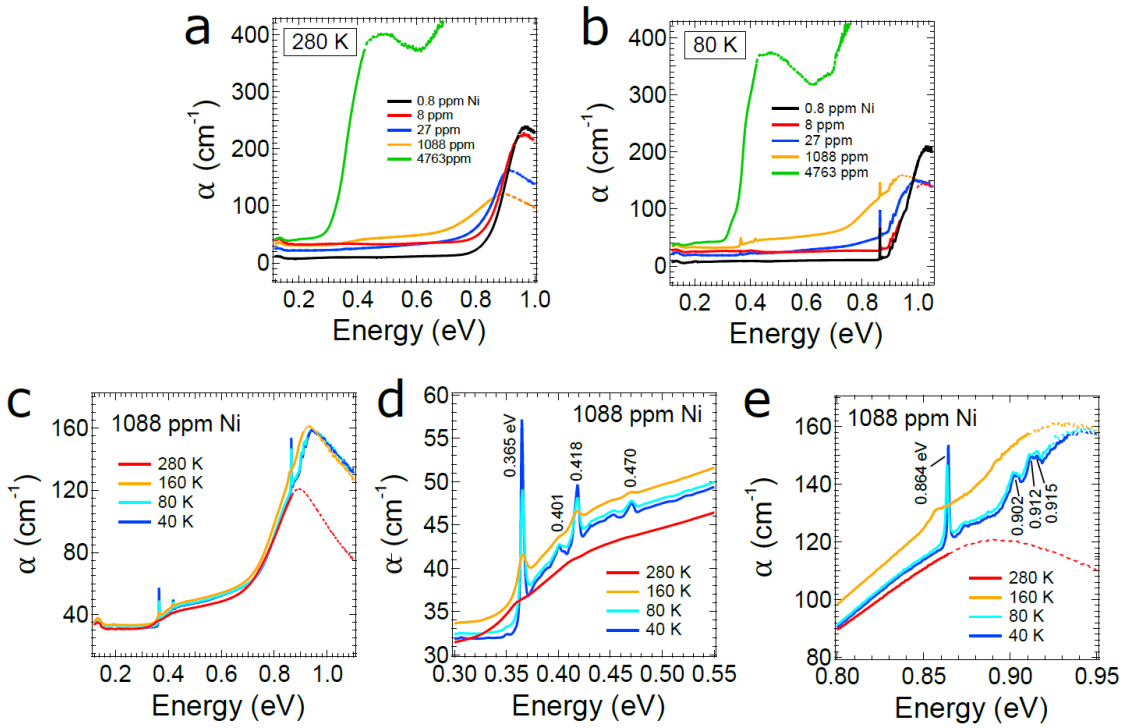


Figure 4.9. Optical absorptivity spectra of $Ni_xFe_{1-x}S_2$ crystals. FTIR absorptivity spectra of polished crystals with various nickel concentrations at (a) 80 K and (b) 280 K. Spectra of an undoped crystal ([Ni] ~ 0.8 ppm) are included for reference (black curves). The thickness of each sample is indicated in the legends. (c-e) Spectra versus temperature for the crystal with [Ni] = 1088 ppm. Dashed segments of the spectra denote regions in which data are unreliable due to limitations in instrument bandwidth or absorbance measurement range.

Below 280 K, a set of absorption peaks emerges at 0.35-0.5 eV on top of the broad sub-gap absorption (Fig. 4.9b,c,d). We observed these peaks only in $Ni_xFe_{1-x}S_2$ samples. The intensity and sharpness of the peaks increase with increasing [Ni] and decreasing temperature. The peak located at 365 meV lies at the low edge of the defect state absorption onset and, using DFT calculations to inform our assignment (Sec. 4.2.6, Fig. 4.11), is attributed to the free exciton generated from the electronic absorption from the induced Ni defect state to the conduction band edge. Using the exciton binding energy calculated in sec. 3.1.3, we place the defect state 378 meV below $E_C$. We tentatively assign the series of peaks lying at higher energy to phonon replicas of the 365 meV peak with the 401, 418, and 470 meV peaks corresponding to the $LO_4$,

| TO modes | Energy (meV) | LO modes | Energy (meV) |
|---|---|---|---|
| $TO_1$ | 51.1 | $LO_1$ | 54.3 |
| $TO_2$ | 50.3 | $LO_2$ | 51.1 |
| $TO_3$ | 42.4 | $LO_3$ | 43.4 |
| $TO_4$ | 35.8 | $LO_4$ | 36.0 |
| $TO_5$ | 26.7 | $LO_5$ | 26.7 |

Table 4.6: Transverse (TO) and longitudinal (LO) optical phonon modes of pyrite. Data adapted from [68]

$LO_1$, and $LO_1 + LO_2$ replicas, respectively (Table 4.6) [68].In addition, the usual set of sharp peaks at 0.85-0.93 eV is present in Ni-containing samples at $T < 200$ K. These high-energy sub-gap peaks seem unaffected by [Ni], at least for the homogeneous, single-phase samples ([Ni] < 1500 ppm).

### 4.2.5 Magnetization

We used variable temperature VSM measurements to determine the spin state of Ni in our $Ni_xFe_{1-x}S_2$ crystals. All crystals measured showed linear and reversible magnetization-field (M-H) plots at temperatures above 2 K, while M(H) is slightly nonlinear at 2 K (Figure 4.10a). The crystals are strongly paramagnetic at all temperatures, with much larger positive values of $\chi_{mol}$ than observed in the undoped crystals (Fig. 4.10b). These crystals behave as nearly ideal Curie paramagnets. Plots of $1/\chi_{mol,Ni}$ vs. $T$ are linear, as expected from the Curie-Weiss expression $\chi_{mol} = C_m/(T-\theta)$, while the Curie-Weiss temperature $\theta$ is essentially zero, which is characteristic of systems containing dilute, non-interacting paramagnetic centers (Fig. 4.10c). Interestingly, we

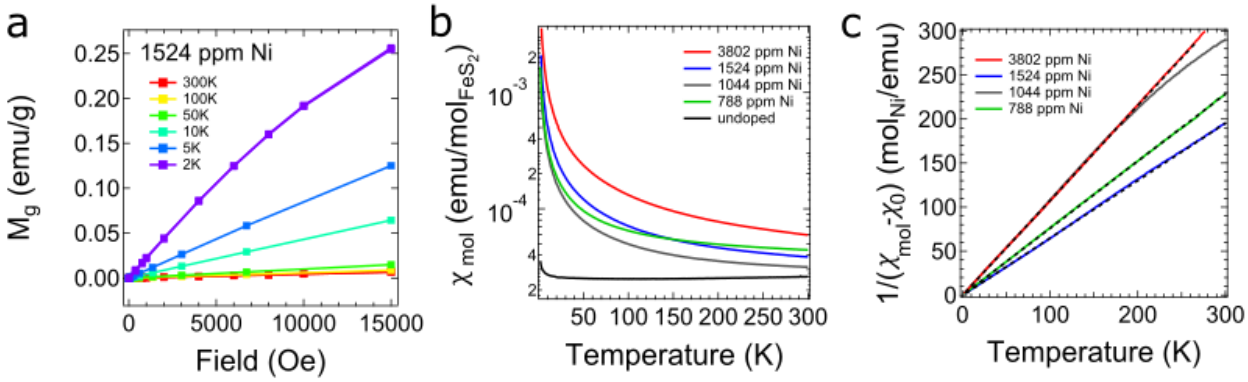


Figure 4.10. Magnetic properties of $Ni_xFe_{1-x}S_2$ crystals. (a) Mass magnetization ($M_g$) versus applied magnetic field at various temperatures for a crystal with [Ni] = 1524 ppm. (b) Molar susceptibility (on a $FeS_2$ basis) as a function of temperature. Data for an undoped crystal are also shown. (c) Inverse molar susceptibility (on a Ni basis) versus temperature. The good linear fit (dashed line) suggests that Ni-containing crystals are well behaved Curie paramagnets.

find that the 1044 ppm and 3802 ppm samples have nearly identical magnetic responses, with only a slight deviation near room temperature.

From fits we find effective magnetic moments $\mu_{eff}$ = 2.72, 3.51, 2.74, and 3.24 $\mu_B$ for [Ni] = 3802, 1524, 1044, and 788 ppm samples, respectively. Assuming a spin only contribution, we calculate ~1.9 unpaired electrons for the 3802 and 1044 ppm samples and 2.65 and 2.39 unpaired electrons for the 1524 and 788 ppm samples respectively. This leads us to believe that Ni is in the $d_8$ configuration with two unpaired electrons. Seeing values slightly higher than 2 from our spin only calculations is not surprising, since those calculations do not account for angular momentum contribution to the magnetic moment. And indeed effective magnetic moments of 2.9 – 3.3 Bohr magnetons for Ni in the $d_8$ configuration have been reported [30]. Thus, our measurements confirm the conclusion of previous ESR studies [52,69,70] that nickel exists in pyrite predominantly as $Ni^{2+}$ ($t_{2g}^6 e_g^2$ electron configuration).

| [Ni] (ppm) | $\mu_{eff}$ ($\mu_B$) | Θ (K) | n |
|---|---|---|---|
| 3802 | 0.16 | 2.72 | 1.90 |
| 1524 | 0.22 | 3.51 | 2.65 |
| 1044 | -0.12 | 2.74 | 1.912 |
| 788 | 0.07 | 3.24 | 2.39 |

Table 4.7: Results of Curie-Weiss fits of $Ni_xFe_{1-x}S_2$ crystals were $\mu_{eff}$ is the effective magnetic moment, Θ is the Curie-Weiss temperature, and n is the number of unpaired electrons.

### 4.2.6 Summary

DFT results are in excellent agreement with experimental observations for $Ni_xFe_{1-x}S_2$. As described above, Ni addition has little impact on electrical conductivity but significantly increases optical absorption below the band gap. Our calculations show that this behavior can be attributed to the generation by $Ni_{Fe}$ centers of localized *d* states ($e_g^*$ orbitals) deep within the band gap (Fig. 11a). Since this $Ni_{Fe}$ state is far from the band edges, the electrical conductivity of $Ni_xFe_{1-x}S_2$ is not significantly enhanced from that of undoped pyrite. However, optical transitions from the mid-gap Ni *d* states to the conduction bands of pyrite (blue arrow in Fig. 11a) reduces the optical absorption threshold to ~0.4 eV, similar to experiment. The calculations result in a $d^8$ electron configuration with two unpaired electrons per $Ni_{Fe}$ also in agreement with experiment. This is shown in Fig. 11c, with only the spin up $e_g^*$ states lying below the Fermi level.

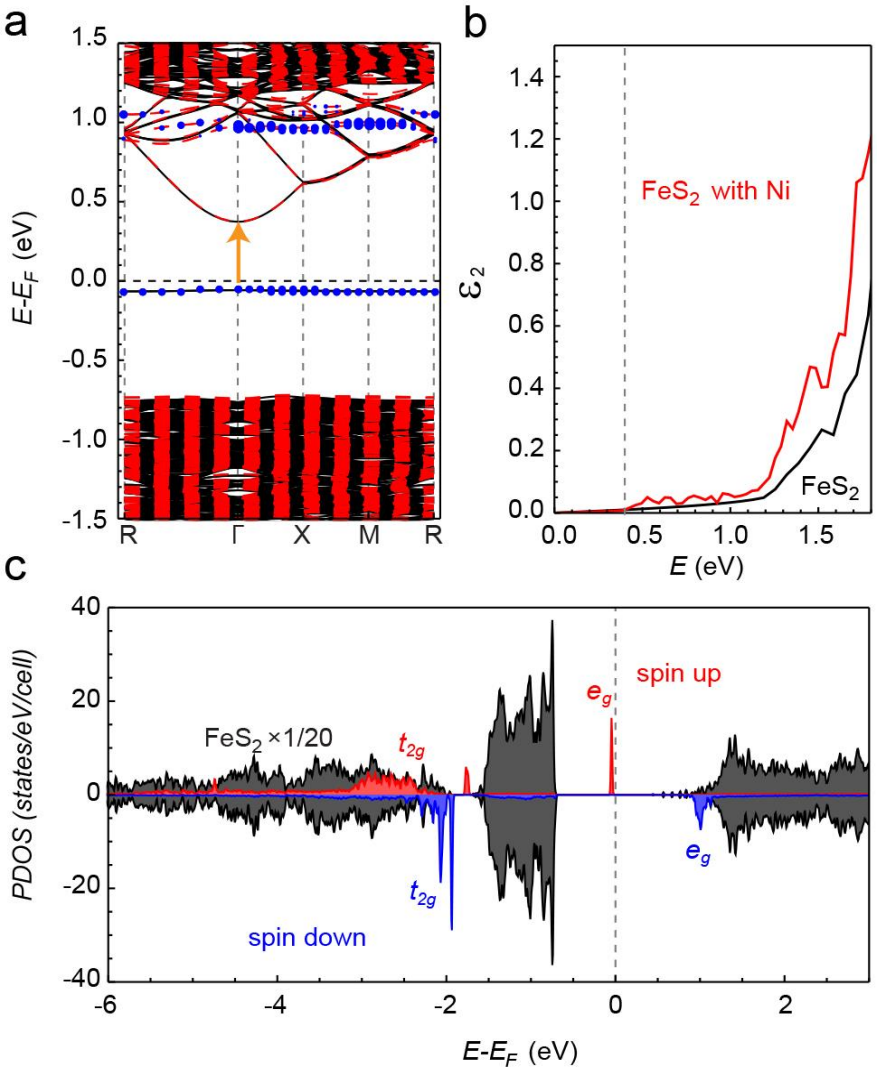


Figure 4.11. DFT results for $Ni_xFe_{1-x}S_2$. Calculated (a) band structure, (b) imaginary part of the dielectric function ($\varepsilon_2$), and (c) projected density of states for $Ni_xFe_{1-x}S_2$ with $x$ = 0.0091. Transitions from the half-filled *d*-orbitals of Ni ($e_g^*$ subset, blue dots) to the conduction band of pyrite (yellow arrow in (a)) account for the reduced absorption onset of ~0.4 eV (dashed line in (b)) for $Ni_xFe_{1-x}S_2$ crystals.

## 4.3 Chromium Doped ($Cr_xFe_{1-x}S_2$)

Cr was added to the crystal synthesis in the form of 99.99% $Cr(NO_3)_3 \bullet 9H_2O$ dissolved in methanol before being added to the growth crucible completeing the flux growth protocal in the same manner as the Co and Ni samples were. Samples were made with Cr concentrations ranging from 39 to 5187 ppm. The optical, electric, and magnetic properties of these crystals will be discussed in the following sections.

### 4.3.2 Elemental Characterization

Using ICP-MS and the same technique as we did with the Co and Ni doped crystals, we looked at the homogeneity of our Cr incorporation in one of our crystals. We find that the uniformity of Cr in the sample is excellent in all but one of the pieces measured, which had a ~30% lower concentration of Cr. The reason for this difference is not quite known, however the excellent agreement across the rest of the sample leads one to think it may have been an artifact of cause by sample preparation. Attempts were still made to measure the exact crystal used in the other measurement techniques whenever possible. As with Co and Ni, we found that Cr could be incorporated into the crystals without substantially increasing the concentration of the other elements measured by ICP-MS (Table 4.9). We do see a slightly higher Zn and Mn concentration than is typical of undoped crystals, but is not outside of the values seen.

| Sample | Cr:Fe Added | Section* | [Cr] (ppm at.) | Average [Cr] (atoms/cm$^{-3}$) | $x$ |
|---|---|---|---|---|---|
| **1** | 0.0022 | 1a | 411 | $3.1 \times 10^{19}$ | 0.0012 |
| | | 1b | 465 | | |
| | | 2a | 294 | | |
| | | 2b | 438 | | |
| | | 3a | 436 | | |
| | | 3c | 424 | | |

Table 4.8. [Cr] uniformity in $Cr_xFe_{1-x}S_2$ crystals. * Section 1 refers to the top of the crystal and section 3 to the bottom of the crystal (a and b refer to pieces of the crystal in the same z-section, measured to check for homogeneity in the xy plane).

### 4.3.1 Structural Characterization

Crystals synthesised with our Cr precuror show similar size, shape, faceting, and overall quality as our undoped crystals. Sycrotron XRD patterns taken of crystals with up to 5187 ppm suggest that all samples are single-phase, homogeneous $Cr_xFe_{1-x}S_2$ solid solutions with lattice constants that increase monotonically with $x$ over the range studied ($0 \leq x \leq 0.0149$, Fig. 4.12).

| 33 ppm Cr Sample | | | |
|---|---|---|---|
| S:Fe = 1.95022562[b] | | | |
| **element** | **ppm at** | **element** | **ppm at** |
| Na | 172.4187 | Te[a] | 0.0204 |
| Mg | 4.3873 | Cs | <0.009 |
| Sc | 0.0873 | Ba | <0.072 |
| Ti | 0.0417 | La | 0.0001 |
| V | 0.0326 | Ce | 0.0002 |
| Cr | 33.2700 | Pr | 0.0002 |
| Mn | 0.2949 | Nd | 0.0008 |
| Co | 0.1009 | Sm | 0.0001 |
| Ni | 0.5440 | Eu | <0.0001 |
| Cu | 0.5353 | Gd | 0.0001 |
| Zn | 7.0815 | Tb | 0.0026 |
| Ga | 0.0105 | Dy | 0.0001 |
| Ge | 0.0322 | Ho | 0.0005 |
| As | <0.0016 | Er | <0.0003 |
| Se | <0.004 | Tm | <0.0001 |
| Rb | <0.0296 | Yb | <0.0003 |
| Sr | 0.0146 | Lu | 0.0035 |
| Y[a] | 0.0001 | Hf[a] | 0.0008 |
| Zr[a] | 0.0229 | Ta[a] | 0.0001 |
| Nb[a] | 0.0021 | W[a] | 0.0014 |
| Mo[a] | 0.0051 | Re[a] | 0.0005 |
| Ru[a] | 0.0698 | Os[a] | 0.0001 |
| Rh[a] | 0.0116 | Ir[a] | 0.0001 |
| Pd[a] | 0.0074 | Pt[a] | 0.0008 |
| Ag | 0.1051 | Au[a] | 0.0004 |
| Cd | <0.0007 | Hg[a] | 0.1626 |
| In | 0.0108 | Tl | <0.0003 |
| Sn[a] | 0.0075 | Pb | 0.0035 |
| Sb[a] | 0.0075 | Bi | 0.0079 |
| | | U | <0.0006 |

Table 4.9: ICP-MS results of a typical Cr-doped ([Cr] = 33 ppm) crystal reported in atomic ppm. [a] Elemental concentration determined by semi-quantitative methods. [b] Due to sulfur loss during sample preparation, the measured S:Fe deviates from the expected 2:1.

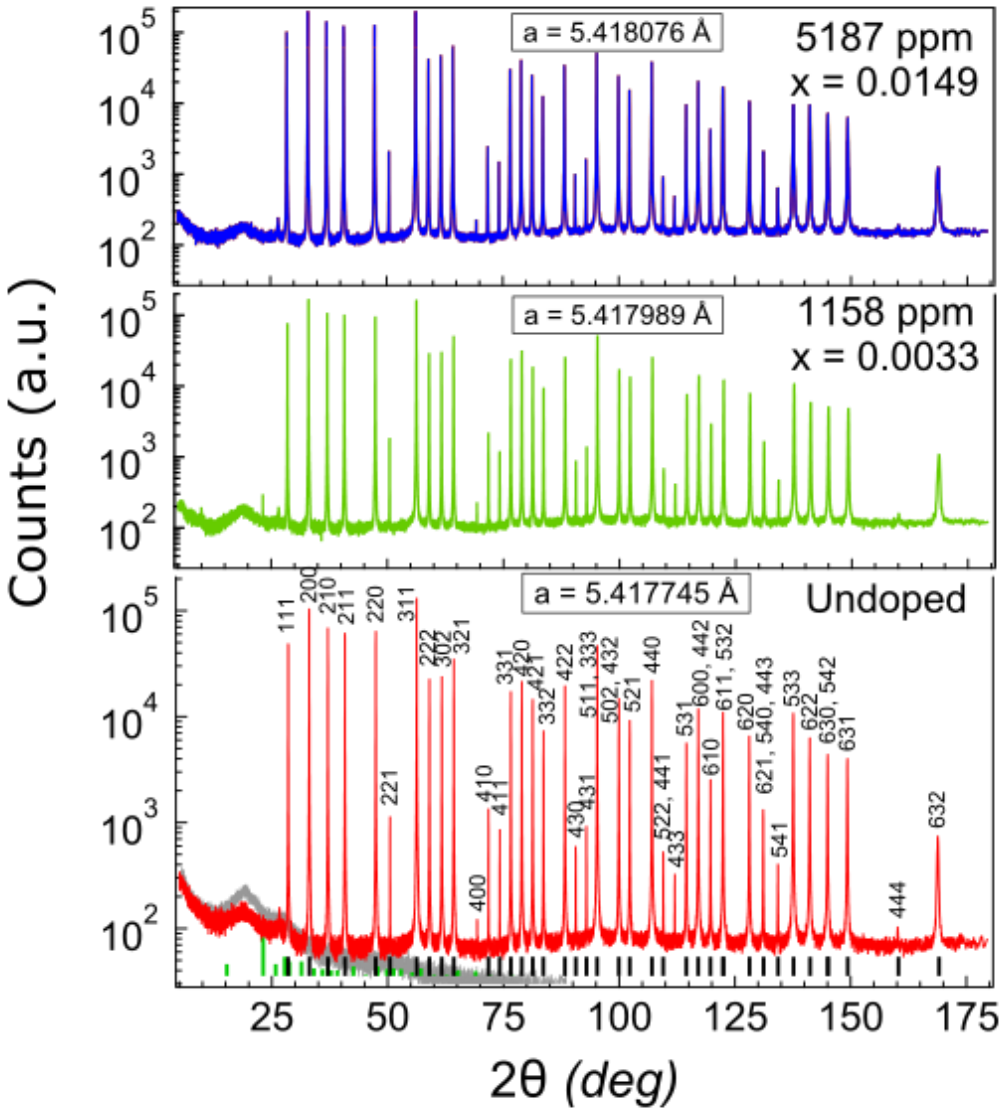


Figure 4.12. Synchrotron XRD pattern of a powdered undoped and powdered $Cr_xFe_{1-x}S_2$ crystals with $x$ = 0.0033 and 0.0149, presented on a log scale. All 39 reflections index to pyrite and no other phases are detected. Lattice parameters were calculated by Rietveld refinement with PDXL2 software at room temperature. The background pattern is for an empty capillary tube. Overlaid on the undoped data are a background pattern of an empty capillary tube (gray) as well as reference patterns for pyrite (black bars) and orthorhombic sulfur (green bars).

### 4.3.3 Hall Effect Studies

Chromium addition has a small but noticeable impact on the electrical properties of the pyrite crystals. Figure 4.13 shows that $\sigma(T)$ and $|R_H|(T)$ of the $Cr_xFe_{1-x}S_2$ and undoped crystals are qualitatively similar from 80-350 K. As with the $Ni_xFe_{1-x}S_2$ samples, all of the $Cr_xFe_{1-x}S_2$ crystals are unipolar *n*-type at higher temperatures. In this temperature regime, we find that $\sigma(T)$ rises and then levels off with increasing [Cr], reflecting a competition between increasing electron density and decreasing electron mobility (Fig. 4.13c-d). The room-temperature electron density increased tenfold and the mobility decreased by a factor of two across the range of [Cr] we studied (from $3\times10^{17}$ to $4\times10^{20}$ atoms $cm^{-3}$). The chromium doping efficiency ($\Delta n/\Delta$[Cr]) is low and decreases from ~0.01 at low [Cr] to $\sim10^{-4}$ at high [Cr], suggesting that $Cr_{Fe}$ is a deep donor that becomes increasingly compensated at higher doping density. We conclude that Cr acts as a donor in pyrite, but a very poor one.

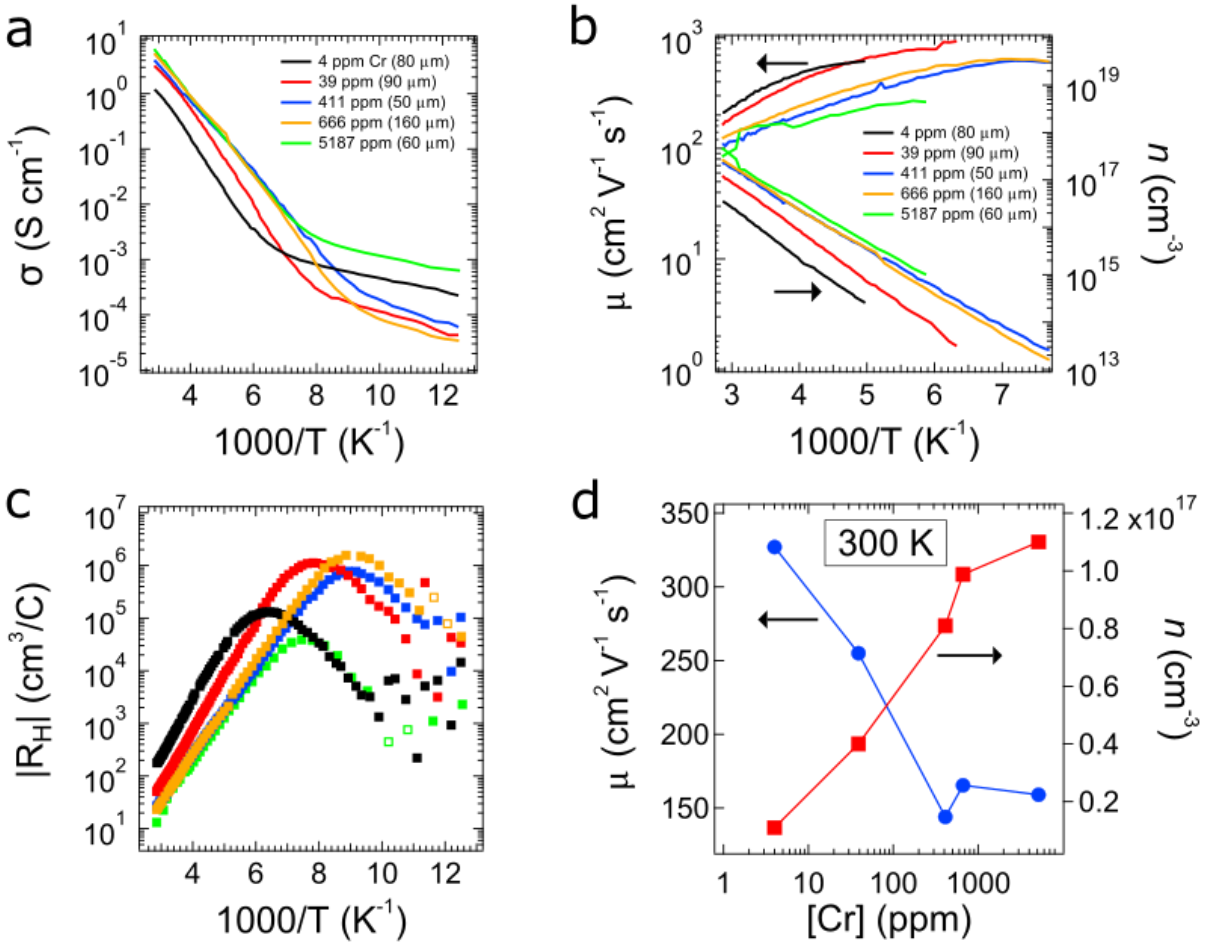


Figure 4.13. Electrical properties of $Cr_xFe_{1-x}S_2$ crystals. (a) Conductivity and (c) absolute Hall coefficient versus inverse temperature for samples with various chromium concentrations, from 4 ppm (for an undoped control crystal) to 5187 ppm. (b) Bulk electron density ($n$) and mobility ($\mu$) in the unambiguously unipolar ($n$-type) temperature region. (d) Room-temperature $n$ and $\mu$ as a function of [Cr].

### 4.3.4 Optical Absorption

Cr addition results in the appearance of significant sub-gap optical absorption. Samples with low [Cr] show an absorption shoulder that extends a few tenths of an eV into the bulk band gap (Figure 4.13). With increasing [Cr], this shoulder grows in intensity and develops a tail down to ~0.2 eV. Upon cooling the crystals, a series of at least five weak, equally-spaced absorption peaks develops on top of the tail from 0.15-0.45 eV. These peaks have a regular spacing of 50 ± 2 meV and an intensity that is the proportional to the Cr concentration. Since the energy of the strongest IR phonon mode observed in pyrite is ~49 meV [41], we tentatively assign the peaks at 0.241, 0.290, 0.340, and 0.391 eV as phonon replicas of the zero-phonon defect-related absorption at 0.191 eV. However, one would expect a significant drop in peak intensity for each increasing phonon interaction which we don't see here. If we accept the $Cr_{Fe}$-$V_S$ defect pair theory discussed in sec. 4.3.6 (Fig. 4.15d,e), we can assign the 0.191 eV peak to the exciton formed by excitation from the defect state to the CBM. Again assuming the same exciton binding energy derived in sec. 3.1.3, we determine an occupied Cr defect state 204 meV below the conduction band edge. We also observe at lower temperatures the usual series of sharp peaks just below the pyrite band edge (0.85-0.93 eV), but these peaks diminish in intensity with increasing [Cr], with a 30% reduction in the peak amplitude with a ~30 ppm increase in Cr concentration from the undoped case and are unresolvable at in samples with large [Cr] due to the low sample transmission. Thus, our results indicate that these high-energy peaks are unlikely to be caused by transitions involving Cr, as was proposed for the 0.864 eV peak by Yu

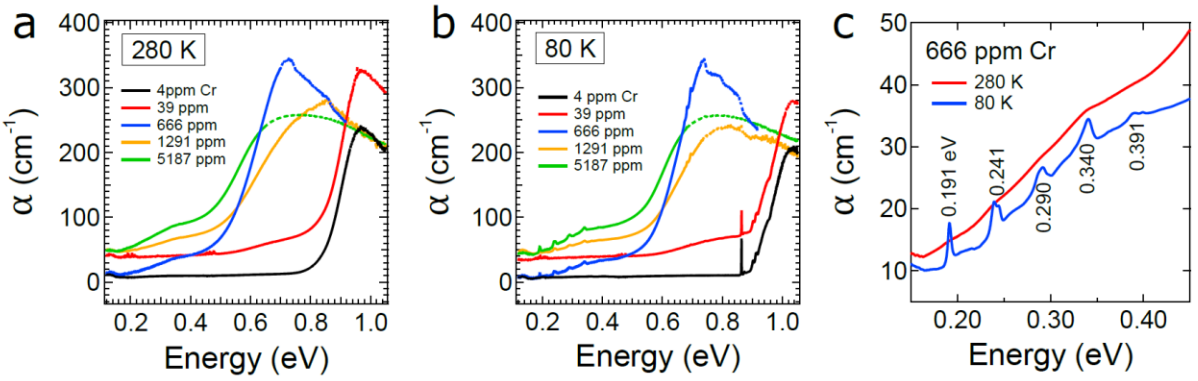


Figure 4.14. Optical absorptivity spectra of $Cr_xFe_{1-x}S_2$ crystals. FTIR absorptivity spectra of polished crystals with various chromium concentrations at (a) 80 K and (b) 280 K. Spectra of an undoped crystal ([Cr] ~ 4 ppm) are included for reference (black curves). The crystal with [Cr] = 1291 ppm was made using elemental Cr powder rather than $Cr(NO_3)_3$ to check that the observed spectral features are due to Cr rather than nitrogen or oxygen contamination. (c) Magnified view of spectra for the sample with [Cr] = 666 ppm to highlight the appearance of a series of equally-spaced peaks from 0.15-0.45 eV at low temperature.

*et. al.* [39,71,72]. Indeed, since the peak intensities are anti-correlated with [Cr], it is clear that chromium interferes with whatever states are responsible for these absorption features.

### 4.3.5 Magnetization

VSM magnometry measurements of Cr-doped crystals show a wide variety of responses for various Cr concentrations. Magnetization vs. field measurements of a 1158 ppm sample show a linear and reversible response curves above 2 K, at 2 K M(H) is still fairly linear but shows a small amount of hysteresis (Fig.1.14a), likely originating from sulfur deficient surface Fe. All of the crystals measured showed large positive $\chi_{mol}$ for all temperatures. Plots of $1/\chi_{mol,Cr}$ vs. T are predominately linear. Fits of these data sets are summarized in Table 4.9. The 622 and 1390 ppm samples similar magnetic properties. They have identical Curie-Weiss temperatures of essentially 0 K. Fits result in an effective magnetic moment of 3.01 and 2.68 $\mu_B$ for [Cr] = 622

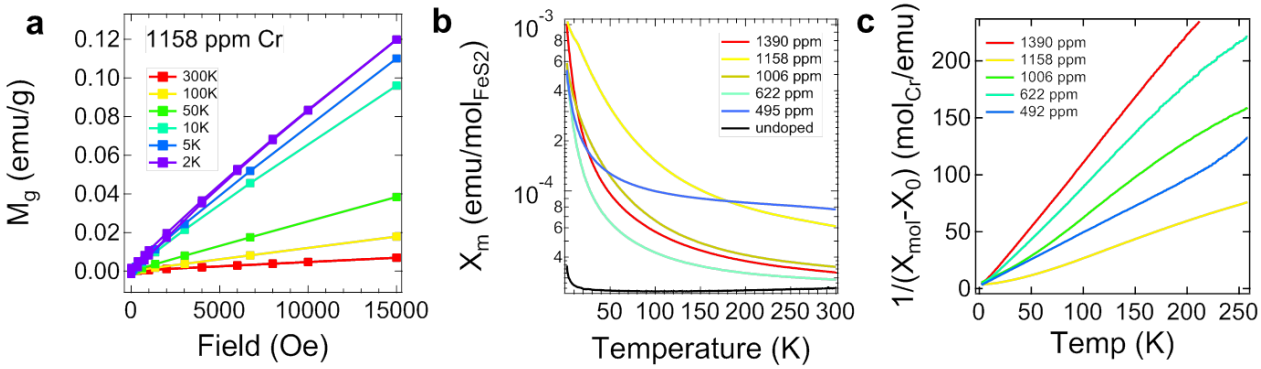


Figure 4.15. Magnetic properties of $Cr_xFe_{1-x}S_2$ crystals. (a) Mass magnetization ($M_g$) versus applied magnetic field at various temperatures for a crystal with [Cr] = 1158 ppm. (b) Molar susceptibility (on a $FeS_2$ basis) as a function of temperature. Data for an undoped crystal and a crystal with [Cr] = 411 ppm are also shown. (c) Inverse molar susceptibility (on a Cr basis) versus temperature. The data fit to Curie-Weiss paramagnetism with a Curie-Weiss temperature of 18 K.

and 1390 ppm respectively. Consistent with 2 unpaired electrons, suggesting that most of the $Cr_{Fe}$ in these samples are the low-spin $Cr^{2+}$ ($t_{2g}^4$ electron configuration, $S$ = 1). The 495 ppm sample has Θ = -5.58, indicating weak anti-ferromagnetic ordering in this sample. For this sample we find $\mu_{eff}$ = 4.13 $\mu_B$, which would arise from having 3 unpaired electrons. So the majority of $Cr_{Fe}$ in this sample would have to be $Cr^{3+}$ ($S$ = 3/2). Fitting the data for a crystal with [Cr] = 1158 ppm to the Curie-Weiss equation gives θ = 15 K, indicating an exchange interaction and transition to ferromagnetic ordering below ~15 K. We find an effective magnetic moment of 5.01 $\mu_B$, consistent with 4 unpaired electrons per chromium atom. This suggests that most of the $Cr_{Fe}$ in this sample is high-spin $Cr^{2+}$ (S = 2). The results of these measurements indicate that Cr can take a multitude of spin states within the $FeS_2$ lattice and it is likely that some concentration of each is present in each crystal. Under what conditions cause one spin state to become the majority is unclear at this time. We note that several EPR studies have reported the presence of $Cr^{3+}$ ($S$ = 3/2) in pyrite crystals [69–71]. However, given that $Cr^{2+}$ has an integer-spin

| [Cr] (ppm) | $\mu_{eff}$ ($\mu_B$) | Θ (K) | n | Oxidation state |
|---|---|---|---|---|
| 495 | -5.58 | 4.13 | 3.25 | 3+ |
| 622 | 0.89 | 3.01 | 2.16 | 2+ (low-spin) |
| 1158 | 15.7 | 5.01 | 4.5 | 2+ (high-spin) |
| 1390 | 0.89 | 2.685 | 2.23 | 2+ (low-spin) |

Table 4.9: Results of Curie-Weiss fits of $Cr_xFe_{1-x}S_2$ crystals were $\mu_{eff}$ is the effective magnetic moment, Θ is the Curie-Weiss temperature, and n is the number of unpaired electrons.

ground state (*S* = 1 or 2) and is "EPR silent" at the microwave frequencies used in these earlier studies [69,73,74], it is plausible that high concentrations of $Cr^{2+}$ could have been present in their samples as well.

### 4.3.6 Summary

DFT results for pyrite with isolated $Cr_{Fe}$ point defects proved to be in poor agreement with the experimental optical and electronic data for our $Cr_xFe_{1-x}S_2$ samples. Whereas the calculations predict that $Cr_{Fe}$ centers should introduce states into the conduction band that render pyrite metallic (Fig. 4.15a), experiment shows that Cr is a deep donor with only a small impact on electrical conductivity. The calculations also predict two prominent sub-gap peaks in the optical absorption spectrum that are not observed experimentally (Fig. 4.15b). Given the apparent inadequacy of a simple $Cr_{Fe}$ point defect model, we performed calculations of several defect pairs, including the $Cr_{Fe}$ dimer and $Cr_{Fe}$ paired with an adjacent sulfur vacancy ($V_S$). While the $Cr_{Fe}$ dimer configuration led to similar results as the isolated $Cr_{Fe}$, calculations show that $Cr_{Fe}$-$V_S$ pairs cause electronic and optical changes that are qualitatively similar to experimental

observations (see Figure 4.15d,e). Pairing with $V_S$ moves the filled *d* state below the Fermi level, which reduces the valence of the Cr impurity from +3 to +2. This state lies ~250 meV below the conduction band edge, in agreement with the poor ionization efficiency seen in electrical measurements and the absorption onset seen in Fig. 4.13. However this leads us to wonder how crystals can be dominated by the magnetic properties of $Cr^{3+}$ while none of the samples measured showed significantly increased carrier concentrations expected for a defect state resonant with the conduction band (as we see with Co). These results indicate that Cr has a very complex interaction with the $FeS_2$ lattice and a more detailed and systematic exploration would be necessary.

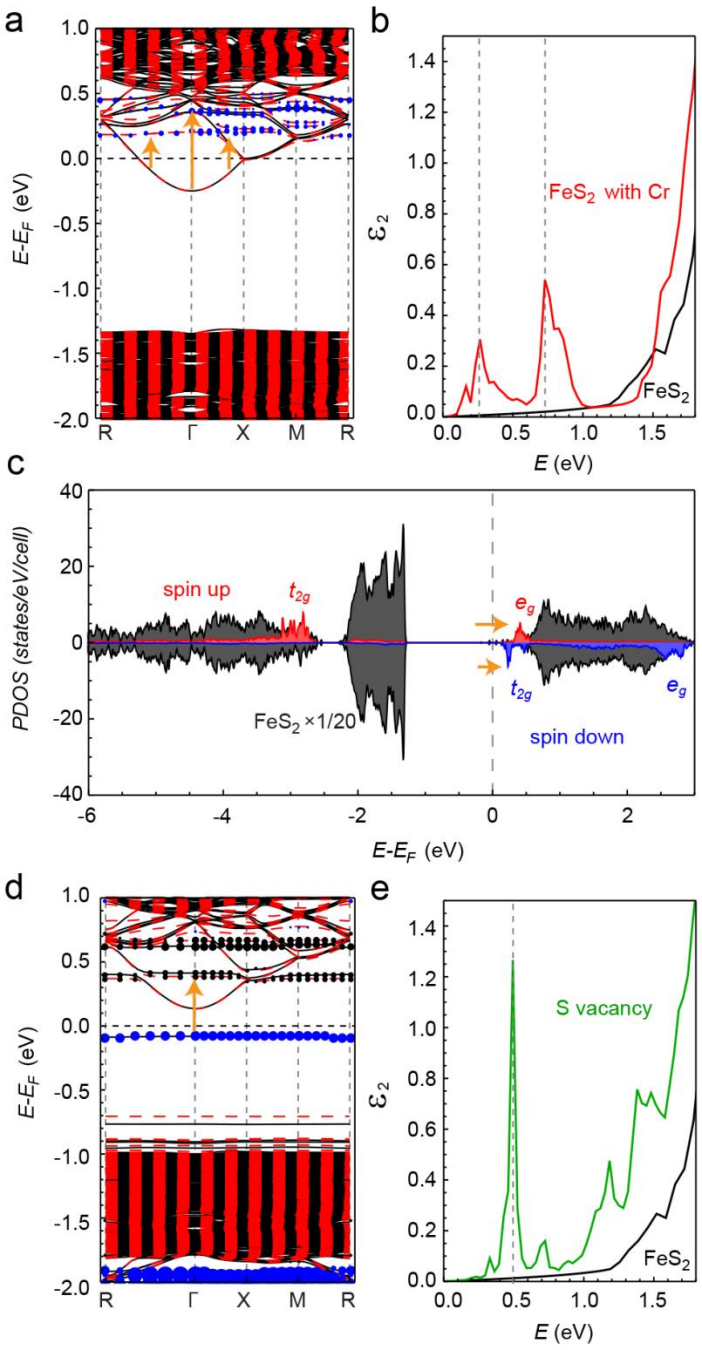


Figure 4.16. DFT results for $Cr_xFe_{1-x}S_2$. Calculated (a) band structure, (b) imaginary part of the dielectric function ($\varepsilon_2$), and (c) projected density of states for $Cr_xFe_{1-x}S_2$ with $x$ = 0.0091. The calculations predict transitions (yellow arrows in (a)) from the conduction bands of pyrite to the *d*-orbitals of Cr (blue dots in (a)) resulting in several prominent sub-gap absorption peaks (dashed lines in (b)). The calculated optical and electrical impact of isolated $Cr_{Fe}$ defects is not in agreement with experiment. Calculated (d) band structure, (e) imaginary part of the dielectric function ($\varepsilon_2$) for $Cr_xFe_{1-x}S_2$ with sulfur vacancies. Transitions (yellow arrow in (d)) from the *d*-orbitals of Cr (blue dots in (d)) to nearby Fe states (black dots in (d)) are corresponding to a peak at ~0.5 eV (dashed line in (e)) for $Cr_xFe_{1-x}S_2$ crystals.

## 4.4 Conclusions

We have studied the impact of Co, Ni, and Cr impurities on the electrical, optical, and magnetic properties of high-purity iron pyrite single crystals grown in sodium polysulfide flux. Without added Co, Ni, or Cr, the pyrite crystals are chemically pure (>99.998% on a metals basis) but still *n*-type near room temperature due to unintentional doping by $\sim 10^{19}$ $cm^{-3}$ native deep donors, probably sulfur vacancies. These crystals have relatively low room-temperature carrier density ($2 \times 10^{15}$ $cm^{-3}$) and high mobility (300 $cm^2$ $V^{-1}$ $s^{-1}$).

Cobalt is a well-behaved donor in pyrite with a defect state located above the conduction band minimum. We find a high doping efficiency at low [Co] (< 500 ppm). At these concentrations, cobalt is nonmagnetic $Co^{3+}$ ($t_{2g}^6$ electron configuration), consistent with full ionization. Samples with [Co] > 5 ppm show $n > 10^{17}$ $cm^{-3}$ at 300 K and metallic $\sigma(T)$ plots. The bulk electrons from $Co_{Fe}$ do not freeze out, so the transition from bulk to surface conduction normally seen in pyrite at lower temperatures does not occur in $Co_xFe_{1-x}S_2$ samples. On the basis of DFT results, we assign the Co-induced optical absorption features observed at <0.2 eV and 0.615 eV to transitions between a $Co_{Fe}$ state resonant with the pyrite conduction band and states lower and higher in the conduction band, respectively. From combined analysis of the data and with the help of DFT calculations we derive a Co defect state that lies ~70 meV above the conduction band edge. Cobalt is currently the best *n*-type dopant for pyrite because it offers high solubility

and doping efficiency with minimal compensation, mobility degradation, and magnetism (for [Co] < 500 ppm), enabling controlled doping to achieve a wide range of electron concentrations ($10^{15}$-$10^{20}$ $cm^{-3}$). For [Co] > 1000 ppm, the doping efficiency steadily decreases and $Co_xFe_{1-x}S_2$ samples become room-temperature paramagnets, as expected from previous work on $Co_xFe_{1-x}S_2$ alloys ($x > 0.005$).

Nickel does not significantly alter the carrier concentration of pyrite. Single-phase, homogeneous $Ni_xFe_{1-x}S_2$ samples could be made only for [Ni] < 1500 ppm. Such samples show substantial sub-gap optical absorption caused by transitions between the mid-gap states and the conduction band. Higher Ni content results in a phase mixture of solid solutions and greatly enhanced absorption down to ~0.27 eV. Samples with [Ni] < 1000 ppm are well-behaved Curie paramagnets. Susceptibility data indicates that each $Ni_{Fe}$ has two unpaired electrons (i.e., $Ni^{2+}$ with a $t_{2g}^6 e_g^2$ configuration), which agrees with our DFT results and previous experimental studies. A self-consistent picture drawn from the data places the $Ni_{Fe}$ state 378 meV below. Except for causing low-temperature magnetism and some degradation in electron mobility, Ni by itself seems to be an inert impurity in iron pyrite. Still, future devices would benefit from controlling Ni contamination in order to boost mobilities and decrease recombination, therefore increasing device performance.

Chromium acts as a deep donor with a doping efficiency that drops with increasing [Cr], making it a poor dopant in pyrite. Cr also degrades the electron mobility by about a factor of two. $Cr_xFe_{1-x}S_2$ samples show a strong absorption tail to ~0.5 eV and a weak tail to ~0.2 eV, qualitatively similar to the spectra of the $Ni_xFe_{1-x}S_2$ crystals. The similarity of the absorptivity

spectra is unsurprising given that both Cr and Ni impurities introduce deep gap states in pyrite. However, DFT calculations predict that isolated $Cr_{Fe}$ centers should be auto-ionizing donors, contrary to the experimental findings. Better agreement with optical and electrical experiment was achieved with calculations of $Cr_{Fe}$-$V_S$ pairs, which suggests that Cr may occur mostly in defect complexes rather than as simple $Cr_{Fe}$ point defects. While DFT calculations indicate Cr in $Cr_{Fe}$-$V_S$ defect pairs is in the low-spin $Cr^{2+}$ state, magnetic data show that Cr adopts several configurations: low-spin $Cr^{2+}$, high-spin $Cr^{2+}$ (with ferromagnetic alignment at low temp), and $Cr^{3+}$ (with slight anti-ferromagnetic alignment at low temp). Excluding the magnetic data, Cr appears to form $Cr_{Fe}$-$V_S$ defect complexes with a partially occupied defect state 204 meV below the conduction band. Reconciling the disagreement between the magnetic data and the other measurements would take a more thorough and systematic look at Cr incorporation in pyrite. Given the position of the defect state within the band gap, we conclude Cr would be detrimental to pyrite device performance, acting both as a scattering center for transport as well as a possible recombination center and its unintentional incorporation should be minimized.

This study shows that progress in understanding and controlling the doping of iron pyrite can be achieved through combined electrical, optical, and magnetic measurements of ultrapure single crystals spiked with individual impurity elements. Using this approach, we have found that cobalt is an ideal *n*-type dopant, while nickel and chromium have been identified as detrimental impurities in pyrite. Both are deep donors that hardly affect the carrier concentration, while acting as scattering centers, reducing carrier mobilities, and likely lead to higher recombination rates in PV devices. This work establishes the basic behavior of these

three transition metal impurities, but many important open questions remain for further study. Identifying and then controlling the concentration of the native deep donor(s) responsible for the unintentional *n*-type doping of pyrite crystals remains a critical challenge in the controlled doping of this material for optoelectronic applications. Discovering a well-behaved shallow acceptor and translating the single crystal results to thin films are also useful directions.

# References


[1] BP, *Statistical Review of World Energy* (2019).
[2] U.S. Energy Information Administration, *International Energy Outlook 2019* (2019).
[3] DOE, (n.d.).
[4] NREL, (2019).
[5] C. Wadia, A. P. Alivisatos, and D. M. Kammen, Environ. Sci. Technol. **43**, 2072 (2009).
[6] S. Rühle, Sol. Energy (2016).
[7] A. Ennaoui, S. Fiechter, C. Pettenkofer, N. Alonsovante, K. Buker, M. Bronold, C. Hopfner, and H. Tributsch, Sol. Energy Mater. Sol. Cells **29**, 289 (1993).
[8] A. Ennaoui, S. Fiechter, W. Jaegermann, and H. Tributsch, J. Electrochem. Sci. Technol. **133**, 97 (1986).
[9] J. Hu, Y. Zhang, M. Law, and R. Wu, J. Am. Chem. Soc. **134**, 13216 (2012).
[10] R. Schieck, A. Hartmann, S. Fiechter, R. Könenkamo, and H. Wetzel, J. Mater. Res. **5**, 1567 (1990).
[11] G. Smestad, A. Ennaoui, S. Fiechter, H. Tributsch, W. K. Hofmann, M. Birkholz, and W. Kautek, Sol. Energy Mater. **20**, 149 (1990).
[12] A. Ennaoui and H. Tributsch, Sol. Energy Mater. **14**, 461 (1986).
[13] P. P. Altermatt, T. Kiesewetter, K. Ellmer, and H. Tributsch, Sol. Energy Mater. Sol. Cells **71**, 181 (2002).
[14] M. Bronold, C. Pettenkofer, and W. Jaegermann, J. Appl. Phys. **76**, 5800 (1994).
[15] R. Murphy and D. R. Strongin, Surf. Sci. Rep. **64**, 1 (2009).
[16] M. Limpinsel, N. Farhi, N. Berry, J. Lindemuth, C. L. Perkins, Q. Lin, and M. Law, Energy Environ. Sci. **7**, 1974 (2014).
[17] S. Seefeld, M. Limpinsel, Y. Liu, N. Farhi, A. Weber, Y. Zhang, N. Berry, Y. J. Kwon, C. L. Perkins, J. C. Hemminger, R. Wu, and M. Law, J. Am. Chem. Soc. **135**, 4412 (2013).
[18] J. Walter, X. Zhang, B. Voigt, R. Hool, M. Manno, F. Mork, E. S. Aydil, and C. Leighton, Phys. Rev. Mater. **1**, 065403 (2017).
[19] M. Cabán-Acevedo, N. S. Kaiser, C. R. English, D. Liang, B. J. Thompson, H. E. Chen, K. J. Czech, J. C. Wright, R. J. Hamers, and S. Jin, J. Am. Chem. Soc. **136**, 17163 (2014).
[20] Y. N. Zhang, J. Hu, M. Law, and R. Q. Wu, Phys. Rev. B - Condens. Matter Mater. Phys. **85**, 1 (2012).
[21] F. W. Herbert, A. Krishnamoorthy, K. J. Van Vliet, and B. Yildiz, Surf. Sci. **618**, 53 (2013).
[22] K. Büker, N. Alonso-Vante, and H. Tributsch, J. Appl. Phys. **72**, 5721 (1992).
[23] M. Bronold, K. Buker, S. Kubala, C. Pettenkofer, and H. Tributsch, **231**, (1993).
[24] M. Birkholz, S. Fiechter, A. Hartmann, and H. Tributsch, Phys. Rev. B **43**, 11926 (1991).
[25] S. W. Lehner, N. Newman, M. Van Schilfgaarde, S. Bandyopadhyay, K. Savage, and P. R. Buseck, J. Appl. Phys. **111**, 0 (2012).
[26] B. Voigt, W. Moore, M. Manno, J. Walter, J. D. Jeremiason, E. S. Aydil, and C. Leighton, ACS Appl. Mater. Interfaces **11**, 15552 (2019).

[27] J. Sangster and A. D. Pelton, J. Phase Equilibria **18**, 89 (1997).
[28] J. I. Pankove, *Optical Processes in Semiconductors* (Dover, 1971).
[29] M. Levy and M. P. Sarachik, Rev. Sci. Instrum. **60**, 1342 (1989).
[30] C. . E. Housecraft and A. G. Shargpe, *Inorganic Chemistry* (Pearsons, Harlow, England, 2012).
[31] R. L. Petritz, Phys. Rev. **110**, 1254 (1958).
[32] S. M. Sze and K. K. Ng, *Physics of Semiconductor Devices* (Wiley-Interscience, 2007).
[33] P. E. Blöchl, Phys. Rev. B **50**, 17953 (1994).
[34] G. Kresse and D. Joubert, Phys. Rev. B **59**, 1758 (1999).
[35] G. Kresse and J. Hafner, Phys. Rev. B **49**, 14251 (1994).
[36] J. P. Perdew, K. Burke, and M. Ernzerhof, Phys. Rev. Lett. **77**, 3865 (1996).
[37] J. Hu, Y. Zhang, M. Law, and R. Wu, Phys. Rev. B - Condens. Matter Mater. Phys. **85**, 1 (2012).
[38] S. G. Choi, J. Hu, L. S. Abdallah, M. Limpinsel, Y. N. Zhang, S. Zollner, R. Q. Wu, and M. Law, Phys. Rev. B - Condens. Matter Mater. Phys. **86**, 1 (2012).
[39] T. R. Yang, J. T. Yu, J. K. Huang, S. H. Chen, M. Y. Tsay, and Y. S. Huang, J. Appl. Phys. **77**, 1710 (1995).
[40] W. Kou and M. Seehra, Phys. Rev. B. Condens. Matter **18**, 7062 (1978).
[41] J. L. E. Verdi and R. F. Willis, (n.d.).
[42] A. Schlegel and P. Wachter, J. Phys. C Solid State Phys. **9**, 3363 (1976).
[43] P. Lazić, R. Armiento, F. W. Herbert, R. Chakraborty, R. Sun, M. K. Y. Chan, K. Hartman, T. Buonassisi, B. Yildiz, and G. Ceder, J. Phys. Condens. Matter **25**, (2013).
[44] P. Burgardt and M. S. Seehra, Solid State Commun. **22**, 153 (1977).
[45] V. . Gupta and N. . Ravindra, Solid State Commun. **32**, 1327 (1979).
[46] L. A. Marusak, C. Cordero-Montalvo, and L. N. Mulay, Mater. Res. Bull. **12**, 1009 (1977).
[47] A. M. Karguppikar and A. G. Vedeshwar, Phys. Status Solidi **95**, 717 (1986).
[48] S. Ogawa, J. Phys. Soc. Japan **41**, 462 (1976).
[49] S. Ogawa, J. Appl. Phys. **50**, 2308 (1979).
[50] R. L. Kautz, M. S. Dresselhaus, D. Adler, and A. Linz, Phys. Rev. B **6**, 2078 (1972).
[51] L. Wang, T. Y. Chen, C. L. Chien, J. G. Checkelsky, J. C. Eckert, E. D. Dahlberg, K. Umemoto, R. M. Wentzcovitch, and C. Leighton, Phys. Rev. B **73**, 144402 (2006).
[52] R. Chandler and R. Bené, Phys. Rev. B **8**, 4979 (1973).
[53] C. H. Ho, C. E. Huang, and C. C. Wu, J. Cryst. Growth **270**, 535 (2004).
[54] C.-H. Ho, M.-H. Hsieh, and Y.-S. Huang, J. Electrochem. Soc. **155**, H254 (2008).
[55] K. S. Savage, D. Stefan, and S. W. Lehner, Appl. Geochemistry **23**, 103 (2008).
[56] S. W. Lehner, K. S. Savage, and J. C. Ayers, J. Cryst. Growth **286**, 306 (2006).
[57] Y. Tomm, R. Schieck, K. Ellmer, and S. Fiechter, J. Cryst. Growth **146**, 271 (1995).
[58] S. R. Butler and R. J. Bouchard, J. Cryst. Growth **10**, 163 (1971).
[59] B. Thomas, K. Ellmer, W. Bohne, J. Röhrich, M. Kunst, and H. Tributsch, Solid State Commun. **111**, 235 (1999).
[60] S. Guo, D. P. Young, R. T. MacAluso, D. A. Browne, N. L. Henderson, J. Y. Chan, L. L. Henry, and J. F. Ditusa, Phys. Rev. B - Condens. Matter Mater. Phys. **81**, 1 (2010).
[61] S. Guo, D. P. Young, R. T. MacAluso, D. A. Browne, N. L. Henderson, J. Y. Chan, L. L. Henry, and J. F. Ditusa, Phys. Rev. B - Condens. Matter Mater. Phys. **81**, 1 (2010).

[62] H. S. Jarrett, W. H. Cloud, R. J. Bouchard, S. R. Butler, C. G. Frederick, and J. L. Gillson, Phys. Rev. Lett. **21**, 617 (1968).
[63] K. Sato, Prog. Cryst. Growth Charact. **11**, 109 (1985).
[64] J. F. Gibbons and R. E. Tremain, Appl. Phys. Lett. **26**, 199 (1975).
[65] P. R. C. Stevens and A. W. Tinsley, J. Phys. C Solid State Phys. J. Phys. C Solid State Phys **4**, L150 (1971).
[66] L. A. Clark and G. Kullard, Econ. Geol. **58**, 853 (1963).
[67] P. Waldner and A. D. Pelton, Metall. Mater. Trans. B **35**, 897 (2004).
[68] W. Bührer, E. Lafougère, and H. Lutz, J. Phys. Chem. Solids **54**, 1557 (1993).
[69] D. Siebert, R. Miller, S. Fiechter, P. Dulski, and A. Hartmann, Zeitschrift Für Naturforsch. A **45**, 1267 (1990).
[70] J. T. Yu, C. J. Wu, Y. S. Huang, and S. S. Lin, J. Appl. Phys. **71**, 370 (1992).
[71] J. T. Yu, Y. S. Huang, and M. Y. Tsay, J. Appl. Phys. **75**, 5282 (1994).
[72] S. H. Chen, M. Y. Tsay, Y. S. Huang, and J. T. Yu, J. Phys. Condens. Matter **6**, 9211 (1994).
[73] J. Krzystek, A. Ozarowski, and J. Telser, Coord. Chem. Rev. **250**, 2308 (2006).
[74] Joshua Telser, L. A. Pardi, A. J. Krzystek, and L.-C. Brunel, (1998).